The Dissertation Committee for Shadrian Brittany Strong
certifies that this is the approved version of the following dissertation:

Climate Modeling of Giant Planets: The Saturnian Seasonal Stratosphere

Committee:

John H. Lacy, Supervisor

Daniel T. Jaffe

J. Craig Wheeler

Paul Harvey

Thomas K. Greathouse

Climate Modeling of Giant Planets: The Saturnian Seasonal Stratosphere

by

Shadrian Brittany Strong, B.S.; M.A.

DISSERTATION

Presented to the Faculty of the Graduate School of

The University of Texas at Austin

in Partial Fulfillment

of the Requirements

for the Degree of

DOCTOR OF PHILOSOPHY

THE UNIVERSITY OF TEXAS AT AUSTIN

May 2008

Dedicated to Mama, Dresden, and Kit.

Acknowledgments

I would like to acknowledge the many people who have helped me get through these last six years, despite the many ups and downs of my graduate career. Thanks to my mother for driving me out to Austin for my first ever AAS meeting in 2000, and who has always encouraged me to learn and excel (*te amo; yo pasó por aquí*). Thanks to my sister (*Mon amour pour toi est si grand que le Mond*), with whom I share a secret language, and whose bull-headedness and strength has provided comfort. Thanks to my husband, Kit, without whom I would have been lost, especially these last few grueling, graduate years. I wish to thank Erin McMahon for our shared uniqueness and friendship (and job assistance!). Marty, Andrea, Amanda, and Nairn, I'm so glad I know you. Thank you Julie Moses for all your help, John Lacy for your incredible repository of knowledge and patience (and sending me to Hawaii with the TEXES team on numerous occasions), Matt Richter for unlimited TEXES tutorials, Tommy G. for providing a great project when I needed it the most, and Stephanie G. for your incredible cooking back in the Houston days. Dan Jaffe and Craig Wheeler have been extremely helpful and supportive throughout my (several) research pursuits. Thank you, Stephanie Crouch and Char Burke. LPI's computer staff have kept my Beowulf nodes rolling and have helped on many occasions. Thanks to the Lunar and Planetary Institute's continued support, I have been able to pour myself into research for the last three years despite the fact that I never remember to fill out my timesheet on

time.

Climate Modeling of Giant Planets: The Saturnian Seasonal Stratosphere

Publication No. ⎯⎯⎯⎯⎯⎯

Shadrian Brittany Strong, Ph.D.
The University of Texas at Austin, 2008

Supervisor: John H. Lacy

In this dissertation, I present an improved multilayer radiative seasonal climate model for the study of giant-planet stratospheric temperatures with primary application to Saturn. Motivated by current Cassini and ground-based observations of a persistent enhancement of hydrocarbon emission from equator to south pole on Saturn (Greathouse *et al.* 2005a,b; Orton *et al.* 2005; Flasar *et al.* 2005; and Howett *et al.* 2007), and the need to disentangle radiative and dynamical contributions to seasonal climate change, this work details the sensitivity of the stratosphere towards seasonal changes in insolation and chemistry. Until this research, the seasonal stratospheric responsivity was found to be slow and minimally pressure-dependent. Despite the fact that methane is the dominant absorber in giant planet atmospheres, current knowledge of shortwave near-infrared spectral transitions are limited to laboratory fitted band-models, which are not generated with optimal giant-planet atmospheric conditions (Tomasko et al. 2007). Summer thermal trends

in the stratosphere are heavily dependent upon shortwave CH_4 near-infrared parameterization. Observational trends in 2002 and 2004 are reproduced

This model incorporates stratospheric heating due to CH_4 absorption of sunlight in the near infrared and visible regime and by C_2H_2, C_2H_6, and C_2H_4 in the ultraviolet over the spectral region 2000 to 10^5 cm^{-1}. Stratospheric cooling is due to CH_4, C_2H_2, and C_2H_6 line emission along with H_2-H_2, H_2-He, and H_2-CH_4 collision induced continuum emissions within the spectral range of 0 to 1600 cm^{-1}. The inclusion of seasonally variable photochemical hydrocarbon abundances produces seasonal trends comparable to observations. The choice of near-infrared (2000 - 9500 cm^{-1}) CH_4 absorption parameterization dramatically influences stratospheric heating and largely determines the seasonal responsivity of the stratosphere.

Table of Contents

List of Tables

List of Figures

Chapter 1

Introduction

1.1 Methodology

To paraphrase Yung and Demore (1999), it is best to ask not why other planets are different from Earth, but rather what makes Earth unique? The evolution of Earth's extensive biosphere is coupled with the evolution of its atmosphere (Yung and Demore 1999). Consequentially, complexities arise in disentangling individual evolutionary contributions relating to physical processes (chemistry, dynamics, life). The planets in our solar system are only unified in their time of origin, $\sim$ 4.6 billion years ago. Beyond that date, planetary divergences may be attributed to evolution and chemistry, predominately fated by solar evolution and the subsequent solar radiation received by the planets as well as differences in planetary composition and mass.

Less than 1% of the total incident solar flux is available to drive atmospheric photochemistry. The majority of chemical reactions persist in cycles, such that few reactions simply convert one species to another. Rather, chemistry is a persistent process that depends on the amount and type of molecules within an atmosphere, the amount of insolation[1], the extent of the atmosphere,

---

[1]Solar insolation is predetermined by the axial tilt of the planet, incident angles, rings,

lifetimes and reactivity of the molecules, to name a few. The time for reactions to occur or persist (1μs to a few billion years) will have a sizeable effect on atmospheric composition and evolution. When reactions result in net conversion of species, the atmosphere evolves (Yung and Demore 1999).

Photochemistry may dominate in the upper atmosphere, but deeper in the atmosphere, where turbulent motions work to mix the atmosphere and ultraviolet radiation from the sun is no longer directly significant, dynamics are important (e.g. Showman et al. 2005; Haigh et al. 2006; Brönnimann et al. 2001). Circulation (e.g. Hadley cells on Earth), zonal winds[2], and more transient weather phenomena[3] are observed[4] (e.g. Sánchez-Lavega et al. 2004; Dyudina et al. 2007).

In studying a simplified, non-anthropogenically influenced 'laboratory' source, such as a giant planet, we can identify key physical processes that drive thermal responsivity in the stratosphere. Whether thermal changes in the stratosphere may be modeled with radiative processes alone remains unknown. It has been suggested that large-scale circulation (e.g. upwelling at the equator and downwelling at the poles) is required to model observationally derived thermal variations in Saturn's stratosphere (Flasar et al. 2005). It is of great

orbital distance of the planet, etc.

[2]For Saturn, zonal winds have been measured to be $\sim 200 - 400$ m/s at the equator between 1994 to 2004 (Sánchez-Lavega et al. 2004)

[3]As opposed to *climate* phenomena which persist for long periods of time, *weather* is indicative of short term atmospheric variations

[4]Lightning, recently observed by Cassini (Dyudina et al. 2007) is thought to occur at the 0.6 - 1.6 bar level resulting from violent, short term storms.

importance to study the atmospheric responsivity to changes in solar forcing, and how the resulting photochemical reactions alter seasonal temperatures. In doing so, we may begin to discern the stability of an atmosphere, both chemically and climatically, and its evolutionary process.

It is not within the scope of this research to definitively answer all questions pertaining to atmospheric evolution of giant planets, much less the Earth. Rather, the goal of this research is to thoroughly examine radiative balance in a giant planet's stratosphere in order to further atmospheric studies of giant planets as a whole. Saturn is the subject of interest in this work, motivated by a current influx of data and a need to revise the outdated, Voyager-era stratospheric modeling assumptions (Greathouse et al. 2005a; Flasar et al. 2005; Howett et al. 2007; Fletcher et al. 2007; Orton and Yanamandra-Fisher 2005; Orton et al. 2007). Developing an updated radiative-seasonal climate model would dramatically influence current perceptions of giant planet climatology.

1.2   The Giant Planets: Modeling Motivation

The four giant planets in our solar system may be divided into two categories: the gas giants (Jupiter and Saturn) and the ice giants (Uranus and Neptune). All four planets may be characterized by large volumes and masses, low densities, a significant number of satellites, and the existence of a ring system. These giant planets are predominantly composed of molecular hydrogen ($> 80\%$) and helium ($\sim 10\%$), and have trace amounts of minor molecules

like methane. Their compositions are likely indicative of their formation in the early solar nebula: having formed far from the Sun at cold temperatures, the giant planets retained ices in their interiors. Gravitational accretion onto their rocky, icy cores produced a form of the atmospheres observed today (Encrenaz et al. 2004). Therefore, giant planet atmospheres are believed to reflect the composition of the early solar nebula.

Planet formation remains a fundamental problem in science. From the early Sun's protoplanetary disk, the solar system was likely formed. The minimum mass of the disk was ~ 0.02 Solar masses based on abundances of refractory elements in the planets and the base assumption that all abundances throughout the nebula were initially solar (de Pater and Lissauer 2001). In one theory of planet formation, cooling of the protoplanetary disk led to the condensation and formation of planetesimals. The conglomeration of planetesimals resulted in the cores of the planets. Gas accretion onto the cores, in the case of the giant planets, resulted in predecessors of the atmospheres observed today. An alternate ('top-down')[5] theory, the gravitational instability theory, suggests that protoplanets are formed through gravitational instability of the protoplanetary disk followed by coagulation of dust grains to form the core (e.g. Boss 2002).

The largest giant planets, Jupiter and Saturn ($R_{eq} \sim$ 71,492 km, 60,268 km; $\rho = 1.33$ g cm^{-3}, 0.70 g cm^{-3}), are believed to have the smallest cores

---

[5]Boss 2002

(de Pater and Lissauer 2001). By comparison, the cores of Uranus and Neptune likely comprise more than half of their total masses ($R_{eq} \sim$ 25,559 km, 24,764 km; ρ = 1.30 g cm^{-3}, 1.76 g cm^{-3})[6]. While the accretion formation theory is currently the most plausible one, this method results in slow core formation for Uranus and Neptune. Due to this slow core formation, little time would remain for these planets to accrete their substantial gaseous envelopes prior to removal of the protoplanetary disk (e.g. Boss 2002). Conversely, this theory easily predicts the formation of Saturn and Jupiter due to their dense, gaseous environment in the protoplanetary disk. Neither observations of the cores of giant planets nor observations of direct planet formation exist.

The atmospheres of giant planets provide an interface between external solar radiation and internal energy sources, resulting in a tangled interplay of dynamics, radiation, and chemistry working to drive annual temperature variations. The significance of dynamics, chemistry, and radiation and their role in driving thermal variations are not well characterized.

In recent years, a significant number of planetary observations have been performed using ground based and spaced based telescopes. The Voyager mission, launched in 1977, provided a substantial amount of information about the meteorology of the giant planets. Infrared spectroscopy (ground based and spaced based) has yielded information on the atmospheric thermal structure. Galileo, launched in 1989, arrived at Jupiter in 1995 with an

---

[6]Values from jpl.nasa.gov

atmospheric probe. The probe landed in an anomalous region of the atmosphere ('the Sahara desert') and did not examine a representative sample of Jupiter's atmosphere. This first in situ measurements of Jupiter's composition were carried out with the Galileo Probe Mass Spectrometer (GPMS) from 0.5 to 21 bar. The Infrared Space Observatory (ISO) (1995 - 1998) gathered significant giant planet chemical information from earth orbit, including the detection of water vapor on all four giant planets, CO_2 on Jupiter, Saturn and Neptune, benzene (C_6H_6) on Jupiter and Saturn, and diacetylene (C_4H_2) on Saturn. ISO probed the entire spectrum of Jupiter and Saturn from 2.3 μm to 180 μm, leading to a new determination of the D/H ratio, updated thermal profiles, and vertical mixing information. The Cassini spacecraft, arriving at Saturn in 2004, was the first spacecraft to investigate the Saturnian system from orbit and launched a probe into Titan in early 2005, examining the atmospheric composition of the 'early Earth'.

The problem that arises with massive data acquisition is the physical interpretation. The long orbital periods of these planets makes annual monitoring challenging. Likewise, each data set is individually analyzed, but not necessarily with equivalent model assumptions and parameters. Modeling has improved significantly over the last 20 years due to increased knowledge of molecular line data, observational information, and better assumptions. However, basic radiative seasonal climate models for Saturn remain historically inaccurate in their current seasonal predictions. Little seasonal modeling has been done for Neptune (Sromovsky and Fry 2003) and the ex-

6

amination of seasonal variability of Uranus has just recently scratched the surface (Sromovsky et al. 2006; Friedson and Ingersoll 1987; Sussman et al. 2007). Significantly more modeling has been done for Jupiter (deep convection, dynamics) and the extra-solar 'Hot Jupiters' (e.g. Showman et al. 2008; Irwin et al. 1997; Sugiyama et al. 2007).

General Circulation Models, or Global Climate Models (GCMs), have been implemented for terrestrial planets (e.g. NASA GISS (del Genio et al. 1983)), giant planet studies (e.g. Explicit Planetary Isentropic-Coordinate model (EPIC) (Dowling et al. 1998; Dowling 1993)) and, more recently, for extra-solar planets (Showman et al. 2007). These three-dimensional models are ideal for climate studies and weather forecasting and have existed for Earth-based studies as early as the 1960s (e.g. Manabe and Strickler (1964); Manabe and Bryan (1969)). GCMs are designed to provide a coherent image of atmospheres. The primary use of these computationally intensive numerical models is to investigate the climate sensitivity and responsivity to changes in solar forcing, chemistry and, for Earth, the effects of anthropogenic interaction. GCMs have been implemented (Kaspi and Flierl 2006) extensively for Jupiter (Morales-Juberías et al. 2003; Lebeau and Dowling 1998 e.g.) and recently for Uranus (Sussman et al. 2007), Venus (Dowling and Herrnstein 2006; Colón and Dowling 2000), and Neptune (Stratman et al. 2001; Lebeau and Dowling 1998). Predominantly, GCMs examine dynamics (winds) and how winds change due to different forcing mechanisms. Disentangling the contributions from individual mechanisms can be difficult. GCM model results

7

are largely predetermined by input parameterizations for radiation and chemistry. The development and maintenance of a GCM is costly in time and money, requiring extensive super computing resources. Since the models that assume radiative balance between thermal emission and solar absorption in the stratospheres of giant planets have not been updated since the Voyager era (Bézard and Gautier 1985; Cess and Caldwell 1979), a comprehensive radiative seasonal climate model would prove useful for constraining properties of stratospheric radiative forcing. Specifically, seasonal heating and cooling rates in the stratosphere are necessary for inclusion in GCMs and will assist in the development of and results obtained from these models.

The research presented in this dissertation satisfies the need for an updated seasonal climate model. Within the context of this work, Saturn is the main planet of interest, due to the current influx of Cassini and ground based data and observed atmospheric trends (discussed in Chapter 2). However, this model can easily be adapted to other giant planets if orbital and photochemical information are known. The next few sections will provide a brief background in atmospheric structure, photochemistry and the incentive for and allure of stratospheric modeling.

1.3   Atmospheric Structure & Seasons

Seasons are the product of a planet's axial tilt. Earth's axial tilt of 23.4° results in the seasons we are familiar with; summer (summer solstice), winter (winter solstice), fall (autumnal equinox), and spring (vernal equinox). The

3.1° axial tilt of Jupiter produces little to no annual variation in temperature, whereas the tilts of Saturn, Uranus, and Neptune (26.7°, 97.8°, 28.3° respectively) result in significant seasonal variability in temperature and chemistry (Moses and Greathouse 2005; Orton et al. 2007; Hammel et al. 2003, 2007). Seasonal nomenclature, L_s, is defined in Appendix A.1.

An atmosphere may be defined as a gaseous envelope surrounding a core of material. This compressible molecular mixture can adhere to the planet due to the planet's gravitational force: the greater the planet's gravity, the longer the atmosphere is retained. A planet with a large gravity can also retain an abundance of low mass molecules. The large gravitational forces of the giant planets enable them to retain hydrogen and helium in their atmospheres, unlike smaller terrestrial planets such as the Earth. The colder the planet (i.e. farther from the Sun), the smaller the thermal motions of the atmospheric gas molecules. This also assists planets in retaining low mass molecules. This holds true for Titan which is distant enough from the Sun to retain a substantial atmosphere despite its low gravity.

A particle may escape from an atmosphere if its kinetic energy exceeds the gravitational binding energy and if the particle can move in an upward trajectory unimpeded by another atom or molecule. Escape occurs in the region of the atmosphere referred to as the exosphere. The base of the exosphere (exobase) is determined to be at the altitude z where

$$\int_z^\infty \sigma_X n(z')dz' \approx \sigma_X n(z)H = 1. \tag{1.1}$$

Here, σ_X is the collisional cross section, $n(z)$ is the number density at altitude z of the species, and H is the scale height (see Equation 1.11 for derivation of the scale height). Since the mean free path l_{mfp} is

$$l_{mfp} = 1/(\sigma_X n), \tag{1.2}$$

the exobase can be defined as $l_{mfp}(z) = H$. Therefore, the mean free path for a species in the exosphere is equal to the atmospheric scale height.

In thermal equilibrium, velocities of individual molecules of mass m are given by the Maxwellian distribution

$$f(v)dv = n \left(\frac{2}{\pi}\right)^{1/2} \left(\frac{m}{kT}\right)^{3/2} v^2 e^{-mv^2/(2kT)} dv, \tag{1.3}$$

with particle velocity v. To test whether a gas particle will escape from the planet, a simple comparison between the average thermal speed (based on a Maxwell-Boltzmann distribution of speeds), which depends on the mass of the particle and temperature, and the escape velocity of the planet may be made:

$$v_{esc} = \sqrt{\frac{2GM}{R}} \tag{1.4}$$

$$\langle v_{thermal} \rangle = \sqrt{\frac{2kT}{m}}. \tag{1.5}$$

The gravitational constant is G, the mass of the planet is M, R is the planet's radius, k is the Boltzmann constant, and m is the mass of the species. A gaseous species can escape if the speeds of the particles on the tail of the Maxwell-Boltzmann distribution exceed the escape speed, or

$$T_{esc} = \alpha \frac{GMm}{kR}, \tag{1.6}$$

10

where α is $1/\lambda_{escape}$. For atomic hydrogen on Earth, $\lambda_{escape} \sim 8$ (de Pater and Lissauer 2001). At or below the exobase, particle collisions drive the velocity distribution into a Maxwellian distribution. Above the exobase, particle collisions are minimal. The rate for atmospheric escape (atoms cm^{-2} s^{-1}) by thermal evaporation (Jeans escape) can be derived from integrating the upward flux in a Maxwellian velocity distribution (Eqn.1.3)

$$\Phi_J = \frac{n(z)v_o}{2\sqrt{\pi}}(1 + \lambda_{escape})e^{-\lambda_{escape}}. \qquad (1.7)$$

The temperature versus pressure (altitude) profile of an atmosphere is controlled by the absorption of energy from the Sun, reflection of visible radiation to space, and internal thermal emission, which may be partially absorbed by the atmosphere and re-emitted to space. The profile details the thermal changes in the atmosphere as a function of pressure (or altitude). Most planetary atmospheres may be divided up into the convective troposphere, the radiative stratosphere and the mesosphere[7]. Figure 1.1 shows a sample temperature-pressure profile for Saturn illustrating these atmospheric divisions.

Deep inside a planet's atmosphere, or at the surface for terrestrial planets, and working outward, atmospheric temperature decreases with decreasing pressure (increasing altitude). This region of the atmosphere, called the troposphere (yellow, Fig. 1.1), is highly unstable and energy is transferred via

---

[7]Additional components include the ionosphere, the exosphere and the magnetosphere, but are not included in the discussion here since they are irrelevant to this research.
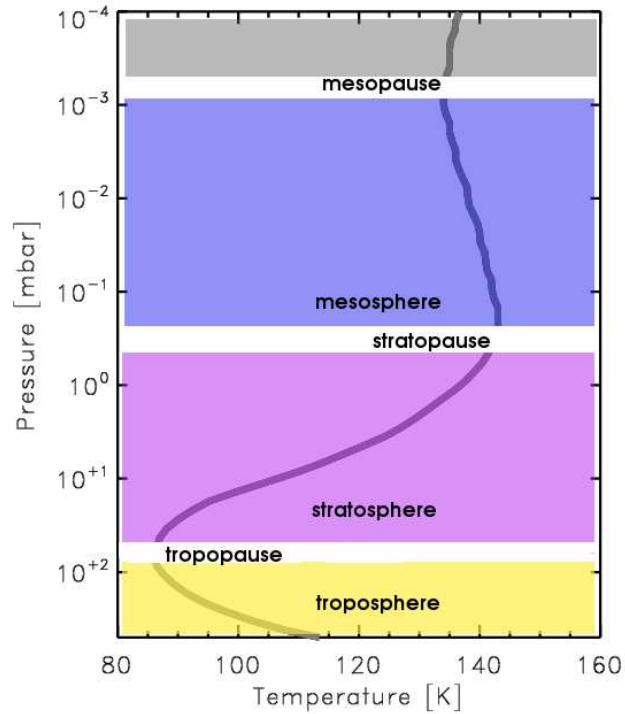
Figure 1.1: An average temperature-pressure profile of Saturn generated for this research illustrating the stratosphere, mesosphere, and troposphere and their respective inversion layers.

convective motions and radiation. A gas parcel that is warmer than the air above it will rise, cool, and sink. This cyclical pattern repeats producing convection. The hot lower troposphere is a direct physical result of internal heat generated from within the planet combined with any trapped emission from above (solar radiation, exothermic chemical reactions, etc). The troposphere is capped by the tropopause inversion.

Above the tropopause exists the stratosphere. The stratosphere is char-

acterized by enhanced heating with increasing altitude (decreasing pressure) (pink, Fig. 1.1). This region of the atmosphere is stable due to warmer gas residing on top of cooler gas. Temperatures are determined by the radiative balance between heating due to absorption of solar radiation and cooling via mid- (600 - 1600 cm^{-1}) and far-infrared (0 - 600 cm^{-1}) emission. As pressure decreases, working towards the top of the atmosphere, an increasing amount of solar radiation is available for absorption and the atmosphere becomes warmer. In the case of the Saturn, it is near-infrared CH_4 which is responsible for absorption of solar radiation throughout the stratosphere (this work, Chapter 2). Methane is photochemically sensitive (see Section 1.4). For Saturn, the vertical abundance of CH_4 in the atmosphere remains fairly constant (e.g. Bézard and Gautier 1985; Moses and Greathouse 2005; Moses et al. 2000). The amount of sunlight available, due to seasonal changes in insolation, will determine the photolysis rates which regulate the amount of methane destroyed in the upper atmosphere. Methane destruction results in the production of free radicals which will later combine to form more complex hydrocarbons such as C_2H_2 and C_2H_6.

The mesosphere is coupled to the stratosphere by another thermal inversion, the stratopause. For Earth, this inversion is due to solar ultraviolet absorption by O_3. The mesosphere is characterized by decreasing temperatures with increasing altitude. Evidence for the existence of a mesopause on Saturn was recently shown by (Greathouse et al. 2005b) from distinct self-absorption cores on top of strong CH_4 emission lines.

For giant atmospheres, it is convenient to define the atmosphere in terms of pressure (p) rather than altitude (z), due to the lack of a physical surface. Pressure and altitude are related via the hydrostatic equation

$$\frac{dp}{dz} = -\rho g, \tag{1.8}$$

where ρ is the mass density and g is the acceleration due to gravity. For an ideal gas, the pressure is given as

$$p = nkT, \tag{1.9}$$

where n is the number density, k is the Boltzmann constant and T is temperature. The mass density in terms of the number density is

$$\rho = mn \tag{1.10}$$

with m as the mean molecular mass. Combining these three equations, the atmospheric scale height (H) can be derived

$$\frac{dp}{p} = -\frac{dz}{H} \tag{1.11}$$

with $H = kT/mg$. The solution to Eq. 1.11 is

$$p(z) = p(z_o) \exp\left(-\int_{z_o}^{z} \frac{dz}{H}\right). \tag{1.12}$$

This solution states that atmospheric pressure exponentially decays in the vertical direction, as a function of atmospheric scale height. For comparison purposes, the atmospheric scale heights for Saturn, Jupiter, Uranus, Neptune and

Earth are 59.5 km, 27.0 km, 19.1 km, 27.7 km, and 8.4 km[8] (Yung and Demore 1999).

Figure 1.2 shows the calculated scale height for an average Saturnian temperature-pressure profile (this work). The atmospheric molecular weight is assumed to be 0.00226 kg mol^{-1} and gravity is assumed to be 9 m s^{-2}.
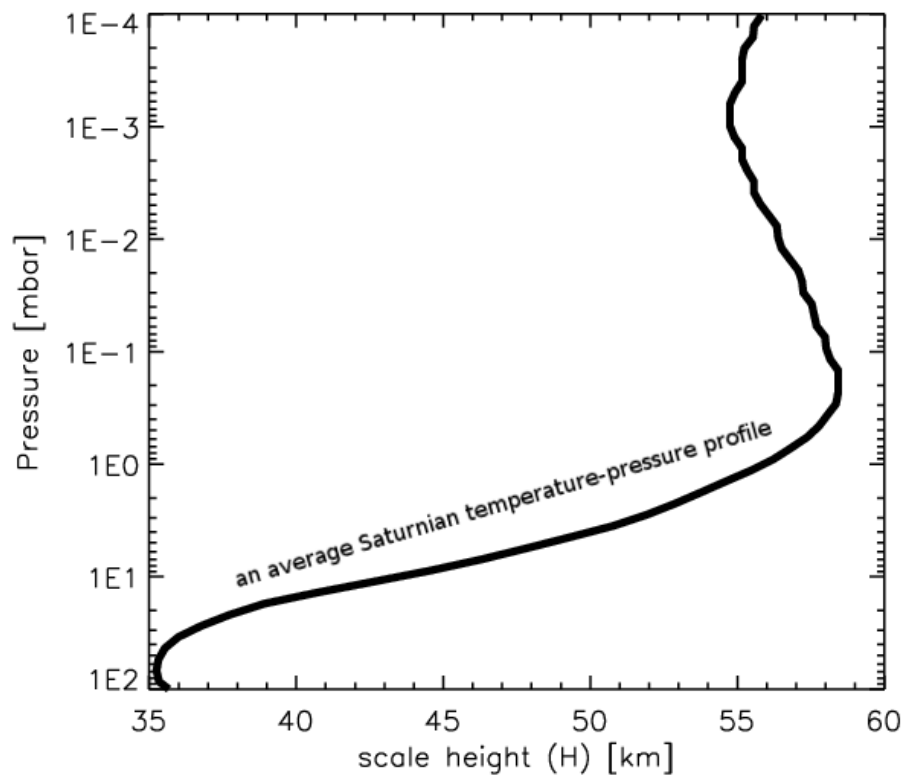
Figure 1.2: Saturnian scale height

---

[8]All values of H are based on an atmospheric pressure of 1 bar

We can examine energy balance within the atmosphere with the equation

$$-\frac{C_p}{g}\frac{dT}{dt} + \frac{d\phi_c}{dp} + \frac{d\phi_k}{dp} = \frac{dF}{dp}, \qquad (1.13)$$

where C_p is the heat capacity per unit mass at constant pressure, dF/dp is the net heating rate which may be defined as the (rate of heating) - (the rate of cooling), ϕ_c is the conduction heat flux in the upper ionosphere/thermosphere, and ϕ_k is the convection heat flux. The conduction heat flux is

$$\phi_c = \kappa\frac{dT}{dp}\rho g, \qquad (1.14)$$

where κ is the thermal conductivity of the atmosphere for a given pressure and temperature ($\kappa = (2kT/m)^{1/2}mC_p/\sigma$). For Saturn, at -8° latitude and autumnal equinox, κ at 0.1 mbar and 140 K is 0.39 W m^{-1} K^{-1}. C$_p$ is assumed to be a constant 24.43 J K^{-1} mol^{-1}, the molecular weight of the atmosphere is 0.00226 kg mol^{-1}, and the cross section of H$_2$ is $\sigma = 10^{-19}$ m^2. Throughout the stratosphere, κ varies between 0.3 and 0.4 W m^{-1} K^{-1} with the above assumptions. Between 1 and 0.001 mbar, dT/dp is 5.0 K/mbar (0.05 K/Pa) and between 100 and 1 mbar, dT/dp is -0.6 K/mbar (-0.006 K/Pa) based on the temperature-pressure profile Fig. 1.1. If we assume a number density of 10^{20} m^{-3} (an approximate value from this work), an H$_2$ mole fraction of 0.88 (where $0.88n$ is the number density of H$_2$), and m$_{H2} = 3.3 \times 10^{-27}$ kg, $\phi_c = 5 \times 10^{-8}$ W m^{-2} between 1 and 0.001 mbar and $\phi_c = -5 \times 10^{-9}$ W m^{-2} between 100 and 1 mbar (for an average temperature of 100 K between 100 and 1 mbar). Between pressures 100 and 0.001 mbar, $d\phi_c/dp$ is -6×10^{-12} W m^{-2}/Pa.

The convection heat flux is

$$\phi_k = K_H \rho C_p \left(\frac{dT}{dp} \rho g - \frac{g}{C_p} \right), \qquad (1.15)$$

with the eddy diffusion coefficient K_H[9]. K_H is of order 2×10^5 cm^2 s^{-1} for 0.1 mbar (from Moses et al. (2005), Model "C" for Saturn, Figure 31.). The eddy diffusion coefficient varies significantly with dp (between 500 and 1×10^6 cm^2 s^{-1} for the pressure range 100 to 0.001 mbar) (Moses et al. 2005). Taking the K_H value at 0.1 mbar, ϕ_k between 1 and 0.001 mbar is -5$\times 10^{-5}$ W m^{-2}. For $K_H(10$ mbar$) \sim 2000$ cm^2 s^{-1}, ϕ_k between 100 and 1 mbar is -5$\times 10^{-7}$ W m^{-2}. For pressures 100 to 0.001 mbar, the value of $d\phi_k/dp = 5 \times 10^{-9}$ W m^{-2}/Pa.

The first term (radiative component) in Eqn. 1.13 is 0.05 W m^{-2}/Pa, assuming a net heating rate of 500 J m^{-2} mbar^{-1} day^{-1} in the lower stratosphere (Chapter 2. Figs. 2.5 and 2.6). Using a net heating rate of 1000 J m^{-2} mbar^{-1} day^{-1} in the mid-stratosphere, the first term becomes 0.1 W m^{-2}/Pa. Comparing the three terms, it is then obvious that both $d\phi_c/dp$ and $d\phi_k/dp$ may be neglected in the stratosphere. We do consider an internal energy source at the bottom boundary of the stratospheric model. For Saturn, the temperature of the energy source is equivalent to the difference between the blackbody temperature resulting from the upward emitted flux of 4.7 W m^{-2}, from Voyager measurements (Bézard et al. 1985), minus the downward flux from the bottom boundary of the model.

---

[9]Eddy diffusion describes the turbulent mixing of atmospheric gases. Because this process is complex and not observationally constrained, the eddy diffusion is parameterized as a function of pressure by the eddy diffusion coefficient K_H

1.4 Photochemistry

In the upper atmospheres of planets, photochemistry assists in the regulation of climate change. Photodissociation (photolysis) is the destruction of molecules by solar photons energetic enough to break molecular bonds. Photons in the visible to gamma ray range have enough energy to photo-dissociate molecules.

On Earth, two of the most common photodissociation reactions occur in the stratosphere: (1) the destruction of ozone (O_3) by photons with $\nu > 31250$ cm^{-1} which leads to the generation of hydroxyl radicals,

$$O_3 + h\nu \rightarrow O_2 + O(^1D)$$
$$O(^1D) + H_2O \rightarrow 2OH, \tag{1.16}$$
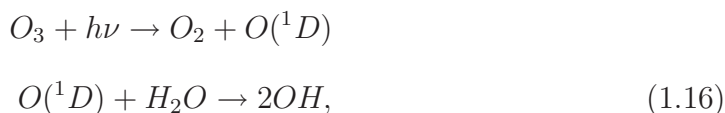
and (2) the formation of tropospheric ozone,

$$NO_2 + h\nu \rightarrow NO + O$$
$$O + O_2 \rightarrow O_3. \tag{1.17}$$
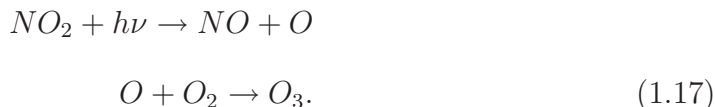
The hydroxyl radical in Eq. 1.16 aides in initiating the oxidation of hydrocarbons, riding the atmosphere of pollutants. The ozone layer in the Earth's stratosphere is a direct product of photodissociation as well. Incident ultraviolet light strikes existing O_2 molecules and splits them into atomic oxygen. Atomic oxygen can then combine with existing O_2 to form O_3. As a negative effect, photolysis also results in the production of ozone-destroying chlorine radicals from CFCs.

For Saturn, hydrocarbon photochemistry alters atmospheric temperatures based on changes in insolation due to season and orbital position (see Chapter 2). Despite the fact that the atmospheres of gas giant planets contain less then 1% methane (CH_4), methane plays a dominant role in regulating the atmospheric temperature variability of Saturn. Methane photochemical byproducts, ethane (C_2H_6) and acetylene (C_2H_2), are Saturn's main stratospheric coolants while methane itself dominates in solar absorption. Figure 1.3 displays synthetic spectra derived from ISO-SWS observations of Saturn for 7 to 15 μm (1428.6 to 667 cm^{-1}) (de Graauw et al. 1997). Notably, the C_2H_2 and C_2H_6 flux is close to an order of magnitude larger then the CH_4 emission. Phosphine (PH_3) is a dominant absorber at tropospheric levels but does not affect stratospheric temperatures (PH_3 lies in a spectral region void of stratospheric emitters/absorbers, so changes in the upward-going blackbody emission due to PH_3 absorption does not affect the stratospheric energy balance).

Methane is the most abundant hydrocarbon in the outer solar system. For $\nu < 69000$ cm^{-1}, the CH_4 cross section is negligible due to not having low-lying dissociation states (similar to H_2) and is photochemically inactive at $\nu < 69000$ cm^{-1}. The photodissociation absorption cross section spectrum of C_2H_6 is similar to CH_4. Those of C_2H_2 and C_2H_4 extend to 50000 and 45400 cm^{-1}, respectively, enabling dissociation by solar absorption to longer wavelengths than CH_4. Absorption of photons shortward of 69000 cm^{-1} by CH_4 can lead to production of photochemical byproducts. These byproducts
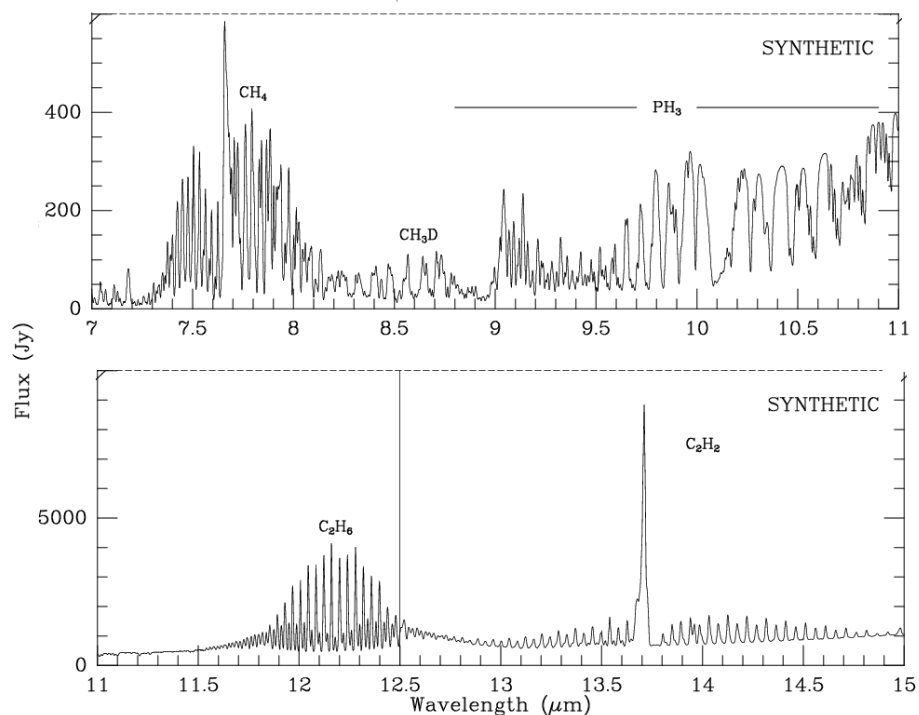
Figure 1.3: Mid-infrared ISO SWS synthetic spectra of C_2H_2, C_2H_6, CH_4 (de Graauw et al. 1997)

can later absorb radiation at longer wavelengths. For C_2H_2, photolysis of this molecule results in new photochemical reactions which may break apart the CH_4 molecule, also known as the photosynthesized dissociation of CH_4 (Yung and Demore 1999).

Due to the fact that CH_4 is the most abundant carbon species in the atmosphere and shares a similar absorption cross section with ethane, CH_4 acts to shield C_2H_6 from incident sunlight, possibly increasing the lifetime

20

of C_2H_6. This act of shielding can alter the heating and cooling balance of the stratosphere. Hence it is not only the reaction chemistry that defines the climate within the atmosphere, but also the inherent interplay between molecules and their individual properties.

We can explicitly determine the volume absorption rate (r_i) for a species (i) as a function of altitude (z) in the atmosphere:

$$r_i(z) = J_i(z)n_i(z) \tag{1.18}$$

with

$$J_i(z) = \int \sigma_i(\nu)F(z,\nu)d\nu \tag{1.19}$$

as the photodissociation coefficient. The number density of the chemical species is given by n_i and σ_i is the absorption cross section for frequency ν.

As a basic example, from Yung and Demore (1999), consider a monochromatic beam of light incident on an isothermal[10], plane-parallel atmosphere containing a single molecular species. This species may absorb sunlight. Its number density in the atmosphere is

$$n(z) = n_o e^{-z/H} \tag{1.20}$$

where H is the scale height. For the optical depth $\tau(z)$, where

$$\tau(z) = \int_z^\infty n(z)\sigma_i dz, \tag{1.21}$$

---

[10]constant temperature

21

and the attenuated solar flux that enters the atmosphere at zenith angle θ,

$$F(z) = F(\infty)e^{-\tau(z)/\cos\theta}, \tag{1.22}$$

the volume absorption rate becomes

$$r(z) = n_o \sigma F(\infty)e^{-z/H - \alpha e^{-z/H}}, \tag{1.23}$$

with $\alpha = \sigma H n_o \cos\theta$.

1.4.1 Why Model the Stratosphere?

The subsequent chapters focus on the detailed creation of an updated radiative seasonal climate model for stratospheric application. This raises the question, 'Why the stratosphere (and not the troposphere...)?'.

The stratosphere can be assumed to be devoid of non-Local Thermodynamic Equilibrium (nLTE) processes. Circulation, although disputed (Flasar et al. 2005), may not play a substantial role in stratospheric thermal regulation (see Chapter 2), at least in the case of Saturn. Arguably, the stratosphere may be modeled via basic radiative processes, simplifying mathematical computations, assumptions, and analysis. From Eq. 1.13, we need only be concerned with the $\rho C_p dT/dt = q$ term (in addition to an internal upward energy source) which is advantageous in computational modeling.

Additionally, many observationally derived temperatures in Saturn's atmosphere are confined to the upper troposphere and stratosphere (Greathouse et al. 2005a,b; Orton et al. 2005; Flasar et al. 2005; and Howett et al.

2007), requiring an updated stratospheric seasonal climate model to compare to. Similarly, in order to thoroughly examine recent observations of Uranus and Neptune (Hammel et al. 2007, 1992, 2003), a comparable seasonal model is appropriate.

Temporally constraining the stratospheric responsivity to changes in seasonal insolation and chemistry would directly assist in providing a better baseline to distinguish between the radiative and dynamical roles in the stratosphere and aide in the future development of a comprehensive GCM. The discrete roles played by radiation and dynamics in Saturn's stratosphere are not well characterized. How these processes drive composition and chemistry, and the extent that chemistry drives seasonal temperature variations, are uncertain. Investigating local radiative balance in the stratosphere is critical to the understanding of giant planet atmospheres (Yelle et al. 2001).

Giant planet stratospheres also provide a unique, simplified 'laboratory' with which to study the responsivity of the atmosphere to seasonal photochemistry and solar forcing in the stratosphere. As a hotbed of photochemical activity, the stratosphere provides a direct means to investigate the seasonal effects of photochemical production and loss. For the Earth, quantifying the impact of anthropogenically induced climate change is crucial to understanding the natural variability of our climate system (Palmer et al. 2002). However, the mechanisms through which changes in the seasonal solar irradiance are transmitted to the lower atmosphere are not well characterized. In particular, the extent that photochemical changes within the stratosphere effect the global

23

climate and conditions for life are of immediate interest. By studying the seasonal effects in the pure laboratory source of the giant planet atmospheres, consequences and conclusions may be revealed for the more complicated Earth environment.

Chapter 2

The Radiative Seasonal Climate Model: Saturn

2.1 Abstract

In this work, I present an improved multilayer radiative seasonal climate model for the study of Saturnian stratospheric temperatures. Motivated by current Cassini and ground-based observations of an enhancement of hydrocarbon emission from equator to south pole (Greathouse et al. 2005a,b; Orton et al. 2005; Flasar et al. 2005; and Howett et al. 2007), this research illustrates the Saturnian stratospheric thermal dependency on near-infrared CH_4 parameterization. The Irwin et al. (2006) k-coefficients are currently the most complete CH_4 near-infrared opacity data set for $4800 < \nu \leq 9500$ cm^{-1}; exact line transitions for this region remain qualitative (Brown 2005). Implementation of the Irwin et al. (2006) k-coefficients in this model does not result in the reproduction of the Greathouse et al. (2005a) $p = 5$ mbar equator-to-south pole observational trends for 2002. We find the equator-to-south pole thermal gradient to be pressure dependent. The HITRAN04 + GEISA03 CH_4 near-infrared opacity data set plus an inclusion of aerosol opacity results in the reproduction of the 2002 and 2004 observational equatorial-to-south pole thermal enhancements, despite the incomplete shortwave near-infrared GEISA03

line list. This line data set produces CH_4 spectra (1247 - 1251 cm^{-1}) that is warmer than TEXES data at the same epoch by 6 K. The thermal gradient dependency on CH_4 near-IR parameterization suggests that for exact stratospheric seasonal modeling, the acquisition of shortwave near-infrared CH_4 line data is imperative. This research does not disprove the meridional redistribution of photochemical species. Such a redistribution could alter the radiative balance of the stratosphere. Atmospheric thermal lags are significantly faster (peak temperatures occur < 5 Earth years from summer solstice for $p \leq 10$ mbar) than previously determined. This model incorporates stratospheric heating due to CH_4 (near-infrared, visible, ultraviolet), C_2H_2 (ultraviolet), C_2H_4 (ultraviolet), and C_2H_6 (ultraviolet) absorption of sunlight and cooling from CH_4, C_2H_2, and C_2H_6 line emission combined with H_2-H_2, H_2-He, and H_2-CH_4 collision induced continuum emissions within the spectral range of 0 to 10^5 cm^{-1}. Temporally, meridionally, and vertically variable hydrocarbon abundances are included to best approximate the seasonal stratospheric radiative responsivity.

2.2   Introduction

Analogous to the Earth, the 26.7° axial tilt of Saturn results in seasonal forcing. One Saturn year is equivalent to 29.5 Earth years, making observations of annual seasonal variability challenging. As of January 2008, Saturn's season is approximately 6 years beyond southern summer solstice ($L_s \sim 340°$). Observations spanning the Cassini mission's lifetime (2004 - 2008) have been

optimal for constraining the peak stratospheric seasonal temperatures at high southern latitudes since the last southern summer solstice in 1972 (Howett et al. 2007; Greathouse et al. 2005a,b; Flasar et al. 2005; Fletcher et al. 2007, Orton et al. 2005). These observations have indicated a persistent enhancement in hydrocarbon emission at the south pole relative to the equator beginning as early as southern summer solstice (2002) to present.

Temporally constraining the peak temperatures as a function of atmospheric pressure would directly reveal the seasonal responsivity of the stratosphere and assist in providing a better baseline to distinguish between the radiative and dynamical roles in the stratosphere. The discrete roles played by radiation and dynamics in Saturn's stratosphere are not well characterized. How these processes drive composition and chemistry, and the extent that chemistry drives seasonal temperature variations, are uncertain. Investigating local radiative balance in the stratosphere is critical to the understanding of giant planet atmospheres (Yelle et al. 2001).

Flasar et al. (2005) suggest that Saturnian climate models require upwelling at the equator and subsidence at the poles in order to reproduce the observed stratospheric temperature trends, since past radiative equilibrium models have failed to mimic both the observed seasonal phase lags and thermal trends (Bézard and Gautier 1985; Cess and Caldwell 1979; Conrath et al. 1990). Past radiative equilibrium models lacked knowledge of the recently updated near-infrared (near-IR) CH_4 absorption parameters (Irwin et al. 2006; Sromovsky et al. 2006), seasonal photochemistry (Moses et al. 2007), and the

updated $[CH_4]/[H_2]$ abundance (Flasar et al. 2005). Including this knowledge in an improved radiative seasonal model for the Saturnian stratosphere may correctly model the observed behavior without necessitating the inclusion of dynamics.

In this chapter, a new radiative seasonal climate model for Saturn's stratosphere is presented that includes the transfer of radiation with wavenumbers from 0 to 10^5 cm^{-1}. Temporally, meridionally, and vertically (TMV) variable hydrocarbon abundances, as determined by Moses et al. (2007) and constrained by Greathouse et al. (2005a), have been included. TMV model results are contrasted with constant hydrocarbon abundances in models like Bézard and Gautier (1985). This investigation focuses on the seasonal temperature variation for Saturn's stratospheric southern hemisphere, in the absence of stratospheric scatterers. The thermal effects of aerosol opacity (Moses, this paper) are examined. Section 2.3 discusses past radiative seasonal models, Section 2.4 details the implementation of photochemical data from Moses et al. (2007), and Section 2.6 provides an overview of the model. Sections 2.6.1 and 2.6.2 detail the calculations and computational assumptions for the cooling and heating components of the radiative seasonal model.

2.3 Previous Radiative Equilibrium Models

Saturnian southern summer observations by Greathouse et al. (2005a,b) in 2002 and 2004 showed a positive emission gradient from the equator to the south pole in the ν_4 band of CH$_4$ at 0.1 mbar. Greathouse et al. (2005a,b)

linked the emission enhancement of CH_4 ν_4 at the pole to a seasonal temperature enhancement between 10 and 0.01 mbar in 2002 and between 5 and 0.1 mbar in 2004. We will define $+\zeta_g$ as the trend of increasing temperature from equator to south pole in units of K. Zonally averaged temperatures derived in 2004 from Cassini CIRS observations (Flasar et al. 2005; Howett et al. 2007) also infer a comparable sustained thermal gradient ($+15$ K at 1 mbar, $+20$ K at 3 to 5 mbar, and $+14$ K at 2 mbar), as did 2004 Keck observations (Orton and Yanamandra-Fisher 2005) ($+10$ K at 3 mbar). These observations are consistent with emission enhancements in the ν_4 band of methane and the ν_9 band of ethane observed 30 years prior (Tokunaga et al. 1978; Gillett and Orton 1975; Rieke 1975). The ζ_g values from observations are shown in Table 2.1.

The Voyager-era radiative seasonal models reproduced derived thermal trends from 1978-1981 observations, but failed to predict the observed trends 25 years later. The stratospheric seasonal model of Cess and Caldwell (1979) was constructed to analyze the CH_4 emission enhancement seen in the pre-Voyager observations (Tokunaga et al. 1978; Gillett and Orton 1975; Rieke 1975). This model consistently replicated southern hemisphere emission trends observed by Tokunaga et al. (1978). However, the model predicted that the equator would be warmer than the pole at southern summer solstice in 2002 (Table 2.1). Likewise, the Bézard and Gautier (1985) multi-layer, monochromatic radiative transfer model for Saturn's stratosphere was developed following the 1980 and 1981 (southern autumnal equinox) Voyager 1 and 2 encounters

29

	$\zeta_g(2002)$ [K]	P [mbar]	$\zeta_g(2004)$ [K]	P [mbar]	$t(\mathrm{T}_{max})$ [yr]
Radiative Equilibrium Model					
Cess & Caldwell (1979)	-5	5	+1	5	2008/2009
Bézard & Gautier (1985)	-6	1	-2	1	2010
Observations					
Greathouse et al. (2005a)	+10	10 - 0.01			
Greathouse et al. (2005b)			+15	5 - 0.1	
Howett et al. (2007)			+14	2	
Flasar et al. (2005)			+15	1	
			+20	3 - 5	
Fletcher et al. (2007)			+16	1	
			+15	5	
Orton and Yanamandra-Fisher (2005)			+10	3	

Table 2.1: The thermal gradient (ζ_g) from equator to south pole from past radiative models and recent observations. A positive ζ_g value indicates that the south pole is warmer than equator. The model-predicted maximum temperatures occur in the year $t(T_max)$, following the peak solar forcing in 2002.

of Saturn. The model reproduced the Voyager 1 ingress ($-76°$) and Voyager 2 ingress ($36.5°$) observations within error for stratospheric pressures of 0.1 to 50 mbar. Nevertheless, this model also forecast the warmer equator than south pole for 2002 (Table 2.1). As seen in Fig. 2.1, the Bézard and Gautier (1985) model predicted no thermal gradient between equator and south pole while the Cess and Caldwell (1979) model predicts a small negative equator to pole thermal enhancement (Fig. 2.1). Both model predictions are inconsistent with ground and space-based findings from 2002 - 2004 (Greathouse et al. 2005a,b; Orton et al. 2005; Flasar et al. 2005; and Howett et al. 2007).

The thermal response of the Saturnian stratosphere lags the solar forcing by a phase shift $\xi = \tan^{-1} \omega_s \tau_r$, where ω_s is the seasonal frequency (2π/Saturn year) and τ_r is the radiative time constant (Conrath and Pirraglia 1983). This response time is estimated from the Newtonian cooling approximation and the timescale for radiative damping in the atmosphere (Goody 1964, chap. 9). Knowledge of the pressure dependency of ξ is limited to the Conrath et al. (1990) (0.1 - 100 mbar) and Conrath and Pirraglia (1983) (100 - 1000 mbar) models. The Conrath et al. (1990) model exhibits a constant $\omega_s \tau_r$ from 0.1 to 100 mbar corresponding to $\xi \sim 98°$ in (8 Earth years). This is indicative of a minimal change in seasonal phase lag with increasing pressure and thermal inertia between 0.1 to 100 mbar, and is consistent with the findings of Cess and Caldwell (1979); Bézard and Gautier (1985) (Table 2.1, $t(T_{max})$). Between 0.01 and 1 mbar, both the vertical diffusion timescale and the photochemical lifetimes are long for C_2H_2 and C_2H_6. High-altitude abundances peak
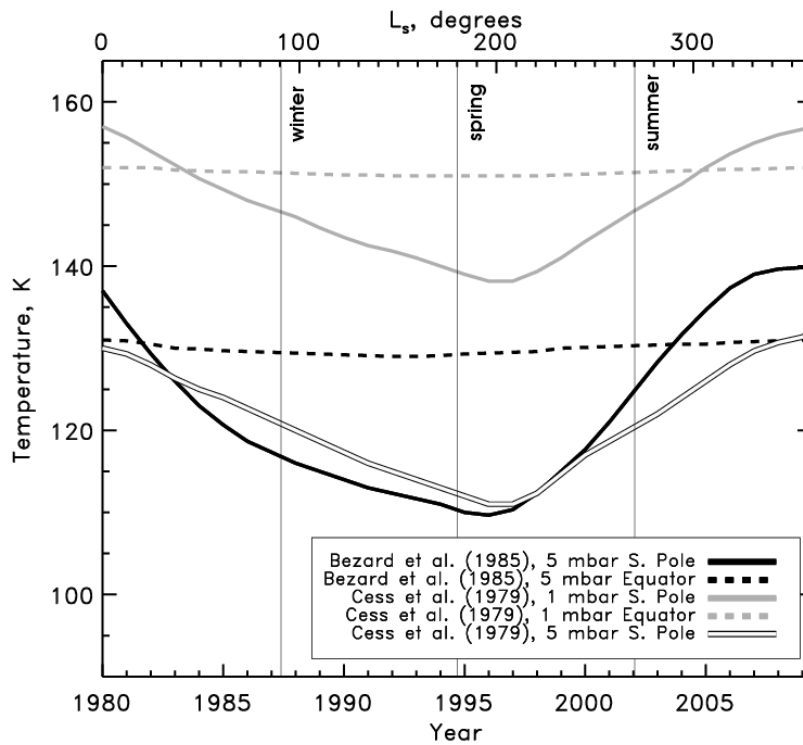
Figure 2.1: 5 mbar seasonal temperatures predicted by the Bézard et al. (1985) model at 5 mbar and the Cess et al. (1979) model at 5 and 1 mbar. Solid vertical lines indicate southern summer and winter solstices and vernal equinox. Notably, no change in seasonal phase lags exists between the 1 and 5 mbar Cess et al. (1979) model. For all three profiles, ζ_g at southern summer solstice indicates the equator is warmer than the south pole.

near summer solstice for C_2H_2 and C_2H_6, whereas deeper in the atmosphere at 0.03 mbar, C_2H_2 and C_2H_6 mole fractions are greater at autumnal equinox (see Fig. 2.2). This indicates that it has taken approximately a Saturnian season for the high altitude hydrocarbon abundances to diffuse down to the 0.03 mbar level (see similar discussion in Moses and Greathouse (2005)). For pressures

32

greater than 1 mbar, vertical diffusion timescales are longer than a Saturnian year. In Figure 2.2, little seasonal change in hydrocarbon mole fractions occurs for pressures greater than 1 mbar. Observations have yet to provide such pressure-dependent information. However, Greathouse et al. (2005b) 2004 observations showed a decrease in temperature at the 0.05 mbar level relative to 2002 temperatures. Other stratospheric pressures probed showed an increase in temperatures (Table 2.1), indicating that the seasonal phase lag is at least not pressure invariant above the 0.1 mbar level.

Both Bézard and Gautier (1985) and Cess and Caldwell (1979) adopted hydrocarbon mixing ratios that did not vary with pressure, latitude, or season. In reality, the hydrocarbon mixing ratios are dependent on pressure, season, and latitude due to transport processes and photochemical production and loss (Moses and Greathouse 2005). Further, Bézard and Gautier (1985) used a low methane mixing ratio, $[CH_4]/[H_2] = 3.5^{+1.0}_{-0.7} \times 10^{-3}$. Cess and Caldwell (1979) implemented a high methane mixing ratio, $[CH_4]/[H_2] = 7 \times 10^{-3}$ and neglected to include any C_2H_2 abundance. Courtin et al. (1984) derived a methane mixing ratio of $[CH_4]/[H_2] = 4.5^{+2.4}_{-1.9} \times 10^{-3}$, based on Voyager 2 IRIS data. From Cassini CIRS observations, the methane mixing ratio was confirmed to be $[CH_4]/[H_2] = 4.5 \pm 0.9 \times 10^{-3}$ (Flasar et al. 2005). The Cess and Caldwell (1979) model implemented a "direct cooling-to-space" method, permitting the uncoupling of layers within the atmosphere. Each layer may then be treated independently. The Bézard and Gautier (1985) model does not include this approximation, but rather was the first to incorporate a multilayer monochro-

matic radiative transfer treatment.

Arguably most critical, there remains significant uncertainty in the shortwave CH_4 near-IR (4800 - 9500 cm^{-1}) line-parameter data utilized in these radiative seasonal models. From our model calculations, 81% of the near-IR solar flux is available for absorbtion in the range 4800 - 9500 cm^{-1}. As will be discussed in Section 2.6.2, near-IR CH_4 absorption of solar radiation dominates stratospheric heating. Consequentially, precise knowledge of near-IR line parameters is imperative for correctly determining the balance between stratospheric heating and cooling. Bézard et al. (1985) used a combination of line parameters from an early GEISA compliation (Husson et al. 1982) for the 3.3- and 2.3-μm CH_4 band complexes. For the 1.7-μm CH_4 band, only $2\nu_3$ spectroscopic data existed at the time of the Bézard et al. (1985) model. Therefore, the authors multiplied the derived heating rate for the $2\nu_3$ band by three to account for two other CH_4 near-IR bands of similar intensity (1.3- and 1.1-μm bands).

We test our model with the constant hydrocarbon mole fractions of Bézard and Gautier (1985) and argue that the effects of adopting these mole fractions result in minimal inconsistencies between the seasonal models and observations (Section 2.8). Likewise, the choice of $[CH_4]/[H_2]$ cannot account for discrepancies between models and observations (Section 2.8). Rather, it is the historical use of incomplete near-IR line parameters which account for the disparities between seasonal models (Bézard and Gautier 1985; Cess and Caldwell 1979) and current observations (Howett et al. 2007; Greathouse et al. 2005a,b;

Flasar et al. 2005; Fletcher et al. 2007) (Section 2.8).

2.4 Seasonal Photochemistry

Despite the predominance of H_2 and He in the Saturnian atmosphere, CH_4 plays the dominant role in regulating stratospheric seasonal temperature variability. Methane photochemical byproducts, C_2H_2 and C_2H_6, are Saturn's main stratospheric coolants, as observed in Figure 2. of de Graauw et al. (1997), while CH_4 dominates in solar absorption. The incident solar ultraviolet flux regulates hydrocarbon production rates (Moses and Greathouse 2005). While the total abundance of CH_4 stays fairly constant throughout a Saturn year, the abundances of C_2H_2 and C_2H_6 are linked directly to the seasonal variability in insolation (Moses and Greathouse 2005). It is the balance between absorption of solar ultraviolet radiation by CH_4, C_2H_2 and C_2H_6 and visible and near-IR radiation by CH_4 combined with the thermal emission via C_2H_2, C_2H_6, and CH_4 that determines Saturnian stratospheric temperatures.
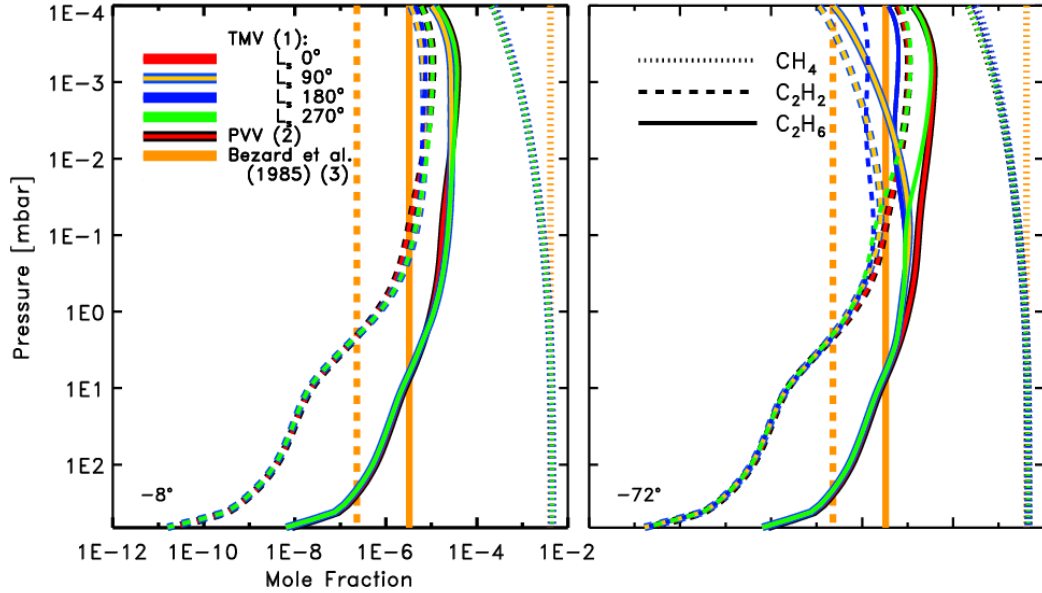
Figure 2.2: The (1) Temporally, vertically, and meridionally (TMV) varying hydrocarbon mixing ratios versus pressure for $-8°$ and $-72°$ at $L_s = 0°$ (southern autumnal equinox), $90°$ (southern winter solstice), $180°$ (southern vernal equinox), and $270°$ (southern summer solstice). The (2) pure-vertically variable mole fractions (PVV) are overplotted as are the (3) constant Bézard and Gautier (1985) mole fractions.

For our model we adopt the TMV mixing ratios for C_2H_2, C_2H_6, and CH_4 from Moses et al. (2007) (Fig. 2.2). A purely vertically variable (PVV) mole fraction, generated from Greathouse et al. (2005a) and updated by Moses and Greathouse (2005), is overplotted for comparison and was tested in the model independently of the TMV mixing ratios. The constant mole fractions used in the Bézard and Gautier (1985) model have also been tested within our model and are overlayed in orange in Fig. 2.2. We will denote the use of separate hydrocarbon parameterizations as (1) TMV, (2) PVV, and (3)

constant Bézard and Gautier (1985) mole fractions.

Figure 2.3 shows the seasonal TMV model mole fractions f r -72° (right) and -8° (left) latitudes. For -8° latitude, slight decreases in the C_2H_2 and C_2H_6 mole fractions bracketing winter coincide with ring shadowing (the same effect is illustrated in Moses and Greathouse (2005), Fig. 5.). At 3×10^{-3} mbar and -72° latitude, the decrease in C_2H_2 and C_2H_6 in winter is due to the absence of insolation. The dramatic seasonal variation in TMV mole fractions at low pressure is indicative of solar UV absorption at the top of the atmosphere. This is discussed in the following section.
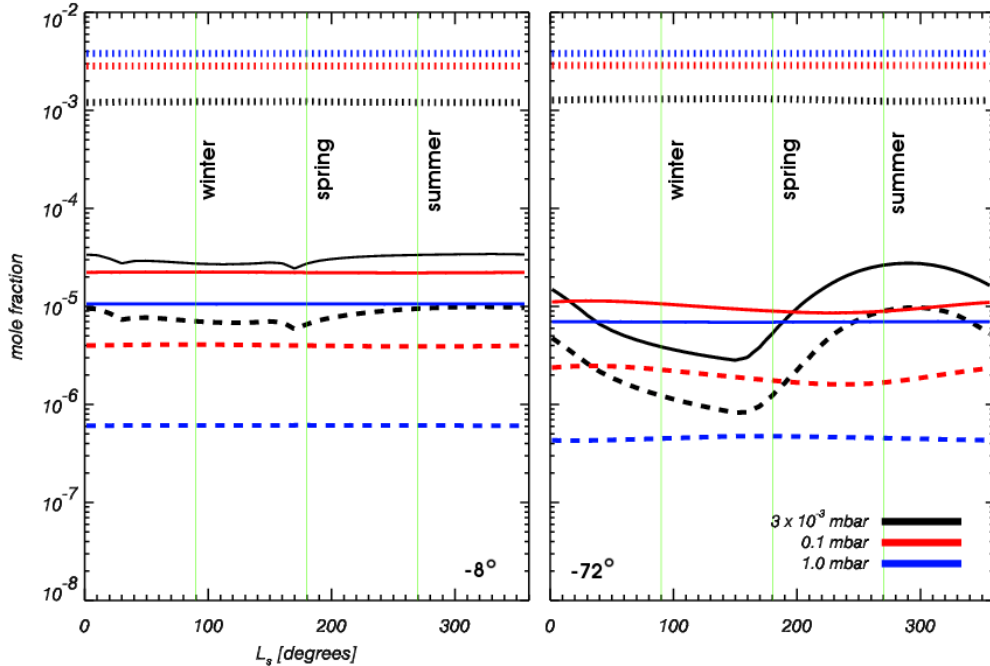
Figure 2.3: TMV mole fractions plotted as a function of season for CH_4 (dotted), C_2H_6 (solid), and C_2H_2 (dashed). Three pressure levels are shown for -72° latitude (right) and -8° latitude (left). Large seasonal variability in photochemistry are obvious near the top of our model stratosphere (3×10^{-3} mbar).

2.5 Ring Shadowing

We have adopted the Bézard (1986) formalism for ring shadowing calculations. The widths and optical depths of five ring regions are supplied (see Moses and Greathouse (2005) for further details). The B ring is divided into two components. The average normal optical depths, $\langle \tau_{ring} \rangle$, were derived from Voyager Ultraviolet Spectrometer (UVS) observations at $\tilde{\nu} = 9.1 \times 10^4$

Ring Region	$r1$ (km)	$r2$ (km)	$\langle\tau\rangle$ (UVS)
A	122340	136780	0.51
Cassini Div.	117510	122340	0.14
Outer B	98500	117510	2.07
Inner B	91975	98500	0.92
C	74655	91975	0.099

Table 2.2: Ring parameters implemented for ring shadowing following Moses and Greathouse (2005).

cm^{-1} (Sandel et al. 1982; Holberg et al. 1982). No scattered light from the rings is included; only direct absorption is considered. Table 2.2 shows the ring parameters used in the model. The inner edge radius is r_1, r_2 is the outer edge radius, and $\langle\tau_{ring}\rangle$ is the average optical depth in the region derived at an effective wavelength of 0.11 μm from Sandel et al. (1982) and Holberg et al. (1982) and at 0.26 μm from the Photopolarimeter Subsystem (PPS) data by Esposito et al. (1983).

The detailed optical depth profiles were obtained from the Planetary Data System's Ring Node (http://ringside.arc.nasa.gov). Ring averaging was performed such that

$$\langle\tau_{ring}\rangle = -ln\left[\frac{\int_{r1}^{r2} e^{-\tau_{ring}}dr}{\int_{r1}^{r2} dr}\right], \qquad (2.1)$$

where r is the radial distance from Saturn's center. Ring shadowing effects are pronounced between latitudes 10° and 40° (Moses and Greathouse 2005), shielding portions of these latitudes near winter solstice. No ring shadowing is observed at the equator and poles (Fig. 2.4).

39
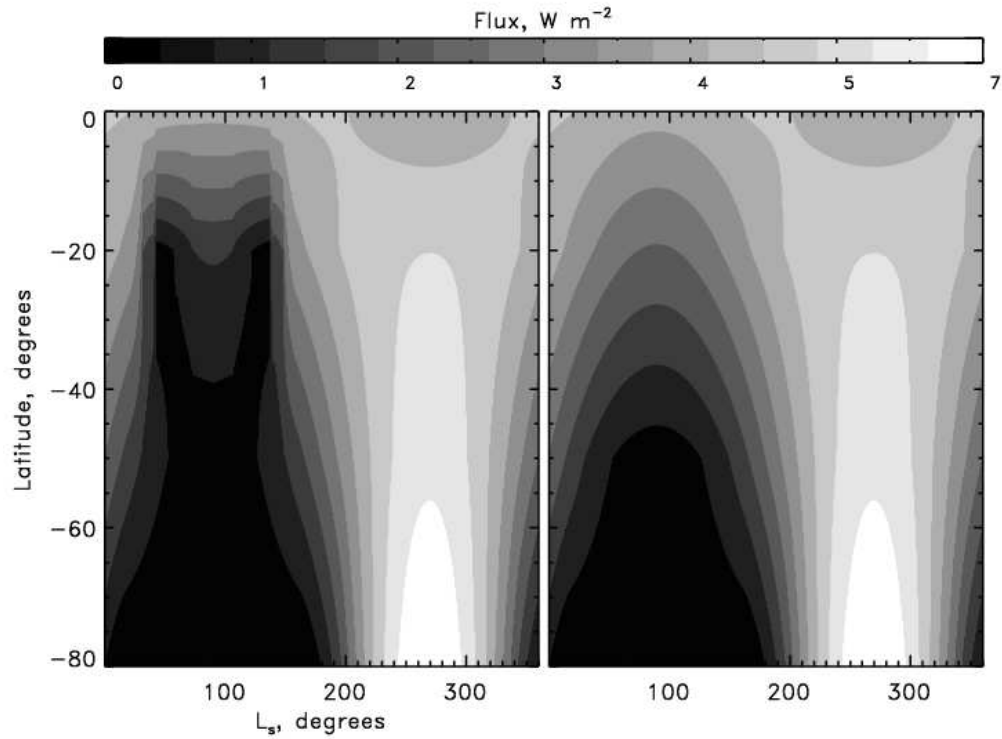
Figure 2.4: Daily mean insolation at the top of the atmosphere in W m^{-2} ($F(TOA)$) as a function of latitude and season (L_s). The effects of ring shadowing is seen on the left and without ring shadowing on the right. Minimum insolation is received during the southern winter ($L_s = 90°$) at the pole and maximum insolation is received during southern summer ($L_s = 270°$) at the pole. The $F(TOA)$ for these plots is determined for 0°, -20°, -50°, and -80°.

Nicholson et al. (2000) confirmed that the ring particles are centimeter-to-meter in size, based on occultation measurement of 28 Sgr. The ring optical depths have negligible wavelength dependence in the ultraviolet, visible, and near infrared.

40

2.6 Time-Dependent Radiative Seasonal Model

The TMV model atmosphere extends from 1.02×10^{-4} to 660 mbar, the latter being the radiative-convective boundary (Bézard and Gautier 1985). The model is divided into a plane parallel atmosphere consisting of 69 evenly spaced, logarithmic pressure layers (dp) and bounded by 70 levels (p). Temperatures and column density of the atmosphere are defined at the pressure levels and interpolated in $\log(p)$ space for layer values. Optical depths are determined at layers and radiative transfer calculations are a function of pressure layer. Local thermodynamic equilibrium (L.T.E.) is assumed throughout.

The model is neatly divided into two components: (1) emission of thermal radiation (0 to 1600 cm^{-1}) and (2) absorption of solar radiation (2000 to 10^5 cm^{-1}). The region 1600 to 2000 cm^{-1} lacks stratospheric emitters and contributes insignificantly to the heating and will be ignored, conserving computation time. From our model, C_2H_2 and C_2H_6 dominate in cooling (see Fig. 2.5) and CH_4 dominates in absorption at near infrared and visible wavelengths (Fig. 2.6). At ultraviolet wavelengths, CH_4, C_2H_2, C_2H_6, and C_2H_4 contribute to the absorption of solar radiation.

For the net thermal flux divergence in Fig. 2.5, C_2H_2 (dashed) and CH_4 (dash-dot) are dominant at 10^{-4} mbar to 10^{-3} mbar. However, C_2H_2 and C_2H_6 become the dominant emitters in the mid- to low-stratosphere. The considerable amount of cooling at the top of the stratosphere due to CH_4 coincides with a decrease in CH_4 opacity at this level. CH_4 plays a minor role in mid-stratospheric thermal emission. Methane lines are saturated due to its
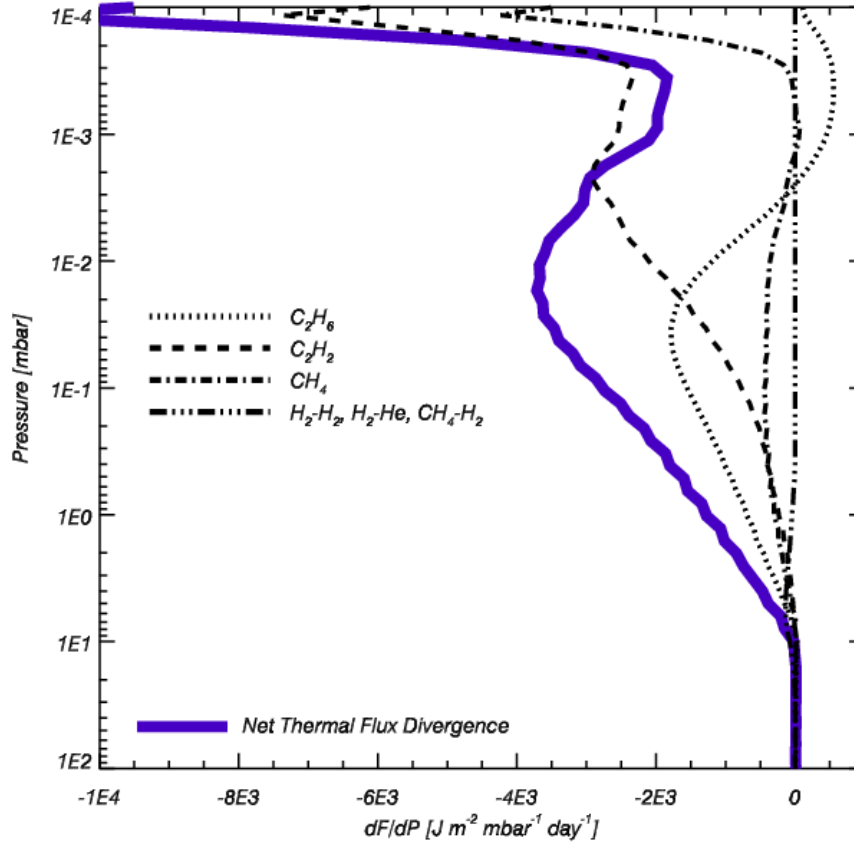
Figure 2.5: The net thermal flux divergence (cooling) (dF/dP) as a function of stratospheric pressure at $L_s = 0°$ and latitude of -72° at seasonal equilibrium.

large atmospheric abundance, therefore reducing its cooling efficiency (Yelle et al. 2001). The ν_4 band of CH_4 lies on the Wein tail of Saturn's thermal blackbody and cooling is weak. At high stratospheric pressure, photons within the ν_4 band may escape but at pressures greater than 1×10^{-4} mbar (Fig. 2.5), the significant overlying abundance of CH_4 traps the outgoing photons, allow-

ing for little contribution to the stratospheric net cooling. Despite the fact that C_2H_2 and C_2H_6 share similar band strengths and spectral coverage, C_2H_2 becomes optically thick higher in the stratosphere than C_2H_6 and contributes less to stratospheric cooling. C_2H_2 has a much simpler structure than C_2H_6, such that the majority of line emission is confined to several strong lines. C_2H_2 lines become optically thick at a lower pressure than C_2H_6. The C_2H_6 band possesses many emission lines over a larger range of wavenumbers. Ethane presents some heating in the upper stratosphere, between 2×10^{-3} mbar and 10^{-4} mbar. Cooling due to H_2-H_2, H_2-He, and CH_4-H_2 (dash-triple-dot) is dominant near 5 mbar and greater due to p^2-dependence of pressure-induced opacity.

The net solar absorption rates in Fig. 2.6 are calculated for the near-IR using a combination of the HITRAN04 line data (2000 - 4790 cm^{-1}) and the Irwin et al. (2006) k-coefficients (4790 - 9500 cm^{-1}). Absorption of solar radiation at ultraviolet wavelengths peaks in the upper stratosphere. The five near-IR bands of CH_4 dominate in solar absorption. Visible wavelength absorption peaks near 10 mbar.

The model is run for a single user-defined latitude. Wavelength dependent optical depths are calculated using the sources detailed in Table 2.3. The flux divergence within a stratospheric layer, dF/dp, is determined from the difference between the flux entering a layer and the flux leaving the layer, including both thermal and solar radiation. Both a diurnal averaging method (Bézard 1986) and a diurnal integration method (this paper) were individually
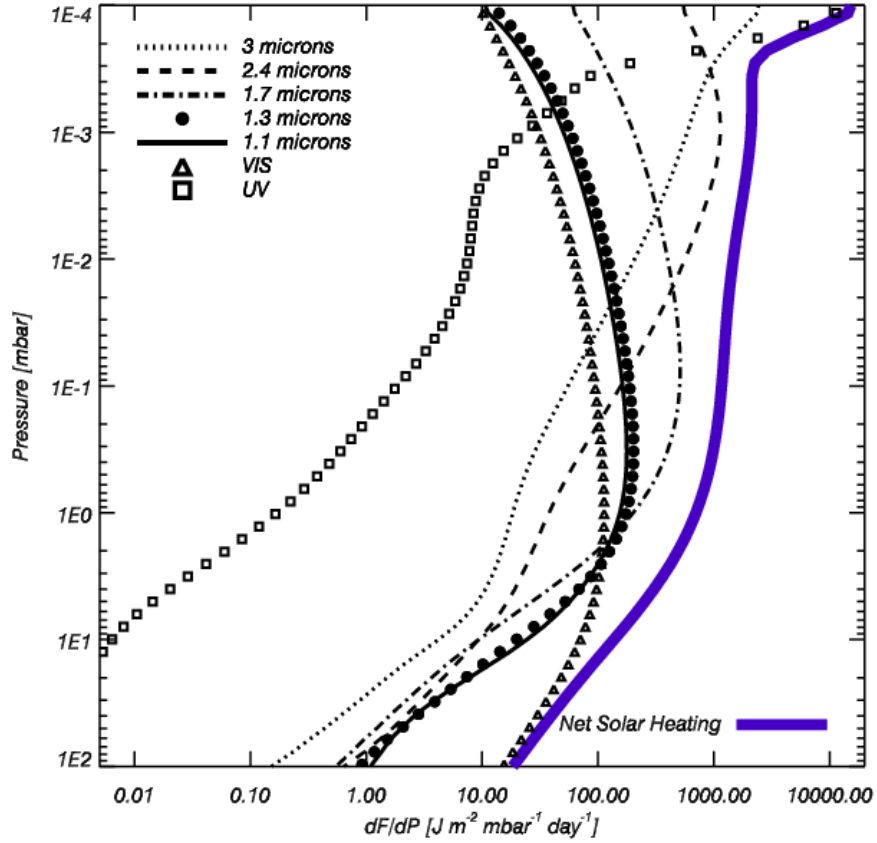
Figure 2.6: The heating rates (dF/dP) as a function of stratospheric pressure at $L_s = 0°$ and latitude of -72° for the (A) HITRAN04 (2000 - 4790 cm^{-1}) + Irwin et al. (2006) (4790 - 9500 cm^{-1}) near-IR parameterization.

incorporated in order to determine the optimal diurnal insolation procedure. The net absorption and emission is integrated over a time step corresponding to a minimum of 1 Saturn day (1/24148 of a Saturn year). This, in turn, determines the net change in temperature based on the Eq. 2.2 below. Subsequent time steps in L_s are updated with the thermal changes. The model

converges to seasonal equilibrium after $\sim$ 2 Saturn years for -72° latitude at 11 mbar and after $\sim$1.5 Saturn years for -72° latitude at 0.01 mbar.

The solar spectrum at Saturn was derived from SOLAR2000 v2.25 (Tobiska, et al. 2000, updated) for a single day (January 1, 2005). Figure 2.7 depicts the solar spectrum at Saturn for an average Sun-Saturn distance of 9.5 AU. Notably, insignificant solar flux exists in the mid- to far-infrared spectrum.
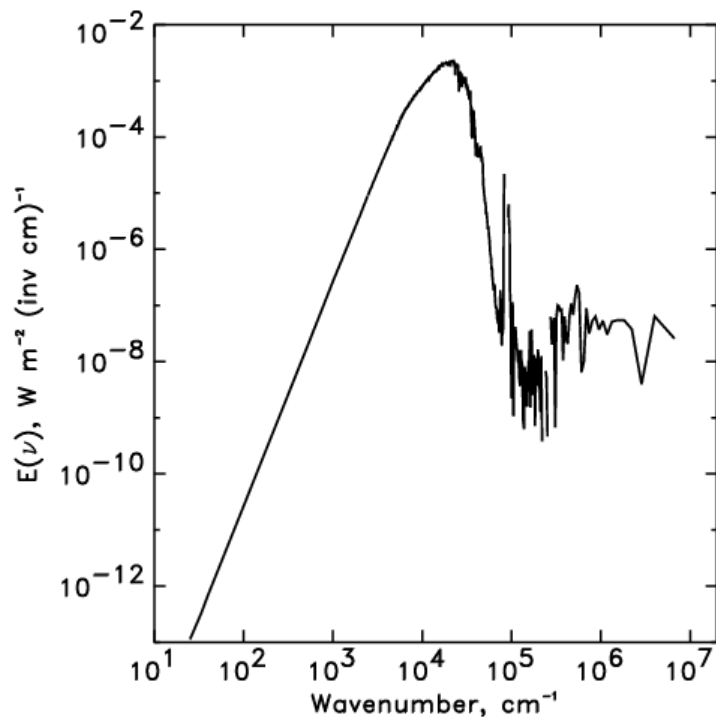
Figure 2.7: The Solar spectrum at Saturn, for an average distance of 9.5 AU, derived from SOLAR2000 v2.25 (Tobiska, et al. 2000)

45

Emission and Absorption Spectral Divisions

	ν (cm^{-1})	R ($\nu/\Delta\nu$)	Bin (cm^{-1})	Source
Emission				
far infrared	0 - 599		1	Borysow et al. (1988)
mid-infrared	600 - 1600	2.8×10^6		GEISA03
				(Jacquinet-Husson et al. 1999)
				Borysow et al. (1988)
Absorption				
near infrared	2000 - 9500:			
(A) line data +	2000 - 4790	1.52×10^6		HITRAN04
k-coeff	4790 - 9500		5	Irwin et al. (2006)
(B) line data	2000 - 4790	1.52×10^6		HITRAN04
	4790 - 9500	1.52×10^6		GEISA03
visible (a)	9523 - 1.0×10^4		3.63	Karkoschka (1994)
visible (b)	1.0×10^4 - 1.9×10^4		1	Karkoschka (1998)
visible (c)	1.9×10^4 - 3.3×10^4		3.63	Karkoschka (1994)
ultraviolet	4.0×10^4 - 10.0×10^4	50		Gladstone et al. (1996)
				Moses et al. (2000)
				references therein

Table 2.3: The resolving power or spectral bin sizes are given for each wavenumber component used in the TMV model. The thermal emission (or net cooling) component of the model atmosphere encompasses the far-IR and mid-IR. The solar absorption component (or net heating) encompasses the near-IR, visible, and ultraviolet regimes. Line data resolving powers (for HITRAN and GEISA data) were determined from Nyquist sampling the Doppler width of spectral lines. Resolving power and bin sizes for other regimes were limited by the sources of input data.

For a radiatively driven atmosphere, the rate of change of temperature as a function of the flux divergence within a pressure layer from Bézard and Gautier (1985) is given by

$$\frac{dT}{dt} = \frac{M_w g}{C_p} \frac{dF}{dp}. \tag{2.2}$$

We have adopted a mean molecular weight $M_w = 0.002226$ kg mol^{-1}, g is the acceleration due to gravity as a function of latitude, and the specific heat of the stratosphere at constant pressure is $C_p = 24.43$ J mole^{-1} K^{-1}. All these parameters are assumed to be constant with altitude. Our value for C_p is based on the formalism of Wallace (1980). The $[C_p/R]_{H_2}$ value at 140 K for H_2 is assumed to be the "normal" Wallace (1980) value of 3.0. Adopting the "intermediate" $[C_p/R]_{H_2}$ of 3.1 from Wallace (1980) does not alter seasonal temperatures. The hydrogen and helium mole fractions are assumed to be $q_{H_2} = 0.877$ and $q_{He} = 0.118$, based on re-analysis of Voyager data (Conrath and Gautier 2000).

From Eq. 2.2, the dT/dt of a layer is interpolated in $\log(p)$ space for pressure levels and added to the initial temperature profile, $T(t) = T(t - 1) + (dT/dt)(dt_{step})$. The new, concluding temperature profile is the starting profile for the subsequent time step. Model-derived seasonally dependent temperature-pressure profiles are overplotted in Fig. 2.8. The pressure at which the stratospheric inversion occurs is dependent upon season and is highest in the stratosphere near summer solstice ($L_s = 270°$). Likewise, the location of the mesopause is also dependent upon season, but is located at the

47
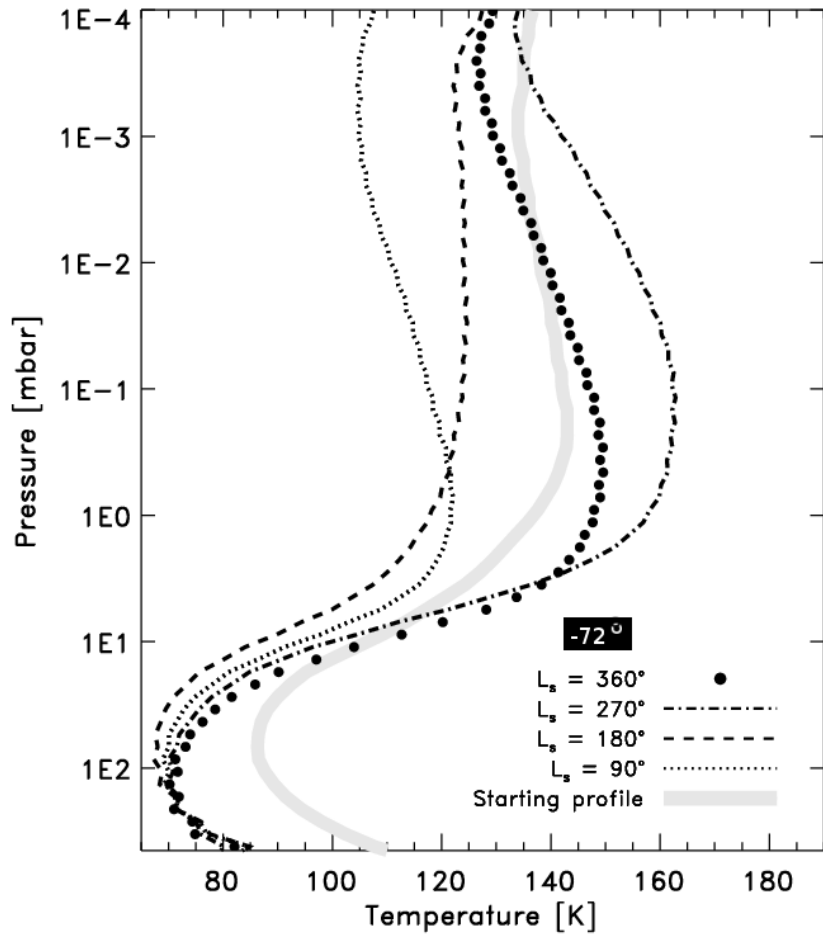
Figure 2.8: Predicted seasonal equilibrium temperature versus pressure profiles for a latitude of $-72°$ at southern autumnal equinox (360°), southern winter solstice (90°), southern vernal equinox (180°), and southern summer solstice (270°). The starting model profile is indicated in thick gray. The black profiles indicate model (A)1. HITRAN04 + Irwin et al. (2006) near-IR parameterization results.

lowest pressure near southern winter due to the absence of solar forcing at the top of the stratosphere. This becomes increasingly obvious over the full Saturnian year. Temperatures for stratospheric pressures 50 mbar to 1 mbar are largely determined by seasonal changes in insolation. For pressures less than 1 mbar, temperatures are determined by both insolation and stratospheric chemistry (Fig. 2.2).

Adaptive time steps have been implemented for computational efficiency. The model is initiated with a time step of 1 Saturn day and the calculation of dT/dt is performed for this initial time step. If the resultant $|dT/dt| < 0.8$ K (time step)$^{-1}$ at all levels, the time step is doubled for all layers and dT doubles sequentially. The doubled time step becomes the subsequent starting step. If $|dT/dt| > 0.8$ K (time step)$^{-1}$ for a single layer, the time step is not changed. Once $|dT/dt| > 2$ K (time step)$^{-1}$ for a single layer, both the time step and the dT are halved for all layers. This procedure expedites the seasonal calculations.

The ephemeris information, taken from the Jet Propulsion Laboratory's Horizons ephemeris calculator (Giorgini et al. 1996), is updated with each time step for $L_s = 0°$ to $360°$. Ephemeris data for a single Saturn year is utilized for all subsequent years. The calculations begin at $L_s = 0°$ at September 1950 and go to June 1980.

For our model, the CH_4 stratospheric mole fraction is held at 4.5 x 10^{-3} (Flasar et al. 2005) at the base, and is allowed to decline with decreasing pressure due to the combination of eddy and molecular diffusion. Implementing the

[CH$_4$]/[H$_2$] Flasar et al. (2005) abundance at the lower limit of its uncertainty results in a constant -4 K for our model-derived temperatures.

2.6.1   The Cooling Component: 0 to 1600 cm^{-1}

For the mid-infrared (mid-IR) (600 to 1600 cm^{-1}), optical depths were pre-tabulated at 10 K intervals between -50 K and $+60$ K from the starting temperature profile (Fig. 2.8) using a line-by-line method at a latitude of -40°. GEISA03 (Gestion et Etude des Informations Spectroscopiques Atmosphériques) line parameters were implemented for the ro-vibrational transitions of ^{12}CH$_4$, ^{13}CH$_4$, ^{12}C^{13}CH$_2$, ^{12}C$_2$H$_2$, ^{12}C^{13}CH$_6$, and ^{12}C$_2$H$_6$ (Jacquinet-Husson et al. 1999). Collisionally induced H$_2$-H$_2$, H$_2$-He and CH$_4$-H$_2$ continuum opacity was accounted for following the Borysow et al. (1988) formalism. Collisionally induced H$_2$-H$_2$, H$_2$-He, and CH$_4$-H$_2$ opacities are the sole opacity sources considered in the far-infrared (far-IR) (0 to 599 cm^{-1}). Molecular species such as NH$_3$ and PH$_3$ have insignificant stratospheric abundances and are not expected to contribute significantly to atmospheric cooling above the NH$_3$ condensation region in the troposphere. Negligible solar flux exists in this spectral range (see Figure 2.7). Figure 2.9 depicts where $\tau = 1$ in the model stratosphere for the cooling component. C$_2$H$_2$ and C$_2$H$_6$ dominate in emission in the mid-stratosphere. The ν_4 band of CH$_4$ slightly overlaps Saturn's thermal blackbody near 1500 cm^{-1} and therefore this band can emit minimally, coinciding with the CH$_4$ cooling peak at 1×10^4 mbar in Fig. 2.5.

Partition sums, $Q(T_o)$, for each molecule and isotopic species were de-
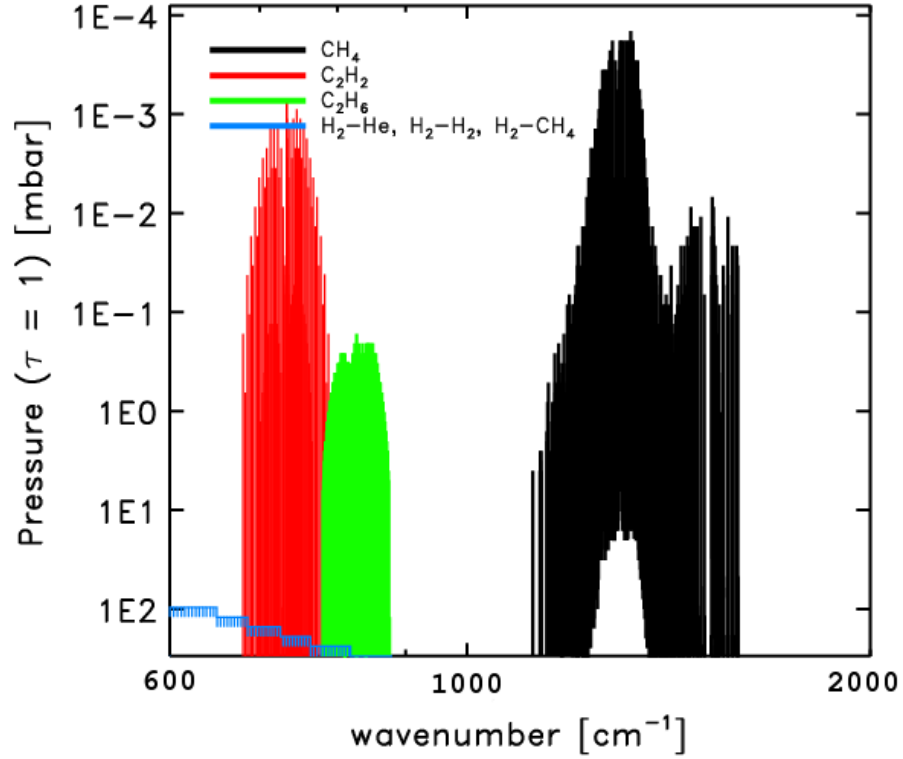
Figure 2.9: The stratospheric pressure for which $\tau = 1$ as a function of wavenumber for the thermal emission component of the model (0 - 1600 cm^{-1}) (far-infrared and mid-infrared) for a latitude of -80° at vernal equinox. All cooling calculations utilized GEISA03 line data for C$_2$H$_2$, C$_2$H$_6$, and CH$_4$. Not shown is the spectral region 0 -600 cm^{-1} which contains solely the contribution of collisionally induced continuum and is optically thin.

rived using the GEISA03 line-parameters at $T_o = 296$ K and for temperatures defined by our temperature profile, $Q(T)$. The total internal partition sum of

a molecule at a specific temperature is the sum over all states s:

$$Q(elec, vib, rot, ...) = d_i \sum_s d_s e^{-E_s/kT}. \tag{2.3}$$

Here, d_i is the state-independent degeneracy factor and d_s is the state-dependent degeneracy factor. E_s is the energy of a given state. The ratio of $Q(T_o)$ and $Q(T)$ provides a correction factor to derive new line-strengths, $S_l(\nu)$, for temperatures defined by our temperature profile. Corrected for stimulated emission, the equation of line-strength becomes,

$$S_l(T) = S_l(T_o) e^{\frac{-E_s}{k}\left(\frac{1}{T_o}-\frac{1}{T}\right)} \left(\frac{1 - e^{-1/kT}}{1 - e^{-1/kT_o}}\right) \frac{Q(T_o)}{Q(T)}. \tag{2.4}$$

The lines were broadened by a Voigt profile, $\phi(\nu)$, dependent on pressure and temperature. Subsequently, optical depths were derived from the column abundance, $U(p, T, g)$, mixing ratio, $q(p, g)$, and the broadened line-strengths,

$$\tau(\nu, p, T, g) = \phi(\nu) S_l(T) U(p, T, g) q(p, g). \tag{2.5}$$

The seasonal model can be run for any user-defined latitude, updated temperature profiles, and altered mixing ratios. As a result, optical depths required for these updated parameters are interpolated from the initial line-by-line optical depth grid within the seasonal model. In this multi-step process, a "pseudo-energy" E_p is calculated from the ratios of bracketing optical depths, for τ between $\tau(\nu, p, T_1)$ and $\tau(\nu, p, T_2)$ in the a-priori grid,

$$\frac{\tau_1}{\tau_2} = e^{\frac{hc}{k}\left(\frac{1}{T_2}-\frac{1}{T_1}\right)E_p}. \tag{2.6}$$

This "pseudo-energy" bootstraps the new optical depth to existing values of bracketing optical depths, as a function of gravity, mixing ratio, and column density for the latitude of interest,

$$\tau(\nu, p, T, g) = \frac{U(p, T, g)q(p)}{U_o(p, T, g_o)q_o(p)}\tau_1 e^{\frac{hcE_p}{k}\left(\frac{1}{T_1(p)} - \frac{1}{T(p)}\right)}. \tag{2.7}$$

The nominal optical depth grid parameters are characterized by gravity g_o, mixing ratio q_o, and column density $U_o(p, T, g_o)$.

Following the formalism of Goukenleuque et al. (2000), the frequency-dependent net thermal flux, F_{IR} (Eq. 2.8), as a function of optical depth is the sum of the outgoing flux, the incoming flux, and flux from below the boundary level of the model atmosphere:

$$
\begin{aligned}
F_{IR}(\tau_\nu, p) = \ & 2\pi \int_{\tau_\nu}^{\tau_\nu^b} B_\nu[T(\tau_\nu^{'})]E_2(\tau_\nu^{'} - \tau_\nu)d\tau_\nu^{'} \\
& - 2\pi \int_0^{\tau_\nu} B_\nu[T(\tau_\nu^{'})]E_2(\tau_\nu - \tau_\nu^{'})d\tau_\nu^{'} \\
& + 2\pi \ B_\nu(T_b)E_3(\tau_\nu^b - \tau_\nu).
\end{aligned}
\tag{2.8}
$$

In Equation 2.8, τ_ν is the optical depth at wavenumber ν, $B(\nu)$ is the Planck function. The exponential function, E_n, is the nth exponential function,

$$E_n(\tau_\nu) = \int_1^\infty (exp(-\tau_\nu t)/t^n)dt, \tag{2.9}$$

where t is the airmass, $\sec z$. The optical depth, τ_ν, is the sum of the continuum and hydrocarbon opacities. $T(\tau_\nu)$ is the temperature of the level of optical depth τ_ν. T_b is the effective temperature of the bottom boundary, corresponding to the radiative convective boundary of our bottom atmospheric

level, $p = 660$ mbar. The net flux at the bottom boundary is the calculated downward flux of the bottom level and the upward 4.7 W m^{-2} at the radiative-convective boundary, from Voyager data (Bèzard et al. 1985). Changing the value of the 4.7 W m^{-2} has no observable effect on the stratospheric thermal structure, consistent with the findings of Bézard and Gautier (1985).

The net thermal flux as a function of optical depth τ is indexed from the bottom pressure layer $(i = n)$ to the top of the atmosphere $(i = 1)$ and is quantitatively expressed as

$$F_{IR}(\tau) = \sum_{i=1}^{n-1} F_i(\tau) + F_o(\tau), \tag{2.10}$$

where $F_i(\tau)$ is the flux contribution of atmospheric layer i, bounded by pressure levels p_i and p_{i+1}, and $F_o(\tau)$ is the outgoing contribution from below the bottom boundary. The Planck function within layer i is assumed to vary linearly as a function of optical depth: $B(\tau) = a_{i+1} + (a_i - a_{i+1})[(\tau - \tau_{i+1})/(\tau_i - \tau_{i+1})]$, with a_i as the Planck function value at level i and τ_i the optical depth of level i. Integrating Equation 2.8 by parts, the expression for the contribution of layer i to the net flux at the level corresponding to an optical depth τ becomes

$$\begin{aligned} F_i(\tau) = \quad & 2\pi \quad [a_{i+1} E_3(|\tau - \tau_{i+1}|) - a_i E_3(|\tau - \tau_i|)] \\ + \quad & 2\pi \quad \frac{(a_i - a_{i+1})}{|\tau_i - \tau_{i+1}|} |E_4(|\tau - \tau_i|) - E_4(|\tau - \tau_{i+1}|)|, \end{aligned} \tag{2.11}$$

and the expression for outgoing flux from below the bottom boundary is

$$F_o(\tau) = 2\pi E_3(\tau_b - \tau) B(T_b). \tag{2.12}$$

54

For a given temperature profile, $F_{IR}(\tau)$ is calculated and then integrated over wavenumber in order to produce the net flux.

2.6.1.1 Mid-IR Resolution and Binning

The presence of numerous and narrow (~ 1 km s^{-1} line widths) spectral lines due to molecular transitions in planetary stratospheres require fine spectral sampling in order to calculate the flux in spectral lines. Without opacity binning, one radiative transfer calculation is performed per spectral interval, where the spectral intervals are determined by the resolving power required to Nyquist sample the Doppler width of spectral lines. Large portions of the thermal spectrum have a minimal number of transitions and rather constant changes in continuum features, allowing for a coarser sampling. A fine resolution grid significantly extends the computational time required to perform radiative transfer calculations. For a resolving power fine enough to Nyquist sample ethane at 140 K, an R of 2.8×10^6 was adopted requiring 67 minutes to complete a single time step (Table 2.4) (3.0 GHz Pentium 4 processors with 1.0 GB of RAM).[1] Up to 600 time steps may be required for the model to converge to seasonal equilibrium, resulting in a 28-day model run for a single latitude. Developing an adaptive, spectral binning routine for the mid-IR is then critical for computational productivity and efficiency.

The resolving power Ω required to Nyquist sample the full width at half maximum of the mid-IR CH$_4$ spectra was determined to be 1.6×10^6 at

---

[1]An $R = 2.2 \times 10^6$ would have likely been sufficient

Maximum Percent Error in Mid-Infrared Binning Routine

Threshold ($\Delta\tau$)	Run Time (min)	% Error dT/dt (10^{-4} mbar)	% Error dT/dt (1 mbar)
0.1	14	4.297	32.497
0.01	18	0.154	14.844
0.001	25	0.071	3.41
1×10^{-4}	31	0.025	0.054
none	67	0.00	-

Table 2.4: The maximum percent errors in calculating $\langle dF/dp_{IR}\rangle$ for a variety of bin thresholds are calculated for $L_s = 0$. The calculations were performed for one adaptive time step which coincides with two Saturn days at this L_s. Nominally, all model calculations are performed for a $\Delta\tau = 0.001$. The maximum errors in $\langle dF/dp\rangle$ for differing bin sizes occurs at the 0.1-mbar level and the 10^{-4}-level, which coincides with the peaks in the C_2H_6 and C_2H_2 contribution.

140 K, based on the Doppler width (α_D) of the spectral line at $\nu = 1300 \text{ cm}^{-1}$. The Doppler width is

$$\alpha_D = \sqrt{\frac{2RT}{M_w}} \frac{\nu}{c}. \tag{2.13}$$

Here, the gas constant is R, the speed of light is c, M_w is the molecular weight of methane (16×10^{-3} kg/mol), and ν is 1300 cm^{-1}. The resolving power (Ω) is then,

$$\Omega = \frac{2\nu}{\alpha_D} = 1.6 \times 10^6. \tag{2.14}$$

C_2H_6 and C_2H_2 require resolving powers of 2.2×10^6 and 2.0×10^6 at 140 K, 830 and 700 cm^{-1}, respectively. C_2H_2 and C_2H_6 are dominant in their contribution towards cooling the atmosphere between 1×10^{-4} mbar and 3 mbar (Fig. 2.5). This region of the stratosphere may be characterized by temperatures between 130 K and 150 K, dependent upon latitude and season. We adopted a resolving power of 2.8×10^6 for all model runs.

Full radiative transfer calculations were performed at spectrally sequential optical depths only if neighboring optical depths differed by more then a predetermined threshold value, $\Delta\tau$. This $\Delta\tau$ is analytically chosen for the 10-mbar level, since below this pressure level there is little thermal contribution to the stratosphere (Greathouse et al. 2005a). Spectrally sequential optical depths differing by less than $\Delta\tau$ are grouped together. The optical depth for the entire spectral bin, τ_{bin}, is equal to the central optical depth within the bin. A single radiative transfer calculation is performed for this full spectral bin. This ensures that the radiative transfer calculations are performed at high resolution when needed and not unnecessarily.

Table 2.4 illustrates the error introduced in the calculation of the cooling rate based on implementation of the binning technique for one full time step at seasonal equilibrium temperatures. The $\Delta\tau$ values tested are 1×10^{-4}, 1×10^{-3}, 1×10^{-2}, and 0.1 for an $\Omega = 1.4\times10^6$. All model runs presented in this paper adhere to a $\Delta\tau$ of 0.001. This threshold has a 0.07% error at 10^{-4} mbar in dT/dt and a 3.41% error at 1 mbar relative to an identical model run without binning. This corresponds to an error in temperature of 7×10^{-4} and 0.034 K, respectively. The computational time for the model run with $\Delta\tau = 0.001$ is 25 minutes (3.0 GHz Pentium 4 processors with 1.0 GB of RAM). Without binning, the same time step requires 67 minutes to complete. Computational time increases with decreasing $\Delta\tau$ value and percent error decreases.

2.6.2 The Heating Component: 2000 to 10^5 cm^{-1}

As the wavelength of incident light becomes shorter, absorption of solar flux becomes increasingly important and peaks between 2×10^4 and 2.5×10^4 cm^{-1} (5000 to 4000 Å). Figure 2.7 shows the incident solar flux at Saturn for our model at a Saturn-Sun distance of 9.5 AU. Notably, little solar flux is received at the planet outside of 2000 to 1×10^5 cm^{-1}. Solar flux parameters were taken from SOLAR2000 v2.25 (Tobiska, et al. 2000).

Peak solar forcing occurs at $L_s = 270°$ for the south pole (coincidentally near perihelion, which occurs at $L_s = 278°$), consistent with southern summer solstice. Conversely, at an $L_s = 90°$, insolation decreases from equator to the south pole. Ring shadowing effects are pronounced between 10° and 40°

latitude (Moses and Greathouse 2005), shielding portions of these latitudes during the winter season. Effects are minimal near the equator and poles.

The dominant opacity in the near-IR (2000 to 9500 cm^{-1}) and visible (9523 to 3.3×10^4 cm^{-1}) is due to CH_4. At ultraviolet wavelengths (4.0×10^4 to 10×10^4 cm^{-1}), CH_4, C_2H_2, C_2H_6, and C_2H_4 are included in optical depth calculations. Optical depths were calculated using a combination of Irwin et al. (2006) CH_4 k-coefficients, HITRAN04 (Rothman et al. 2005), and GEISA03 (Jacquinet Husson et al. 1999) CH_4 line parameters for the near-IR, Karkoschka (1998) and Karkoschka (1994) visible absorption coefficients, and Moses et al. (2000) and Gladstone et al. (1996) ultraviolet molecular photoabsorption cross sections. Figure 2.6 details the heating rates calculated in the model from 2000 to 10^5 cm^{-1} for the (A) HITRAN04 + Irwin et al. (2006) near-IR parameterization. Figure 2.10 details the differences in the heating between (A) and (B) HITRAN04 + GEISA03 parameterizations for near-IR bands between 4790 - 9500 cm^{-1}. Since the near-IR dominates in solar absorption in the mid-stratosphere (Fig. 2.11), but line data remains qualitative for many shortwave transitions, the choice of absorption parameterization is important and is discussed in the following subsection.
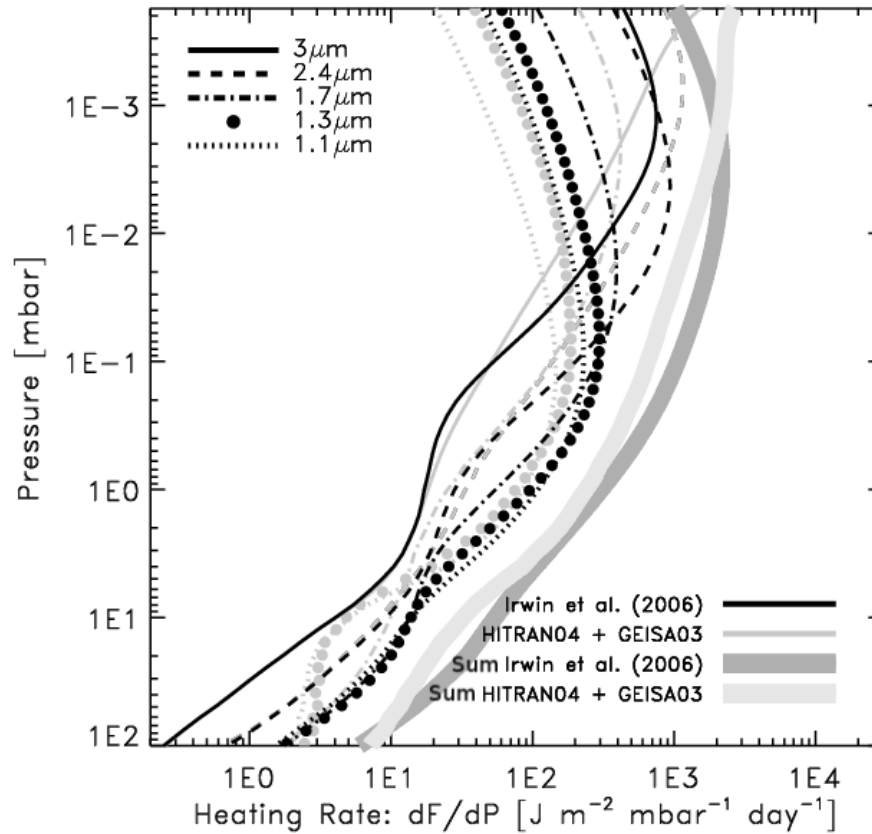
Figure 2.10: Heating rates derived with the Irwin et al. (2006) k-coefficients (black) for the 3μm (3333 cm^{-1}), 2.3μm (4348 cm^{-1}), 1.7μm (5882 cm^{-1}), 1.3μm (7692 cm^{-1}), and 1.1μm (9091 cm^{-1}) bands for the south pole. The net result is plotted in thick, dark gray. Overplotted are the heating rates derived with the HITRAN04 (2000 - 4790 cm^{-1}) + GEISA03 (4790 - 9500 cm^{-1}) near-IR parameterization (thin gray) for the same bands. The net result is plotted in thick, light gray.
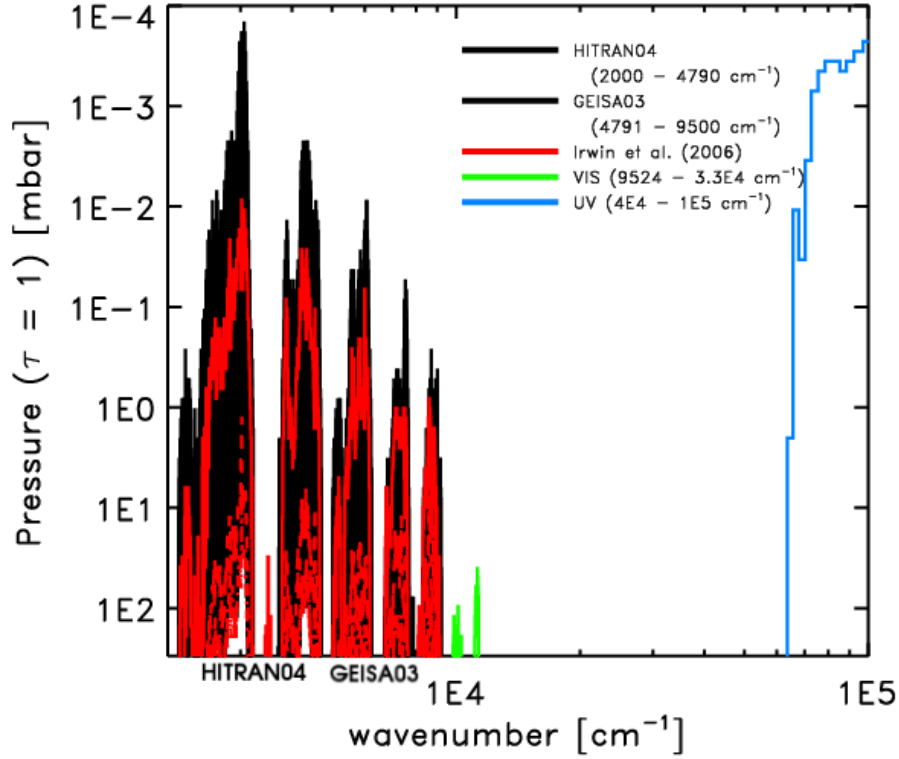
Figure 2.11: The stratospheric pressure for which $\tau = 1$ as a function of wavenumber for the heating component of the model (2000 - 10^5 cm^{-1}) including the near-IR, visible, and ultraviolet regimes near the south pole (-72°) at vernal equinox. Use of the HITRAN04 (2000 - 4790 cm^{-1}) and GEISA03 (4790 - 9500 cm^{-1}) line data are shown in black for the near-IR regime. Separate use of the Irwin et al. (2006) CH$_4$ absorption coefficients are overplotted in red. The differing red line styles indicate where $\tau = 1$ for three Irwin et al. (2006) absorption coefficients: k_1 (dash-dot), k_6 (dash), and $k_1 0$ (solid). Use of these coefficients is detailed in Section 2.6.2.2. A zoomed-in portion of the spectrum is show in Fig. 2.12.

An aerosol opacity source was included for some TMV model tests

61
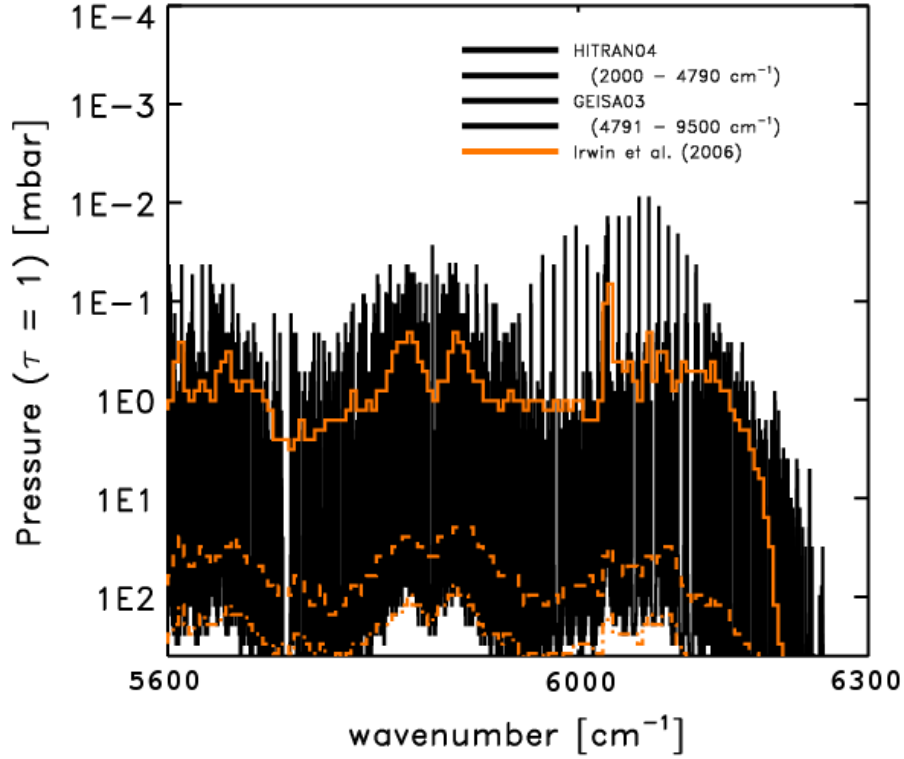
Figure 2.12: A zoomed in plot depicting the $\tau = 1$ as a function of pressure for the 1.7 μm near-IR band of CH_4. The results from using the Irwin et al. (2006) CH_4 absorption coefficients (orange) are juxtaposed with the GEISA03 line-by-line calculation. The differing line styles in orange indicate three $\tau = 1$ values for three k-coefficients. The use of k-coefficients are detailed in Section 2.6.2.2.

between the wavenumbers 2000 - 10^5 cm^{-1}. Opacity information was generated for this model by Moses (this paper) based on information from Karkoschka and Tomasko (2005). Fig. 2.13 depicts the aerosol optical depth as a function of wavenumber for -80° (black) and 0° (gray) for several pressures.
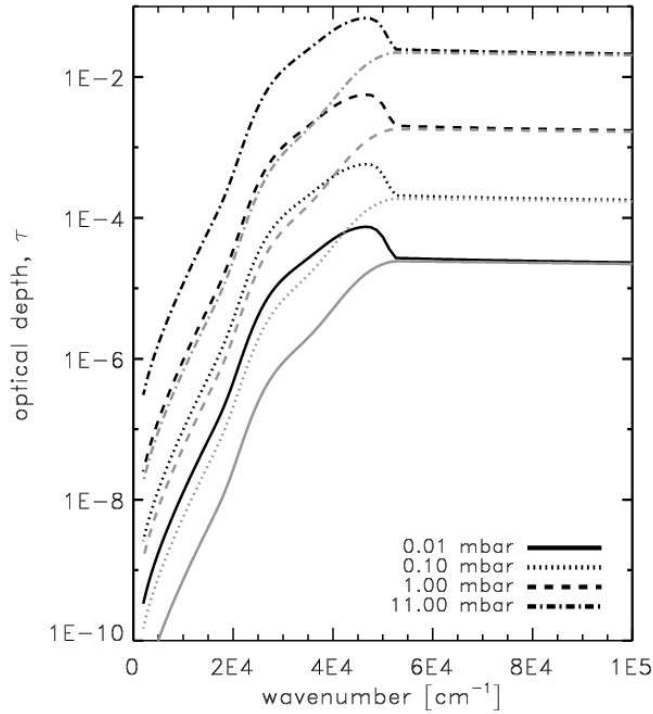
Figure 2.13: Aerosol optical depths from Moses (this paper) based on parameters from Karkoschka et al. (2005). These optical depths are for several different pressures as a function of wavenumber for the south pole (-80°) (black) and equator (gray)

2.6.2.1 Near-IR CH$_4$ Absorption

Despite the significance of methane in the atmospheres of the outer planets, CH$_4$ spectroscopy between 5000 and 10^4 cm^{-1} remains inadequate for high resolution remote sensing studies (Brown 2005). Substantial gaps exist in the line data available for near-IR CH$_4$. At shorter wavelengths, the near-IR CH$_4$ line-transitions become increasingly complicated (Irwin et al. 2006)

63

and laboratory determination of appropriate lower state energies for temperatures and pressures comparable to those found in outer planet atmospheres are challenging.

CH_4 line data in the GEISA03 database are limited to the empirical near-IR lines of Brown (2005), in which lower state energies were set to 555.555 cm^{-1} for lines between 3800-4600 cm^{-1} (2.3 μm band) and 5500-6185 cm^{-1} (1.7 μm band), and 333.333 cm^{-1} elsewhere (1.1 μm, 1.3 μm bands). This is believed to be a reasonable approximation for the energies (Irwin et al. 2006). The HITRAN04 database (Rothman et al. 2005) contains lower state energies for the 3 μm and the 2.3 μm bands, but equates the lower state energies for the 1.7, 1.3, and 1.1 μm bands to -1. Bézard and Gautier (1985) used an earlier version of the GEISA database near-IR line parameters (Chedin et al. 1982) for their stratospheric modeling, which contained even less knowledge of lower state energies in the near-IR. For the 5882.4 cm^{-1} (1.7 μm) group and shortward, data used by Bézard and Gautier (1985) was limited to the $2\nu_3$ transition, and the authors multiplied the heating rate determined for the $2\nu_3$ band by 3 to account for the two other shortwave near-IR groups. This provided the best near-IR parameterization at the time.

The Irwin et al. (2006) near-IR CH_4 absorption coefficients (2000 - 9500 cm^{-1}) currently provide the most complete CH_4 absorption parameters. Irwin et al. (2006) present k-distribution parameters fitted to the band models of Strong et al. (1993) and Sihra (1998) at temperatures and pressures that better sample giant atmosphere than those of Baines et al. (1993);

Sromovsky et al. (2006) for the near-IR. This data set also includes corrections to the Irwin et al. (2005) data set for weakly absorbing wavelengths which were found to be important in Titan and the ice giants. The Irwin et al. (2006) near-IR parameterization alone proved to model observed Uranus spectral features at $p > 2000$ mbar with higher fidelity (Sromovsky et al. 2006) than past band model fits (Strong et al. 1993; Irwin et al. 1996). It should be noted that the HITRAN04/GEISA03 data set is likely insufficient for giant-planet atmospheric modeling shortward of 4790 cm^{-1} (2.1 μm), but longward of 4790 cm^{-1}, the line data are likely more precise than the Irwin et al. (2006) near-IR k-coefficients.

Recent Tomasko et al. (2007) DISR Titan observations have shown that an overall decrease in the Irwin et al. (2006) CH$_4$ absorption coefficients for 1.7, 1.3. and 1.1 μm bands were required to fit observed spectra.

To best account for near-IR CH$_4$ absorption, we utilize line-by-line calculations using HITRAN04 line parameters for the wavenumber range 2000 - 4790 cm^{-1} (following the method discussed in Section 2.6.1 for the mid-IR, without binning). This makes optimal use of the CH$_4$ line data information offered by HITRAN04 out to its near-IR completeness limit. For the range 4790 - 9500 cm^{-1}, we individually test the Irwin et al. (2006) near-IR CH$_4$ absorption coefficients combined with and without the Tomasko et al. (2007) multiplicative corrections against the GEISA03 line data.

Thermal inconsistencies generated using the near-IR Irwin et al. (2006) coefficients may be attributed to the laboratory pathlengths ($\leq\sim$ 14 m) used

in derivation (Tomasko et al. 2007). Pathlengths in the giant planets are long, $\sim$ 20 to 50 km. Laboratory determination of the methane absorption within gas giant atmospheres is challenging due to low atmospheric pressures and cold temperatures and measurements may require multiple passes through long cells at high pressures in order to produce measurable methane absorption (Tomasko et al. 2007). As noted by Tomasko et al. (2007), in order to recreate the effective pathlengths in Titan's atmosphere, laboratory methane mixing ratios must be increased from 1.5% to 100%. This allows for the reduction of the pathlength from 50 km to 800 m (Tomasko et al. 2007). Extrapolation but be implemented to determine the amount of methane absorption within a giant-planet environment. The pathlengths and temperature-pressure profile for Saturn are similar to Titan's, suggesting that use of the Tomasko et al. (2007) corrections is appropriate.

The correlated k-distribution method has been implemented in radiative transfer calculations by various authors (Lacis and Oinas 1991; Goody et al. 1989,e.g.). This method sorts spectral transmittance based on a probability function of the gas absorption coefficients. A single calculation may then be performed once for a single absorption coefficient and statistically weighted based on its existence within a given spectral bin. The correlated k-distribution method has not been proven to maintain high accuracy for stratospheric calculations (Goody et al. 1989).

2.6.2.2 Use of Irwin et al. (2006) CH$_4$ k-coefficients

The Irwin et al. (2006) near-IR CH$_4$ absorption coefficients, k_n, were used to derive near-infrared optical depths as a function of temperature within seasonal model time steps. There are ten Irwin et al. (2006) k-coefficients per 5 cm^{-1} bin between the wavenumbers 4790 - 9500 cm^{-1}. The probability distribution of each k_n coefficient is given by Δg_n. The derivation of k-coefficients are detailed in Chapter 4. The wavelength-dependent optical depth through a layer in the atmosphere with pressure p and temperature T as a function of k_n is,

$$\tau_n(\nu, p, T, g) = k_n(\nu, p, T)q(p)U(p, T, g), \qquad (2.15)$$

where $U(p, T, g)$ is the column density at the user-defined latitude as a function of pressure, temperature, and gravity and $q(p)$ is the mixing ratio of CH$_4$ at pressure p (Fig. 2.2).

Within each of the Irwin et al. (2006) 5 cm^{-1} wavenumber bins (943), 10 separate radiative transfer calculations through the extent of the model atmosphere were performed as a function of k_n. The deposited flux at the top of the atmosphere is weighted by the values for Δg_n. The flux deposition as a function of k_n and layer is summed over the ten k_n values. This final flux is then used in determining the heating rates. This is illustrated in Fig. 2.14.

2.6.2.3 Diurnal Insolation

In order to determine the best method for calculating the daily insolation in the stratosphere as a function of season and latitude, we tested the
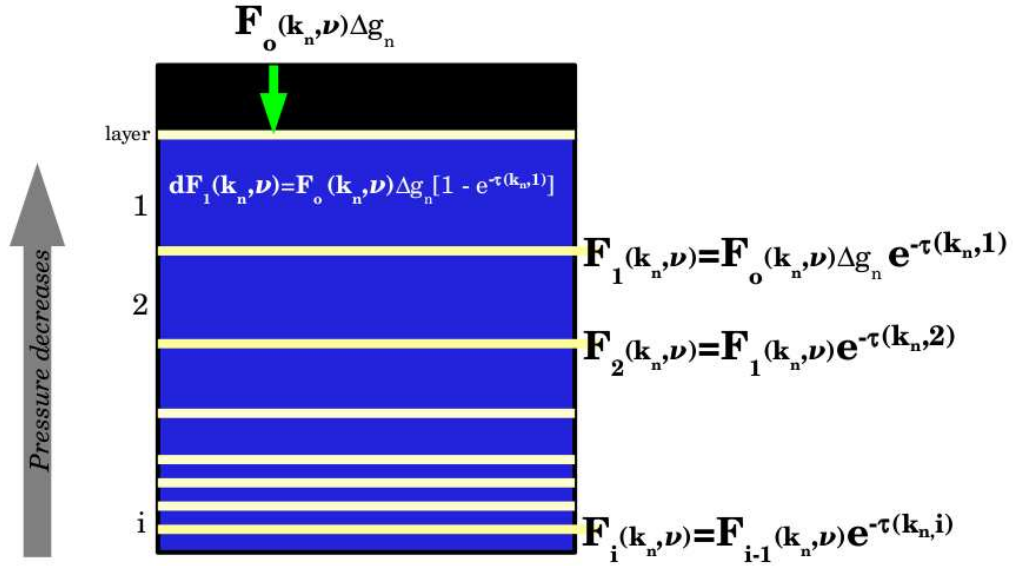
Figure 2.14: An illustration of the implementation of the Irwin et al. (2006) k-coefficients. The flux deposition at each layer in the stratosphere $(dF/dP(k_n,\nu))$ is calculated as a function of the ten k-coefficients, k_n, per Irwin et al. (2006) wavenumber bin (ν). This technique is applied to the near-IR region 4790 - 9500 cm^{-1}. The incident solar radiation, $F_o(k_n,\nu)$ is multiplied by the Irwin et al. (2006) weights, Δg_n, iterated over k_n. Once the $dF/dP(k_n,\nu)$ is determined, the total flux deposition for a given wavenumber bin is the $\sum_n dF/dP(\nu)$.

Bézard (1986) diurnal averaging method against an exact diurnal integration method. Each was individually implemented in the TMV model and seasonal temperatures were derived.

For our exact diurnal integration method, the total solar flux absorbed within a pressure layer during a day occurs between sunrise and sunset as a function of latitude and season. This period of daylight is symmetrically

divided into two time periods: dawn-to-noon and noon-to-dusk. The absorbed flux is calculated during the dawn-to-noon time period and doubled to account for the total flux absorbed for the full day.

Radiative transfer calculations are performed once per spectral bin and per incident solar zenith angle for the heating component (2000 - 10^5 cm^{-1}). Ten solar zenith angles were calculated based on the season due to their dependency on solar declination angle δ, latitude θ, and time of day. The cosine of the solar zenith angle z is given by

$$\cos z = \sin \theta \sin \delta + \cos \theta \cos \delta \cos \alpha, \tag{2.16}$$

where α is the hour angle of the sun and varies between dawn $(\alpha = \alpha_o)$ and noon $(\alpha = 0)$.

The cosine of the hour angle of the sun at sunrise $(\alpha = \alpha_o)$ in planeto-centric coordinates as a function of user-defined latitude and solar declination angle is

$$\cos \alpha_o = \left(\frac{R_e}{R_p}\right)^2 (-\tan \theta \tan \delta). \tag{2.17}$$

The equatorial and polar radii are $R_e = 60{,}268$ km and $R_p = 54{,}364$ km (Lindal et al. 1985). Hour angles equidistant in time between $\alpha = \alpha_o$ $(\alpha_o = \pi/2$ for sunrise at equinox) and $\alpha = 0$ (noon at equinox) are generated at a user-defined resolution. For $|\cos \alpha| \geq 1$ and $\theta \delta > 0$, perpetual day is in occurrence. For $|\cos \alpha| \geq 1$ and $\theta \delta \leq 0$, the planet observes perpetual night.

From the top of the atmosphere downward, the deposited flux within

a layer dp (between pressure levels $p-1$ and p) as a function of $d\tau$ is given by

$$dF(dp) = F_o e^{-\tau/\cos z} \cos z (1 - e^{-d\tau(dp)/\cos z}),$$ (2.18)

where $F(p-1)$ is the incident flux from the level above the current layer dp and τ is the total optical depth down to level $p-1$. Near the top of the atmosphere, with an incident solar flux of $F_o = F(p-1)$ and $\tau \ll 1$, the expression $(1 - e^{-d\tau(dp)/\cos z})$ becomes $d\tau/\cos z$. Equation 3.1 simplifies to

$$dF(dp) = F(p-1)d\tau.$$ (2.19)

The $\cos z$ is no longer important at small optical depths.

From Eq. 3.1, an array of $dF(dp)$ values are generated for $n = 10$ solar zenith angles (in degrees). The resulting function of deposited flux per cosine zenith angle is integrated using the trapezoidal rule, such that the average absorbed insolation over a full day is

$$\langle dF(dp) \rangle_{day} = \frac{\int_{\alpha_o}^0 dF(dp) d\alpha}{\Psi},$$ (2.20)

with Ψ equal to the number of seconds in a Saturn day.

Bézard (1986) implemented a daily average value for $\cos z$. The deposition of solar radiation is a function of optical depth within a layer. The average daily $\cos z$ value for any latitude is described as

$$\langle \cos z \rangle_{day} = \frac{1}{2\pi} \int_{\phi_s - \phi_e}^{\phi_s + \phi_e} \frac{\cos\theta \cos\delta \cos(\phi - \phi_s) + \left(\frac{R_e}{R_p}\right)^2 \sin\theta \sin\delta}{\sqrt{\cos^2\theta + \left(\frac{R_e}{R_p}\right)^4 \sin^2\theta}} d\phi, \quad (2.21)$$

where ϕ and θ are the longitude and latitude of a point on the planet. The solar zenith angle is z and the solar declination, δ, is a function of the planet's obliquity, where $-26.7 \leq \delta \leq 26.7$ for Saturn. The solar longitude is defined as $\phi_s = L_s$. The variable ϕ_e is defined such that

$$
\begin{aligned}
\phi_e &= 0, \text{ if } - \left(\frac{R_e}{R_p}\right)^2 \tan\theta \tan\delta \geq 1 \\
\phi_e &= \cos^{-1}\left[-\left(\frac{R_e}{R_p}\right)^2 \tan\theta \tan\delta\right], \\
&\quad \text{if } -1 < -\left(\frac{R_e}{R_p}\right)^2 \tan\theta \tan\delta < 1 \\
\phi_e &= \pi, \text{ if } - \left(\frac{R_e}{R_p}\right)^2 \tan\theta \tan\delta \leq -1.
\end{aligned}
\tag{2.22}
$$

The solution to Eq. 2.21 is

$$
\langle \cos z \rangle_{day} = \frac{\cos\theta \cos\delta \sin\phi_e + \left(\frac{R_e}{R_p}\right)^2 \phi_e \sin\theta \sin\delta}{\pi \sqrt{\cos^2\theta + \left(\frac{R_e}{R_p}\right)^4 \sin^2\theta}}.
\tag{2.23}
$$

The Bézard (1986) approximation for all layers is

$$
F(\tau) \sim F_o \langle \cos z \rangle e^{-\tau/\langle \cos z \rangle_{day}},
\tag{2.24}
$$

where $\langle \cos z \rangle$ is the average cosine of the zenith angle for daytime and night time and is equal to ϕ_e/π times $\langle \cos z \rangle_{day}$ (Eq. 2.23).

At the top of the atmosphere, Equation 2.24 is not an approximation since $F(\tau = 0) = F_o \langle \cos z \rangle$. With increasing depth in the stratosphere, the $\langle \cos z \rangle_{day}$ approximation could insufficiently account for changes in incident

71

angle. From Equation 2.24, the deposition of solar radiation as a function of optical depth and pressure level (dF/dP)

$$dF(dp) = F_o \langle \cos z \rangle e^{-\tau/\langle \cos z \rangle_{day}} \left(1 - e^{-d\tau(dp)/\langle \cos z \rangle_{day}} \right). \qquad (2.25)$$

Values for $dF(dp)$ (Eq. 2.25) are compared to our integrated value of $dF(dp)$ (Eq. 3.1) with respect to a set of atmospheric optical depth values (Eq. 3.1). The resulting comparison is shown in Figure 2.15.
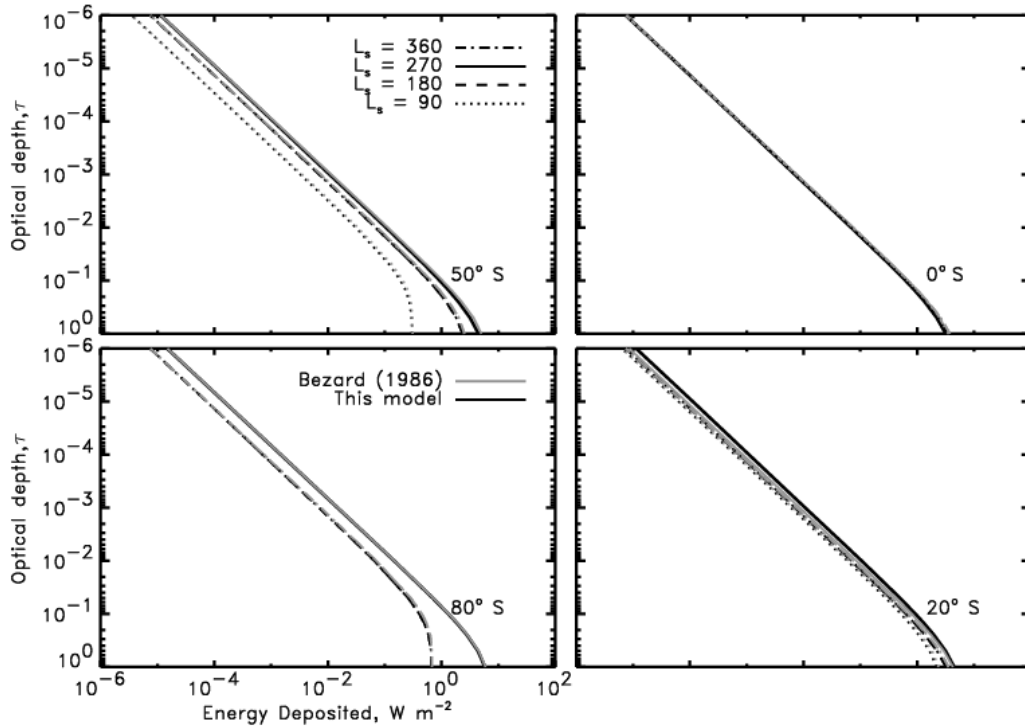
Figure 2.15: Flux deposition (W m^{-2}) as a function of optical depth, τ, and season (L$_s$) in the atmosphere for the diurnal averaging approximation of Bézard (1986) (gray) relative to the exact insolation integration method implemented in our model (black), for latitudes 0°, −20°, −50°, −80°. The seasons plotted are southern summer solstice (solid), winter solstice (dot), autumnal equinox (dash-dot), vernal equinox (dash); L$_s$ = 270°, 90°, 360°, 180°, respectively.

In Fig. 2.15 the Bézard (1986) averaging method and our full integration method are nearly identical. The Bézard (1986) method decreases computational time by a factor of 18, on average, for the absorption component of the model. The largest thermal deviations occur at $p \geq 526$ mbar and do not affect our stratospheric thermal results. We adopt the Bézard (1986)

averaging method method for all model calculations.

2.7 TEXES Observations

Observed spectra were obtained in November 2005 and April 2007 at NASA's Infrared Telescope Facility (IRTF) using TEXES (Lacy et al. 2002). The 1.4 arcsec wide entrance slit was oriented along the celestial E/W direction and then scanned N/S for the 2005 C_2H_6 observations and the 2007 CH_4 observations. The slit was oriented along the celestial N/S direction and nodded on and off the planet for the 2005 CH_4. Each data set is composed of either many scans or nodded observations co-added together into 10 degree latitude bins at observed Saturnian airmasses of 1-1.2, 1.2-1.5, 1.5-2.0, and 2.0-3.0. A spectral resolving power, $R = \lambda/\Delta\lambda$, of 80,000 was achieved. The observations of the ν_4 band of CH_4 were made between 1246 and 1252 cm^{-1} and the observations of the ν_9 band of C_2H_6 were made between 817 and 822 cm^{-1}. In November 2005 and April 2007, Saturn was at an L_s of 311° and 329.5° and the observer sub latitude point was -21.1 and -18.5 (values of L_s and sub latitude from Astronomical Almanac 2007, 2005).

2.8 Results and Discussion

Figure 2.16 Displays the 5-mbar seasonal temperature profiles from the TMV model relative to the Cess and Caldwell (1979) and Bézard and Gautier (1985) results at the same pressure. The dashed line indicates equatorial latitudes and the solid line indicates south polar latitudes. For model (A)

74

latitudes -8° and -72° are shown (slight ring shadowing is observed at the -8° latitude, as indicated by the bumps bracketing the winter season). Model (B) and (B)1. display results from 0° and -80°. Summer temperatures at the south pole are equivalent for latitudes -72° and -80°. Summer temperatures at -8° and 0° differ by 0 to 2 K following summer solstice until autumnal equinox. The -8° and -72° latitudes for model (A) were chosen due to limitations in the extrapolation of the photochemistry from Moses et al. (2007). The -8° latitude has a temporal dependence (although less pronounced) similar to the high latitude models due to the proximity of perihelion ($L_s = 278°$) and southern summer solstice ($L_s = 270°$).

The TMV model was run for model(A) HITRAN04 + Irwin et al. (2006) and (B) HITRAN04 + GEISA03 near-IR parameterizations (red,cyan). Overplotted in blue is model (B)1. which includes the aerosol opacity. Model (A)1. is not shown since it replicates model (A) temperatures. This latter result was unexpected, but a similar effect was observed by Yelle et al. (2001). The 1999 study of the Uranian stratosphere by Marley and McKay (1999) also showed aerosol heating to be minor. The 5 mbar predictions from Bézard and Gautier (1985) (thin, black) and Cess and Caldwell (1979) (red + black) are shown. Implementing the Bézard and Gautier (1985) mole fractions with the updated value of q_{H_2} produces the thick black line; the peak temperature corresponds well with the Bézard and Gautier (1985) profile. The (B) HITRAN04 + GEISA03 closely tracks the Bézard and Gautier (1985) Voyager-era profile at 5 mbar, but reaches maximum temperature earlier in the season.

Model (A) does not reproduce the observed ζ_g values; model (B)1. best fits observed thermal trends. The modeled ζ_g values are given in Table 2.5 for 1 and 5 mbar.

The seasonal temperatures for four latitudes are depicted in Fig. 2.17. The solid profiles use the (A)1. HITRAN04 + Irwin et al. (2006) + Aerosol τ near-IR (dotted) and (B)1. HITRAN04 + GEISA03 + Aerosol τ near-IR (solid). Only model (B) has been implemented for -50° and -20°. For the south pole and equator, the upper stratospheric ($p < 0.1$ mbar) thermal magnitudes for both model (A) and (B) are similar. Notably, for -80° and 0° latitudes, the peak summer temperatures for both models occur at nearly identical L_s. This suggests that it is the seasonally variable hydrocarbon abundances that control the temporal seasonal responsivity, since both models implemented the same variable abundances.

As seen in Table 2.5, the ζ_g is substantially different between $p = 1$ mbar and $p = 5$ mbar. Likewise, upon inspection of Fig. 2.17, it is clear that $\zeta_g(0.1$ mbar) differs from $\zeta_g(1$ mbar), indicating that stratospheric ζ_g values are very sensitive to pressure. The ζ_g values for model (A), 1 mbar in 2004 (Table 2.5) are not dissimilar to the observationally derived values shown in Table 2.1 for the same pressure. We find that the Greathouse et al. (2005a) derived ζ_g values for 2002, bracketing 10 - 0.01 mbar, only coincide with those from model (A) at $2 < p < 1$ mbar. For $p = 0.1$ and 0.01 mbar, model (A) ζ_g values are +20 K and +12 K, respectively.

Figure 2.18 illustrates the differences between latitudes -72° (solid) and -80° (dash-dot) for model (A) (left) and for latitudes -8° (solid) and 0° (dash-dot) for model (A) (right). Ring shadowing is noticeable at -8° (bracketing the winter season). Stratospheric temperatures are equal at the southern summer

77

TMV: Equatorial to South Pole thermal gradient, ζ_g

TMV Model	$\zeta_g(2002)^a$	P^b	$\zeta_g(2004)^c$	P	$t(\mathrm{T}_{max})$
(A) HITRAN04 + Irwin et al. (2006)	-4.94	5	+3.07	5	2006.5
	+11.51	1	+13.57	1	2005
(A)1. HITRAN04 + Irwin et al. (2006) + Aerosol τ	-4.94	5	+3.07	5	2006.5
	+11.51	1	+13.57	1	2005
(B) HITRAN04 + GEISA03 near-IR	-5.79	5	+1.02	5	2007.2
	+7.69	1	+11.83	1	2005
(B)1. HITRAN04 + GEISA03 + Aerosol τ near-IR	+7.50	5	+14.61	5	2006.4
	+14.80	1	+17.00	1	2004.7

Table 2.5: The thermal gradient (ζ_g) from equator to south pole for the TMV model. The model-predicted maximum temperatures occur in the year $t(T_{max})$ for the south pole, following the peak solar forcing in 2002.

^{a}Kelvin
^{b}mbar
^{c}year

solstice for -72° and -80° between 0.01 and 11 mbar. Equatorial temperatures are equivalent to -8° at southern summer solstice between 5 and 11 mbar. Due to the aforementioned extrapolation problem (above) with the photochemistry, we will refer to -72° results as the south polar results.

Including the Tomasko et al. (2007) multiplicative corrections to the Irwin et al. (2006) k-coefficients result in an increase in summer temperatures at -72° by +3 K at the 5-mbar level and a decrease of -3 K for $p < 1$ mbar. Thermal phase lags remain unchanged providing further evidence that it is the seasonal hydrocarbon abundances that largely determine the stratospheric responsivity.

In Figure 2.20, TEXES 2007 and TEXES 2005 CH_4 spectra are plotted (cyan) for latitudes -8° (top) and -72° (bottom). Overplotted are near-IR parameterizations (A) (purple), (B) (dashed), and (B)1. (red). Model (A)1. is not shown since the temperatures are identical to (A). Overplotted in thin green is the atmospheric transmission spectrum for each data set. The inclusion of the aerosol opacity for parameterization (B)1. acts to increase temperatures relative to (B), resulting in CH_4 emission lines with higher radiance values everywhere except for the 2007 -8° data. For the 2007 data, TEXES spectra are best fit by model (A) at -8°: fits to several line centers are obvious. For the 2007 -72° data, none of the models provide a reasonable fit, although the wings of the TEXES data are fit by model (A) and (B). Model (A) temperatures required a reduction of 5 K to best fit TEXES spectra. For the 2005 data set, both model (B) and (B)1. best fit emission cores at -8° latitude,

but still required a reduction in model temperatures by 1 to 2 K. For the -72°
data in 2007, none of the models fit the observed methane spectra. For both
2005 and 2007, the data sets for -72° are significantly noisier than those for -8°
latitude; strong line cores fall on strong earth atmospheric absorption features.
To address the possibility of an additional ethane enhancement at the south
pole relative to the equator (Greathouse et al. 2005a), the C_2H_6 TMV mole
fraction was enhanced by 1.7 at -80°. Summer temperatures changed by -2.5
K at 2 mbar and by a maximum of -3.7 K at 0.1 mbar.

The temporal relationship between peak solar forcing at southern sum-
mer solstice and maximum southern temperatures is shown in Figure 2.22.
Notably for the three latitudes shown, peak stratospheric temperatures pre-
cede the summer solstice above the 3×10^{-4} mbar level. This is a photochemical
effect, such that the CH_4 in the stratosphere responds to increases in solar forc-
ing by both increased absorption and increased production of photochemical
coolants. Following the extended dark winter for the south pole, spring gives
rise to a substantial increase in solar forcing, causing increased CH_4 absorption
and consequential warming. For example, Fig. 2.21 depicts the TMV seasonal
temperatures for $p = 3 \times 10^{-3}$ mbar. At -72° latitude, no incident solar radia-
tion is observed at this pressure and latitude until $L_s \sim 150°$. Changes in the
seasonal mole fractions (Fig. 2.3) are clearly observed in the resultant seasonal
temperature profiles in Fig. 2.21.

The maximum temporal phase lag from Fig. 2.22 is +30° in L_s at 10
mbar for -72°, +40° in L_s at 10 mbar for -50°, and +50° in L_s at 10 mbar

for -20°. For -72° latitude, near-IR model (A) is shown. The temporal phase lags are consistent among the three models indicating that individual near-IR parameterizations do not effect the temporal seasonal responsivity as a function of pressure in the stratosphere. These temporal phase lags indicate that seasonal response times are faster than the predicted equilibrium radiative disturbance timescale $\xi = 98°$ in L_s from 0.1 - 100 mbar (Conrath et al. 1990). Peak temperatures lag maximum solar forcing by 0° to 60° in L_s for $0.1 \leq p \leq 0.1$ mbar.

There is a significant latitude dependency for the thermal phase lags; most notably as the absolute value of the latitude decreases, peak temperatures precede the maximum solar forcing with greater L_s. For $p < 2 \times 10^{-4}$ mbar, the stratospheric photochemistry is responsive to instantaneous changes in the solar insolation (see Fig. 2.3, Fig. 2.21), hence peak temperatures precede the summer solstice at this level. At low pressures, near 1×10^{-4} mbar, boundary conditions significantly affect the values of the phase lags.

Implementing the PVV mole fractions in place of the TMV mole fractions reduces temperatures at south pole by 4 K at 0.01 mbar and by 6 K at 0.1 mbar. The seasonal phase lags in the upper stratosphere, $p < 0.01$ mbar, exhibit minimal pre-solstice thermal maximums as indicated in Fig. 2.22. The TMV mole fractions result in the detailed thermal responsivity of the stratosphere, indicative of the seasonal and latitudinal variability of the hydrocarbon photochemistry.

Figure 2.23 illustrates the ζ_g values as a function of pressure for the

seasons indicated for model (B)1. For $L_s = 270°$, there is a gradual increase in the ζ_g value until 0.1 mbar, coinciding with the mid-stratospheric level at which C_2H_6 cooling peaks (Fig. 2.5). A turnover in temperatures at 0.1 mbar indicates that below this pressure level, temperatures are still responding to the residual winter lag. This turnover moves toward greater pressure as the season approaches autumnal equinox. At the 10 mbar level, cooling via continuum emission dominates (Fig. 2.5). Near the 100 mbar level for all seasons, relatively no seasonal variation in temperatures is observed ($\zeta_g \rightarrow 0$).

Figure 2.24 displays the 2 mbar seasonal temperatures for the TMV near-IR parameterizations combined with observationally derived temperatures from Cassini (Fletcher et al. 2007; Orton and Yanamandra-Fisher 2005) and ground-based observations (Greathouse et al. 2005a,b). Data for the equator is indicated by squares and for -80° latitude by circles. Temperatures were taken from the seasonal contour plots provided by each source. This plot indicates that the model (A) best fits the Greathouse et al. (2005a,b) equatorial data, while models (B)1. and (B) best fit the Cassini trends and the Greathouse et al. (2005a,b) polar data, respectively. Model (A) cannot replicate the observationally derived ζ_g values.

2.9   Conclusion

It has been shown that implementing an improved radiative seasonal model for Saturn's stratosphere using seasonally adaptive hydrocarbon abun-

dances in conjunction with updated physical information can produce temperature trends in Saturn's stratosphere that are comparable with current observations. However, the thermal trends derived from our temporally, meridionally, and vertically variable model (TMV) are sensitive to the choice of near-IR parameterization: (1) use of the HITRAN04 (2000 - 4800 cm^{-1}) + Irwin et al. (2006) (4800 - 9500 cm^{-1}) does not reproduce the observationally derived equator-to-south pole thermal enhancement (ζ_g) for $p = 5$ mbar but does fit TEXES 2007 CH$_4$ data (1247 - 1251 cm^{-1}) for -8° and (2) use of the HITRAN04 (2000 - 4800 cm^{-1}) + GEISA03 (4800 - 9500 cm^{-1}) near-IR line data does reproduce the magnitude of the derived equator-to-south pole thermal enhancement model results only fit TEXES 2007 CH$_4$ spectra at -8°. No models fit TEXES CH$_4$ spectra at -72° for years 2005 and 2007. Detailed conclusions are listed below.

1. This research reveals that accurate near-infrared CH$_4$ line data would be optimal for retrieving exact seasonal temperature variations for the Saturnian stratosphere. The Irwin et al. (2006) k-coefficient data set is the most complete shortwave near-infrared data set to date, for application to giant-planet atmospheres. Use of this data set in the TMV model created here ably reproduces TEXES CH$_4$ (1247 - 1251 cm^{-1}) spectra at -8° latitude, but has difficulty in reproducing the observationally derived ζ_g values (Table 2.5,2.1). This may suggest that dynamics play a role in the redistribution of photochemical byproducts (ethane and acetylene), which would alter the radiative balance in the stratosphere.

2. Several separate parameterizations of near-infrared CH_4 absorption were tested: (A) HITRAN04 (2000 - 4970 cm^{-1}) + Irwin et al. (2006) k-coefficients (4970 - 9500 cm^{-1}), (A)1. HITRAN04 (2000 - 4970 cm^{-1}) + Irwin et al. (2006) k-coefficients (4970 - 9500 cm^{-1}) + aerosol opacity, (A)2. HITRAN04 (2000 - 4970 cm^{-1}) + Irwin et al. (2006) k-coefficients (4970 - 9500 cm^{-1}) + Tomasko et al. (2007) multiplicative corrections + aerosol opacity, (B) HITRAN04 (2000 - 4970 cm^{-1}) + GEISA03 (4970 - 9500 cm^{-1}), and (B)1. HITRAN04 (2000 - 4970 cm^{-1}) + GEISA03 (4970 - 9500 cm^{-1} + aerosol opacity.

   (a) Parameterization (A) and (A)1. produce identical seasonal profiles. Parameterization (A)2. possesses the same thermal phase lags as (A) and (A)1. but is cooler by -4 K for $p < 1$ mbar and warmer by +3 K for $p \sim 5$ mbar. Parameterization (A) produces spectra comparable to TEXES 2005 and 2007 CH_4 spectra but cannot produce the observationally derived trend of increasing temperature from equator-to-pole (ζ_g) for 2002 and 2004 (Greathouse et al. 2005a,b; Orton et al. 2005; Flasar et al. 2005; and Howett et al. 2007).

   (b) Parameterization (B) produces thermal responses and ζ_g values comparable to observations (Greathouse et al. 2005a,b; Orton et al. 2005; Flasar et al. 2005; and Howett et al. 2007), but results in warmer seasonal temperatures than observationally derived. The input TMV model temperatures were changed by +7 K at the equator and -14 K at -72° latitudes in order to generate CH_4 spectra that

fit TEXES 2007 CH$_4$ spectra. TEXES 2005 spectra are fit well by this model at -8°. For 2005, the TMV model temperatures were decreased by 10 K at -72° to fit TEXES data.

(c) Parameterization (B)1. (model (B) plus an aerosol opacity) produces a reasonable fit the observationally derived temperatures for 2005 data at -8° and reproduces the observed thermal responsivity and ζ_g values, despite the fact that the GEISA03 line list used from (4970 - 9500 cm^{-1}) is incomplete. This may suggest that the approximations used for missing near-IR shortwave ground-state energies from Brown (2005) are adequate for stratospheric, equatorial modeling. Relative to TEXES CH$_4$ spectra, the TMV temperatures required a reduction of 7 K (at -72°) and 0 K (at -8°) in 2005 and 12 K (at -72°) and +7 K (at -8°) in 2007.

(d) Implementation of Bézard and Gautier (1985) constant mole fractions combined with near-IR parametrization (B) (without aerosol opacity) in the TMV model produces 5 mbar seasonal temperatures and phase lags comparable to those from Bézard and Gautier (1985) and Cess and Caldwell (1979).

3. Testing the uncertainty in the [CH$_4$]/[H$_2$] ($4.5\pm0.9\times10^{-3}$) (Flasar et al. 2005) produces a minimal decrease in seasonal temperatures of -4 K. Enhancing the C$_2$H$_6$ abundance at -80° latitude by a factor of 1.7, as suggested in the conclusions of Greathouse et al. (2005a), decreases summer temperatures by -5 K.

4. Due to the adaptation of TMV hydrocarbon abundances, the stratospheric phase lags between peak solar forcing and maximum temperature are latitudinally and pressure dependent. This has not been previously detailed for the Saturnian stratosphere. Phase lags are shorter (-10 to +50° in L_s for all tested latitudes) than perturbed radiative dissipation timescales (+65° in L_s) (Conrath et al. 1990) at the 0.1 - 10 mbar level. For model (A)1., at $p = 1 \times 10^{-3}$ mbar, peak stratospheric temperatures precede the summer solstice due to photochemical effects by -10° in L_s at -80°.

5. The location of the mesopause and stratopause, as a function of pressure, is seasonally dependent. For the south pole, the location of the stratopause occurs at lowest pressure at southern summer solstice. The mesopause is located at the lowest pressure near southern winter solstice.

2.10 Acknowledgments
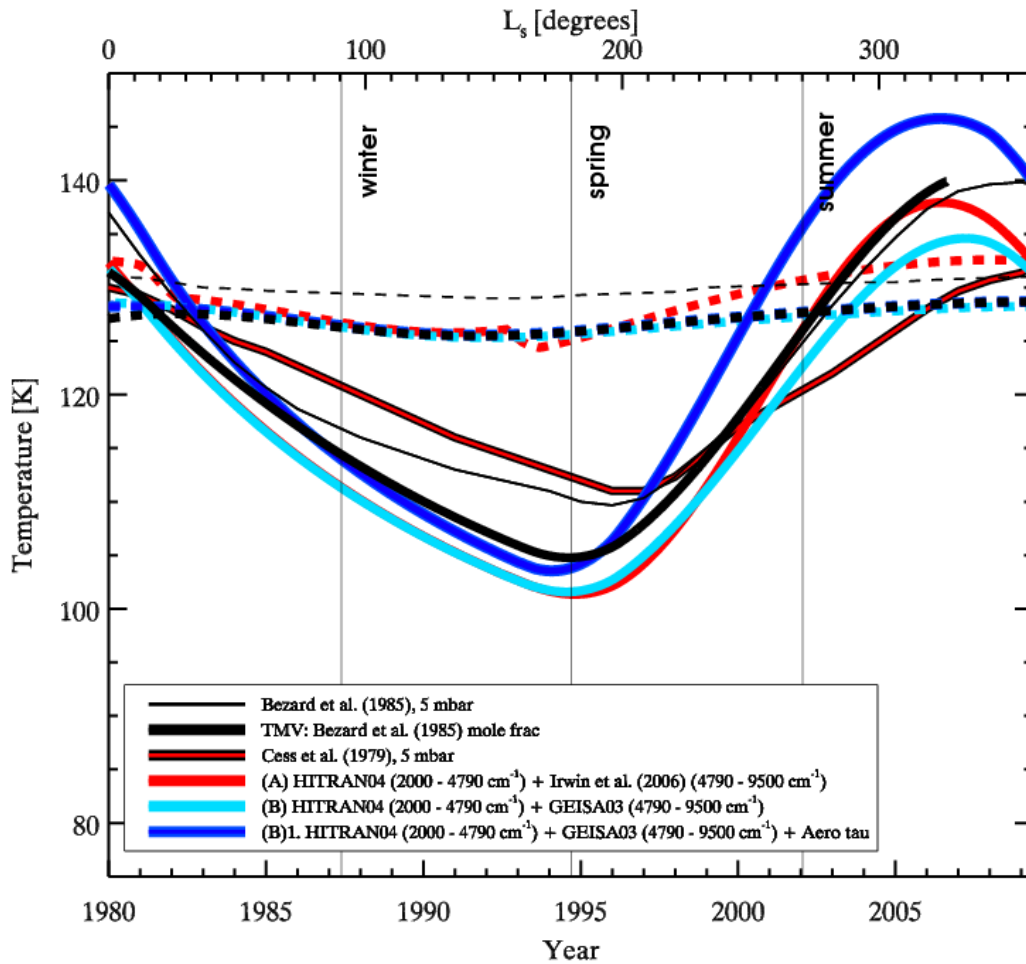
Figure 2.16: The 5 mbar seasonal temperatures predicted by the TMV model with the implementation of the (A) HITRAN04 + Irwin et al. (2006) (red: -72° and -8°) and (B) HITRAN04 + GEISA03 near-IR parameterizations (blue and cyan: -80° and 0°). Dashed lines indicate low latitude (near the equator) and solid lines indicate southern polar latitudes. Ring shadowing is observed at the -8° (red, dashed) latitude. Overplotted are the 5 mbar predictions from Bézard and Gautier (1985) (thin, black) and Cess and Caldwell (1979) (outline black + red). The TMV model with Bézard and Gautier (1985) mole fractions produces results similar to the Bézard and Gautier (1985) model (thick black). Model (B)1. best fits observed trends of ζ_g (Table 2.1). Southern summer solstice occurs on October 29, 2002 ($L_s = 270°$) (Astronomical Almanac 2002).
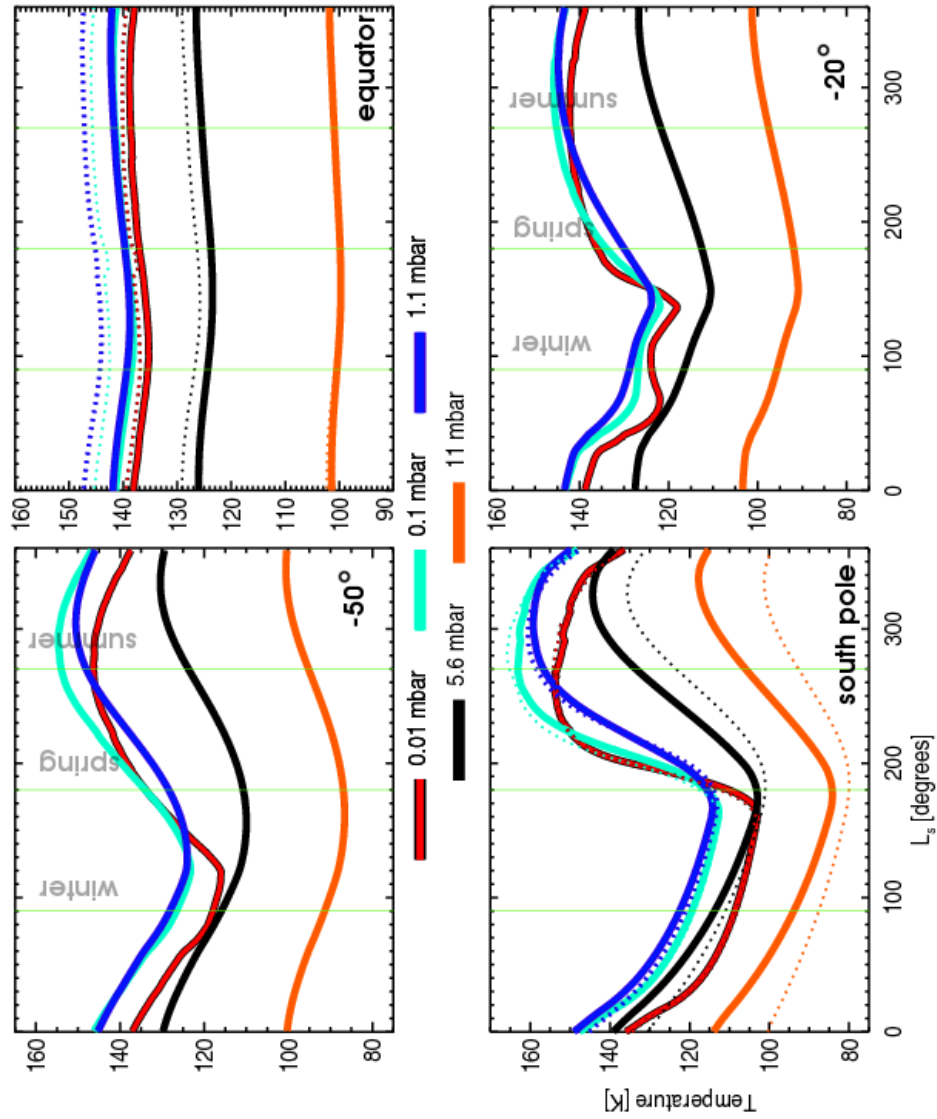
Figure 2.17: Seasonal temperature profiles for 4 latitudes using near-IR parameterization (A)1. HITRAN04 + Irwin et al. (2006) + Aerosol τ near-IR (dotted) and (B)1. HITRAN04 + GEISA03 + Aerosol τ near-IR (solid). Solid vertical lines indicate solstices ($L_s = 90, 270°$) and equinoxes ($L_s = 180, 360°$).
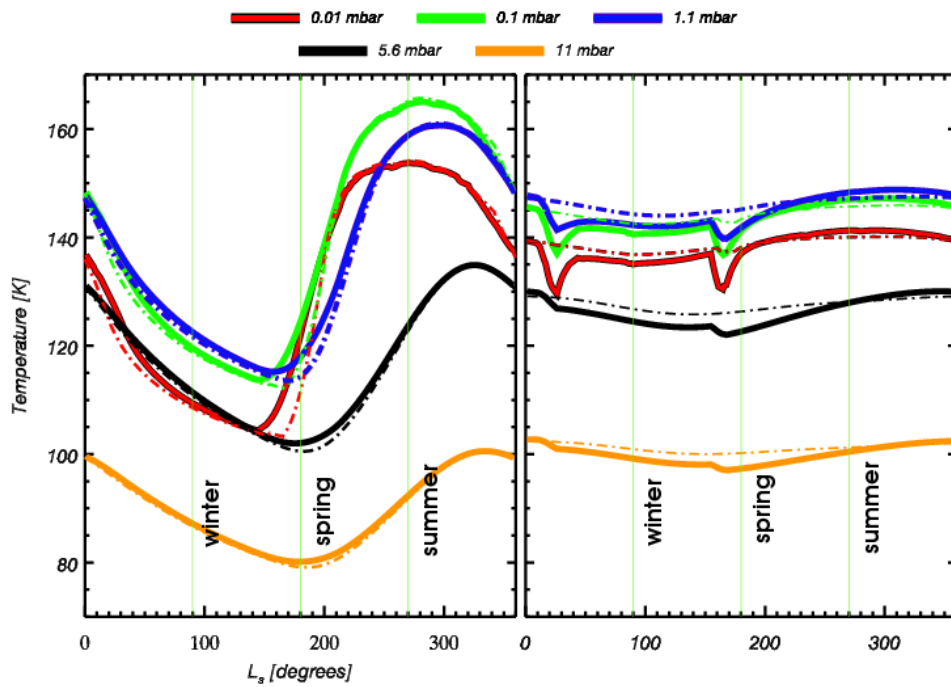
Figure 2.18: Seasonal temperature profiles for -80° (dash-dot) and -72° (solid) at left and 0° (dash-dot) and -8° (solid) at right using the near-IR parameterization (A).
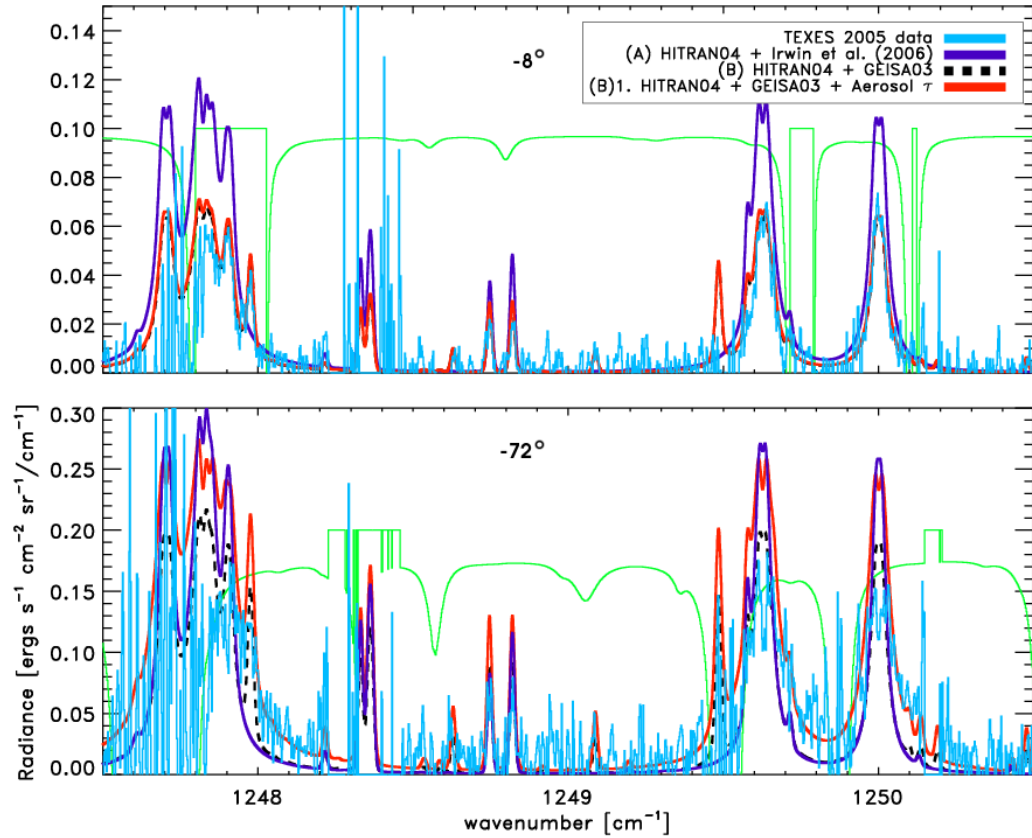
Figure 2.19: TEXES 2005 CH$_4$ spectra (1247.5 - 1250.5 cm^{-1}) (light blue) are displayed. Overplotted are the predicted CH$_4$ spectra using TMV model temperatures for the same time for near-IR parameterizations (A) (dark blue), (B) (dashed), and (B)1. (red). Model spectra are generated with the Greathouse et al. (2005a) model.
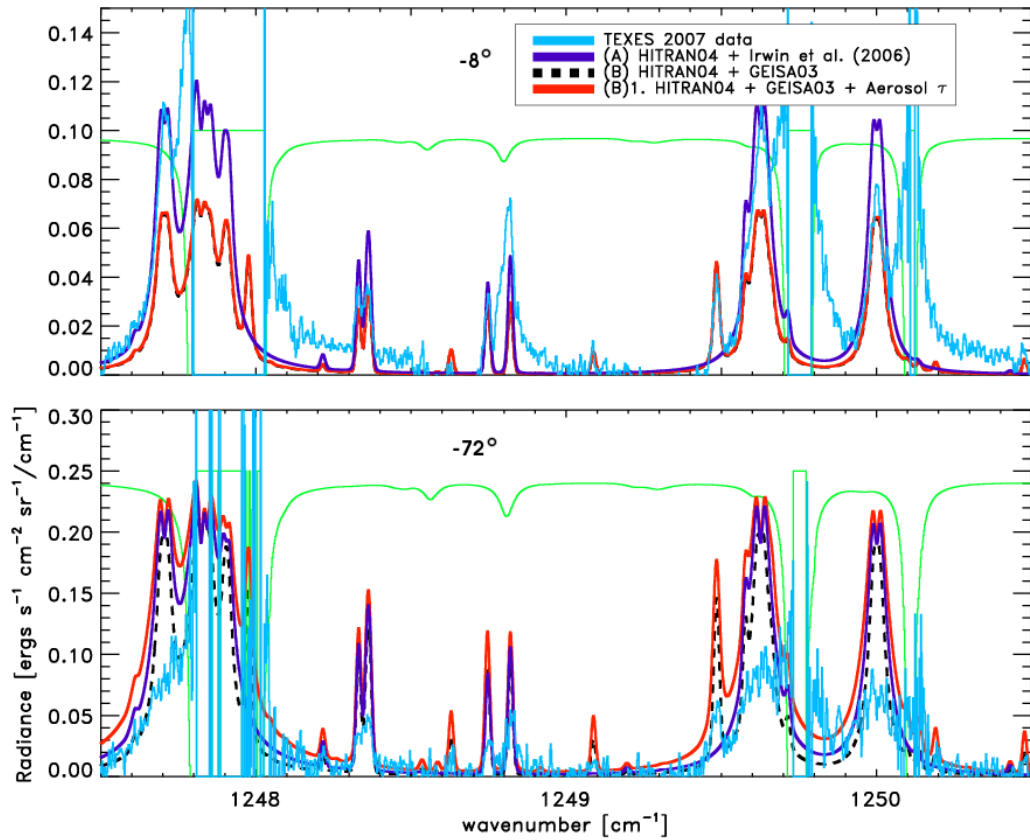
Figure 2.20: TEXES 2007 CH$_4$ spectra (1247.5 - 1250.5 cm^{-1}) (light blue) are displayed. Overplotted are the predicted CH$_4$ spectra using TMV model temperatures in the Greathouse et al. (2005a) model for the same time for near-IR parameterizations (A) (dark blue), (B) (dashed), and (B)1. (red).
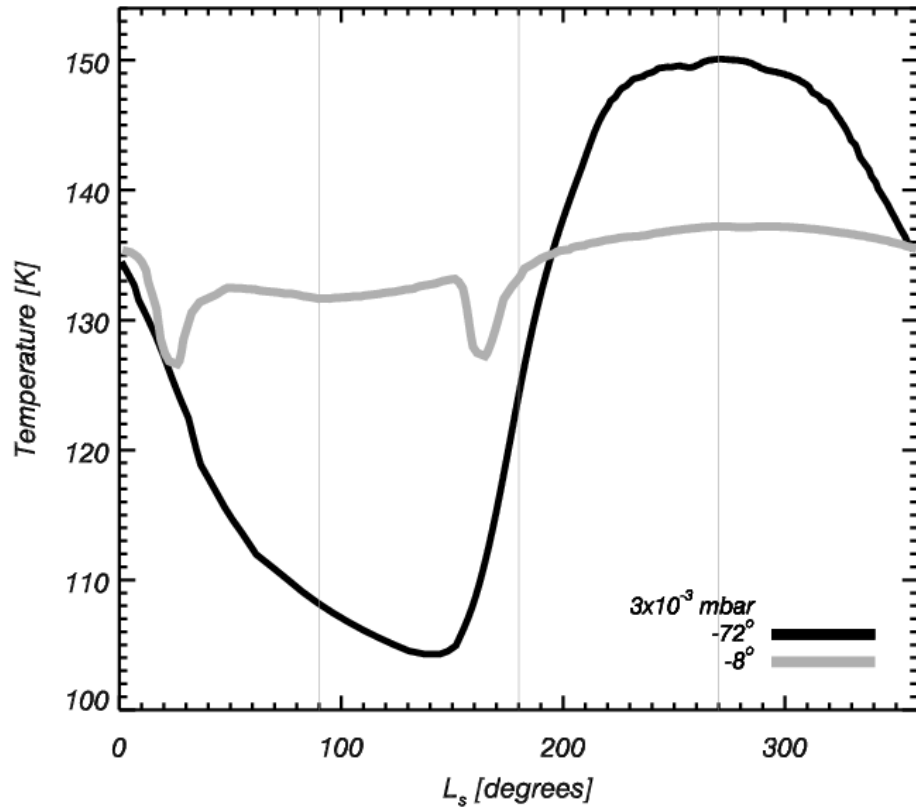
Figure 2.21: Seasonal temperatures for $p = 3 \times 10^{-3}$ mbar for latitudes -72° and -8° from model (A). This pressure level is sensitive to photochemical changes (Fig. 2.3).
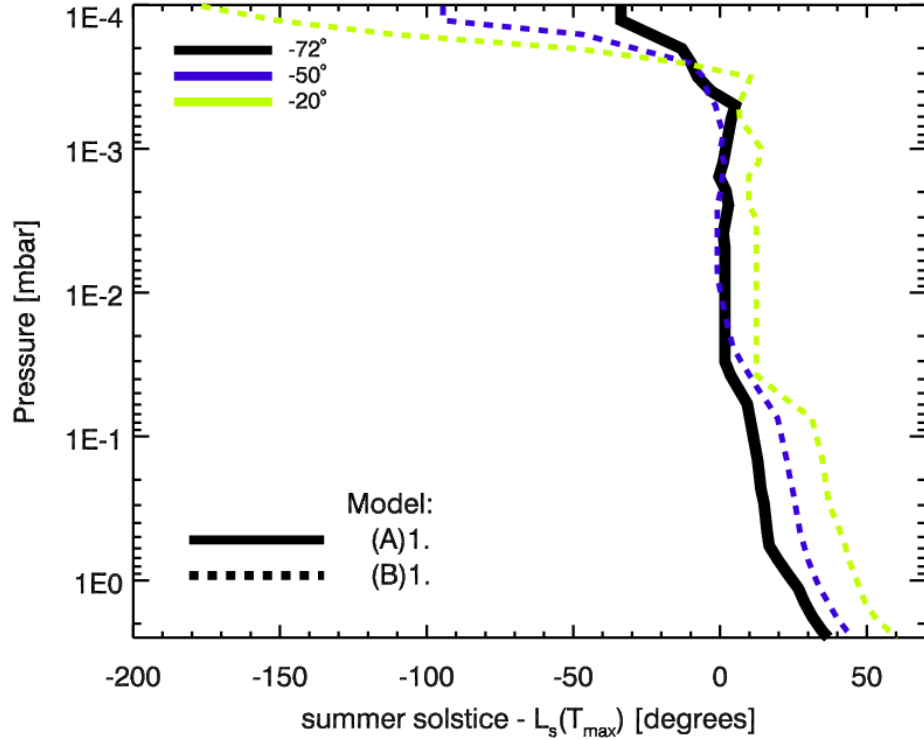
Figure 2.22: The phase lag between peak solar forcing ($L_s = 270°$) and maximum stratospheric temperatures for latitudes -72°, -50°, and -20°. Results are shown for the near-IR parameterizations (A) (solid) and (B)1. (dashed). At $p < 0.1$ mbar and in particular, at $p < 2 \times 10^{-4}$ mbar, the stratospheric photochemistry is responsive to instantaneous changes in solar insolation (see Fig. 2.3), hence peak temperatures precede the summer solstice at this level. Note that -20° is more sensitive to solar distance than to solar latitude but behaves similarly to the other latitudes since perihelion occurs near summer solstice.
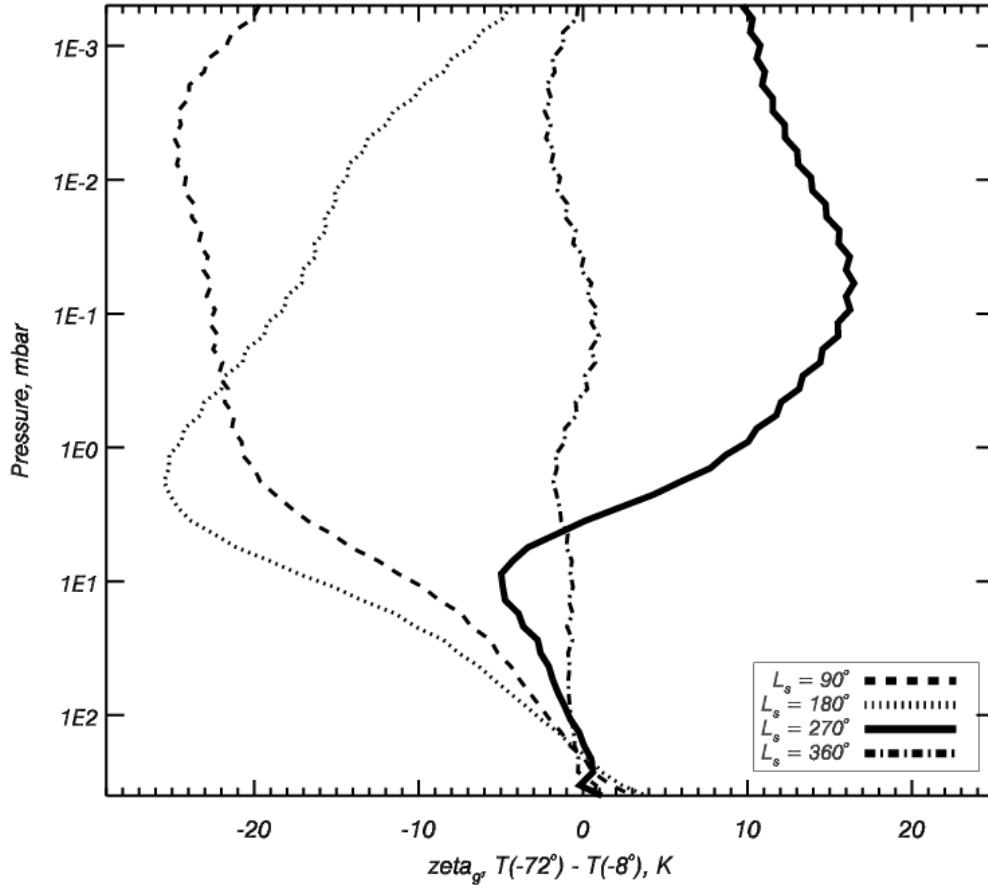
Figure 2.23: The ζ_g values as a function of season. $L_s = 360°$ coincides with 2010. At southern summer solstice (270°) there is an inversion in ζ_g at 0.1 mbar, such that below this level, the stratosphere remains responsive to the past winter phase lag.
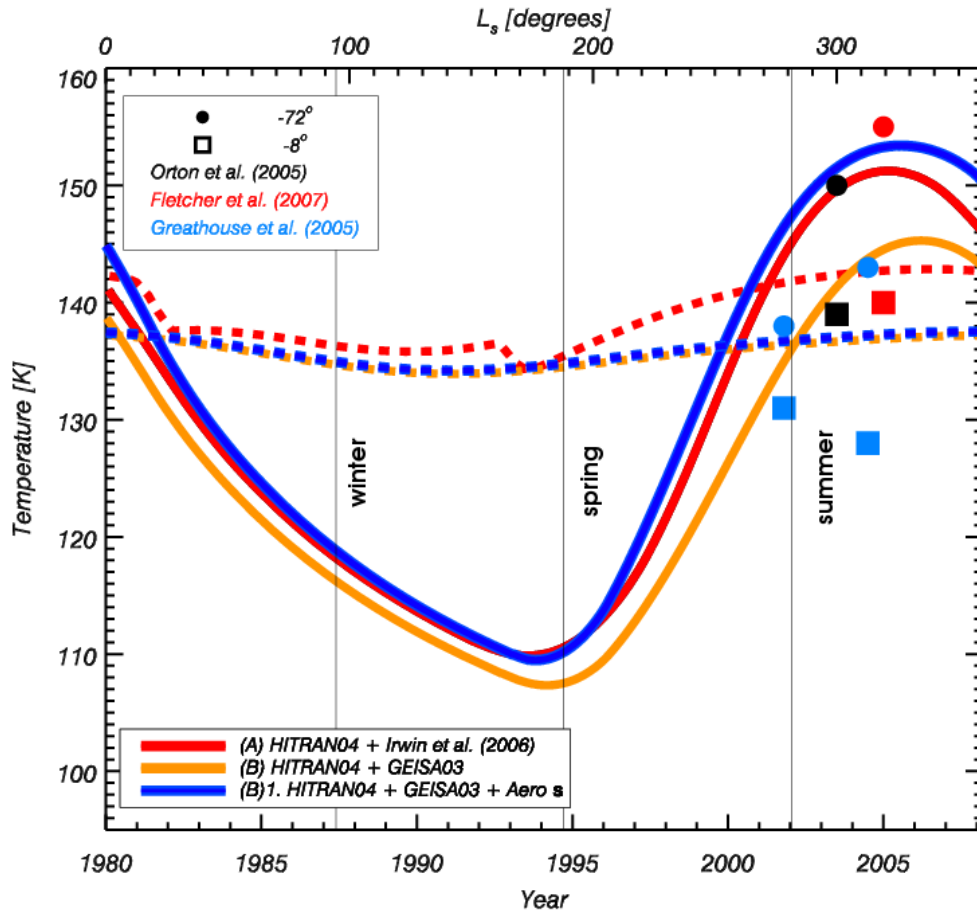
Figure 2.24: 3 mbar seasonal temperatures for the three TMV near-IR param-
eterizations combined with observationally derived temperatures from Cassini
(Fletcher et al. 2007; Orton and Yanamandra-Fisher 2005) and ground-based
observations (Greathouse et al. 2005a,b). Equatorial data is represented by
squares and polar data by circles. Solid lines are south polar temperatures
and dashed lines are for equatorial latitude. (Derived temperatures from ob-
servations are identical for both -72° and -80° and for 0° and -8° within the
error of ±2 from extracting the values from the published contour plots.)

Chapter 3

Model Validation

3.1 Radiative Transfer: By-Hand versus Model Calculations

The complete seasonal radiative climate model consists of numerous subroutines, numerical recipes, multiple conditional statements, and many iterative loops. As a result, it is imperative to compare model output to a simple "back-of-the-envelope" by-hand calculation. Predominantly, it is imperative that the model is correctly performing the radiative transfer calculations.

As discussed in Chapter 2, the model is divided into two components: the absorption component (2000 to 10^5 cm^{-1}) and the emission component (0 to 1600 cm^{-1}). Radiative transfer calculations for the absorption component are based on the diurnal integration or averaging of the solar flux as a function of optical depth in the atmosphere. For the emission component, the model uses the Goukenleuque et al. (2000) formalism.

The absorption radiative transfer component may be calculated via two methods, as discussed in Chapter 2. The first method uses a diurnal integration procedure and the second uses a diurnal averaging procedure:

1.

$$dF(dp)_1 = F_o e^{-\tau/\cos z} \cos z (1 - e^{-d\tau(dp)/\cos z}), \qquad (3.1)$$

$dF(dp)$ is the amount of flux absorbed within a pressure layer with F_o is the incident solar flux at the top of the atmosphere, τ is the total optical depth down to level dp, and $\cos z$ is the cosine of the incident solar zenith angle. This calculation is performed once per solar zenith angle, which changes relative to season and latitude. The total flux based on a day's worth of insolation is

$$\langle dF(dp) \rangle_{day} = \frac{\int_{\alpha_o}^{0} dF(dp) d\alpha}{\Psi}, \qquad (3.2)$$

with Ψ equal to the number of seconds in a Saturn day and α is the hour angle of the sun and varies between dawn ($\alpha = \alpha_o$) and noon ($\alpha = 0$). (Further detailed explanation on the derivation of these equations may be found in Chapter 2).

2.

$$dF(dp)_2 = F_o \langle \cos z \rangle e^{-\tau/\langle \cos z \rangle_{day}} (1 - e^{-d\tau(dp)/\langle \cos z \rangle_{day}}), \qquad (3.3)$$

where $\langle \cos z \rangle$ and $\langle \cos z \rangle_{day}$ are the average value of the cosine of the zenith angle over to full day and night period and for the day period only. At the top of the atmosphere, this equation is no longer an approximation. Within the stratosphere, the value of $\langle \cos z \rangle_{day}$ may inaccurately account for daily changes in solar zenith angle resulting in an escalation or decrement of solar deposition at high pressures. (See Chapter 2 for details on the $\langle \cos z \rangle$ calculation.)

The thermal radiative transfer component was calculated based on the formalism of Goukenleuque et al. (2000) (discussed in detail in Chapter 2).

$$
\begin{aligned}
F_i(\tau) = \quad & 2\pi \quad [a_{i+1}E_3(|\tau - \tau_{i+1}|) - a_i E_3(|\tau - \tau_i|)] \\
+ \quad & 2\pi \quad \frac{(a_i - a_{i+1})}{|\tau_i - \tau_{i+1}|}|E_4(|\tau - \tau_i|) - E_4(|\tau - \tau_{i+1}|)| \\
+ \quad & 2\pi \quad E_3(\tau_b - \tau)B(T_b),
\end{aligned}
\tag{3.4}
$$

such that $F_i(\tau)$ is the flux of atmospheric level i, bounded by pressure levels p_i and p_{i+1}. The Planck function in layer i is assumed to vary linearly as a function of optical depth: $B(\tau) = a_{i+1} + (a_i - a_{a+i})[(\tau - \tau_{i+1})/(\tau_i - \tau_{i+1})]$, with a_i as the Planck function value at level i and τ_i the optical depth of level i. The model's bottom boundary pressure level is indicated by the b notation. The exponential function, E_n, is the nth exponential function, $E_n(\tau_\nu) = \int_1^\infty (exp(-\tau_\nu t)/t^n)dt$, where t is the airmass, $\sec z$.

The derived model values for the $dF(dp)$ for a single molecular line in the emission component and two molecular lines in the absorption component are shown in Fig. 3.1 and Fig. 3.2. These values are compared to a simplified calculation performed without the model. For the absorption component, both the diurnal integration and diurnal averaging methods were tested. For the thermal component, the model's Goukenleuque *et al.* (2000) formalism is tested against a simple two-stream approximation for the radiative transfer

98

where

$$F_\nu^+(\tau, \mu) = 2\pi \quad B_\nu(\tau_*)T_\nu[(\tau_* - \tau)/\mu]$$
$$- 2\pi \int_\tau^{\tau_*} B_\nu(\tau')\frac{d}{d\tau'}T_\nu[(\tau' - \tau)/\mu]d\tau', \tag{3.5}$$
$$F_\nu^-(\tau, -\mu) = 2\pi \quad B_\nu(TOA)T_\nu(\tau/\mu)$$
$$+ 2\pi \int_0^\tau B_\nu(\tau')\frac{d}{d\tau'}T_\nu[(\tau - \tau')/\mu]d\tau'. \tag{3.6}$$

The upward flux as a function of $\mu = \sec z$ is then F_ν^+ and the downward flux is F_ν^-. The combined total emitted flux is

$$F_\nu(\tau) = F_\nu^+(\tau) - F_\nu^-(\tau). \tag{3.7}$$

Notably, the by-hand calculations are similar, if not identical to, the model calculations. This indicates that the model's radiative transfer is being performed correctly.

3.2 $F(\nu)$ Spectrum

As an additional test of model validation, the TMV flux spectrum $(F(\nu))$ for a given wavenumber range was plotted for the top of the model atmosphere. This flux spectrum contains the incoming and outgoing flux in the mid-infrared for ethane (819.5 to 819.7 cm^{-1}). In Figure 3.3, $F(\nu)$ at the top of the atmosphere is plotted in black. To compare against results for a separate model, overplotted in blue, red and purple are results from using the Greathouse et al. (2005a) model with the TMV temperature-pressure profiles
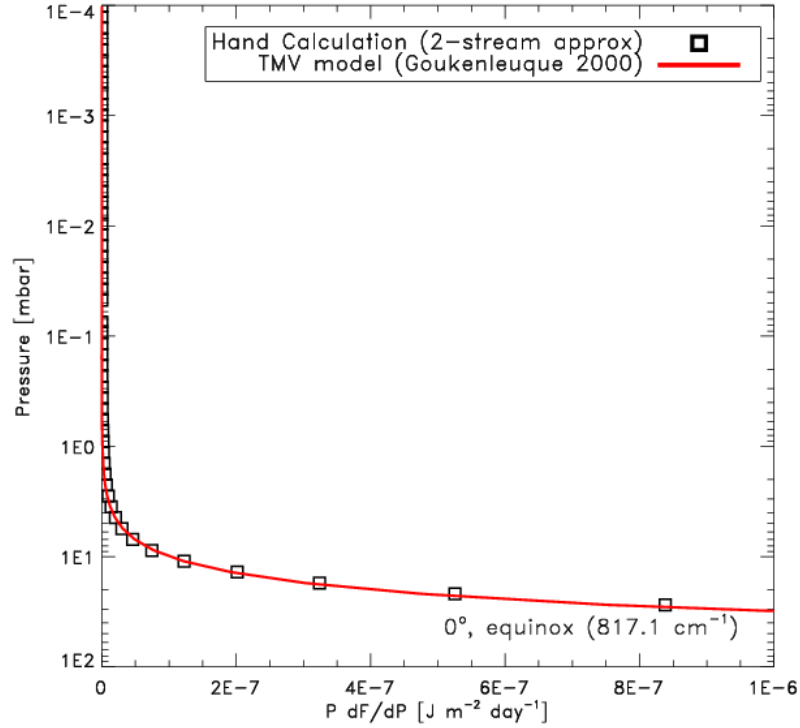
Figure 3.1: The PdF/dP (J m^{-2} day^{-1}) calculated from the model (solid red) and by-hand (squares) for a single spectral line of ethane at 817.7 cm^{-1} for a latitude of 0° and at equinox.

and mixing ratio information. Since the TMV model produces a flux spectrum (in W m^{-2} cm^{-1}) and the Greathouse et al. (2005a) model generates an intensity spectrum (in ergs s^{-1} cm^{-2} sr^{-1}/cm^{-1}), we have plotted the Greathouse et al. (2005a) model results for a latitude of -55° to compensate for the angle averaging and have converted the Greathouse et al. (2005a) units to W m^{-2} cm^{-1} by multiplying by $\pi/1 \times 10^3$. The TMV model was not run for -55° latitude, and therefore the mixing ratios and temperatures supplied to the

100
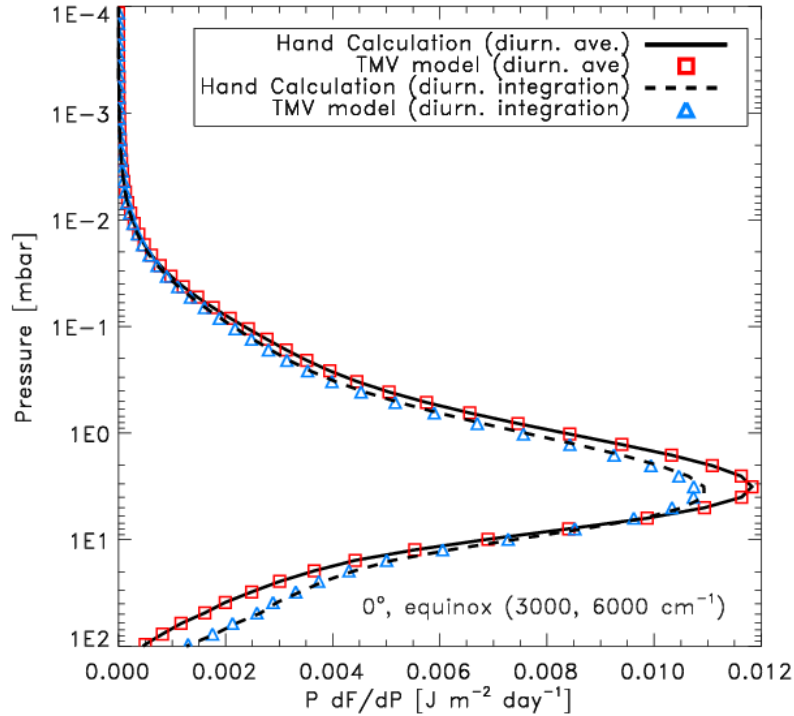
Figure 3.2: The PdF/dP (J m^{-2} day^{-1}) calculated from the model based on the diurnal averaging method (red squares), from the model based on the diurnal integration method (blue triangles), by-hand with the diurnal averaging method (solid line), and by-hand with the diurnal integration method (dashed line). Values are for a combination of two spectral lines of methane in the near infrared at 3000 and 6000 cm^{-1} for a latitude of 0° at equinox.

Greathouse et al. (2005a) model are for -72° latitude (with model (A) Irwin et al. (2006) + HITRAN04 near-infrared parameterization) (red), -8° (with model (A) Irwin et al. (2006) + HITRAN04 near-infrared parameterization) (blue), and -50° (with model (B) HITRAN04 +GEISA03 near-infrared parameterization) (purple). The -8° temperature + mixing ratios (blue) fit the line

wings well as do the -72° temperature + mixing ratios (red). The vertical offset in line intensity is due to not having the exact temperature profile and mixing ratios for -55° latitude.
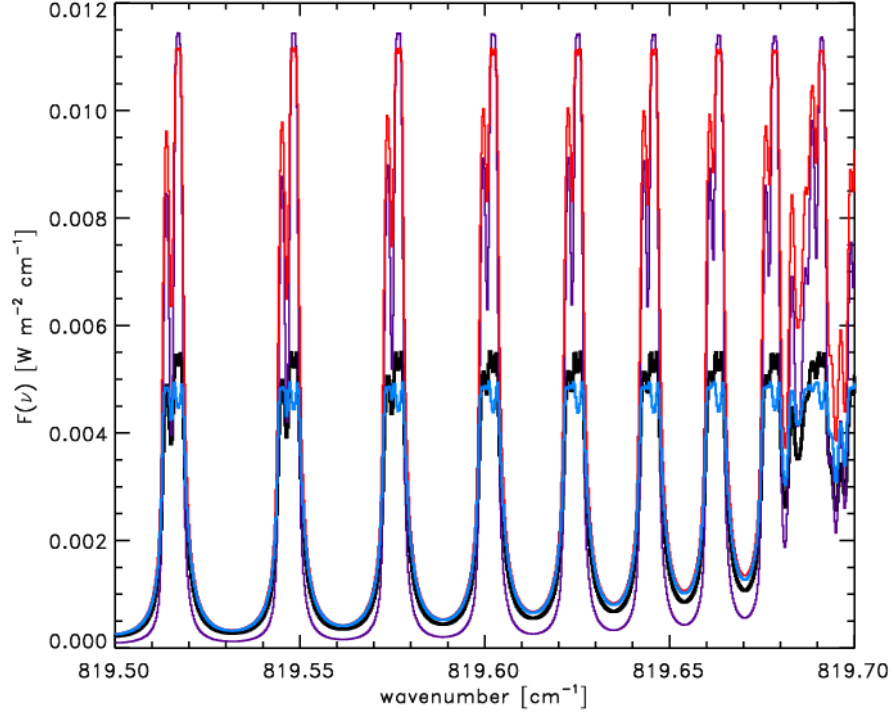
Figure 3.3: The flux spectrum of ethane at the top of the atmosphere (black) from the TMV model. Overplotted are the Greathouse et al. (2005a) model results with implementation of TMV temperature-pressure profiles and mixing ratios for latitudes -8° (cyan), -72° (red), and -50° (purple). Since the Greathouse et al. (2005a) model outputs spectra in units of intensity (ergs s^{-1} cm^{-2} sr^{-1}/cm^{-1}), we have converted the units to flux (W m^{-2} cm^{-1}) by multiplying by $\pi/1 \times 10^3$ and viewing the spectra at a latitude of -55° to account for the angle averaging. Wings are fit well by both the temperatures and mixing ratios of -8° (cyan) and -72° (red) latitudes (both were generated with model (A) Irwin et al. (2006) + HITRAN04 near-infrared parameterizations. The vertical discrepancy is due to not having the exact temperature and mixing profiles for -55° latitude.

Chapter 4

Near-Infrared CH$_4$ and Gas Giant Atmospheres

Chapter 2 briefly discussed the significance of and uncertainty in near-infrared (near-IR) laboratory methane spectra. A complete CH$_4$ near-IR line data set would be ideal for precise gas-giant climate modeling. However, due to laboratory limitations, we are presently limited to near-IR band models generated from short-pathlength spectra at temperatures and pressures inconsistent with gas-giant stratospheric conditions.

The radiative balance between stratospheric absorption of solar near-IR and thermal emission via mid-infrared (mid-IR) and far-infrared (far-IR) has been shown to be extremely sensitive to the choice of near-IR parametrization (Chapter 2). This chapter provides a more detailed discussion and attempts to highlight the laboratory procedures involved in the determination of CH$_4$ transmission spectra.

4.1 The Significance of Near-infrared CH$_4$

Strong et al. (1993) argued that because absorption bands of methane dominate in the visible and near-IR spectra of Jupiter, interpretation of Jo-

vian spectra is critically dependent on the awareness of spectroscopic CH_4 parameters.

For the long pathlengths within the giant planets' atmospheres, centers of strong near-IR CH_4 bands are saturated. The wings of the strong bands and centers of weak bands, in turn, become more important. HITRAN04 (Rothman et al. 2005) and GEISA03(Jacquinet-Husson et al. 1999) databases have improved since the Bézard and Gautier (1985); Cess and Caldwell (1979); Strong et al. (1993) studies, but knowledge of weak bands in near-IR CH_4 line lists remains absent due to the quantum mechanical complexity of higher vibrational bands. These near-IR spectral regions are very compounded and overlapping, requiring quantum mechanical models to discern interactions between different states and transitions Rothman et al. (2005). Beyond 4800 cm^{-1}, there has been limited success in producing measurable intensities and transition energies due to the laboratory difficulty involved. Consequentially, low-resolution absorption coefficients for methane must be supplemented to interpret near-IR CH_4 observations (Strong et al. 1993; Baines et al. 1993; Irwin et al. 2006) and to model gas-giant atmospheres. Even though the absorption coefficient method provides a means to model shortwave near-IR methane, the method possesses drawbacks.

From laboratory generated transmission spectra of CH_4 in short pathlength gas cells ($\leq 5 - 13$ m), absorption coefficients may be inferred, since

105

the transmission is defined as

$$
\begin{aligned}
\mathfrak{T}(\nu, T, p) &= e^{-\tau(\nu,T,p)/\mu} \\
&= e^{-k(\nu,T,p)U(T,p)/\mu},
\end{aligned}
\tag{4.1}
$$

where $\tau(\nu, T, p)$ is the optical depth as a function of wavenumber, temperature, and pressure, μ is the cos of incident angle z, $k(\nu, T, p)$ is the absorption coefficient, and $U(T, p)$ is the column density.

The measurement of precise CH_4 absorption coefficients in the laboratory at temperatures, pressures, and pathlengths remotely comparable to giant atmospheres is currently impossible. Pathlengths in the giant planets are long, $\sim$ 20 to 50 km (comparable to the scale heights of their atmospheres, see Fig. 1.2 in Chapter 1.2). The cold temperatures and low atmospheric pressures in the giant atmospheres can required multiple passes through long gas cells at high pressures in order to produce measurable CH_4 absorption (Tomasko et al. 2007). Extrapolation is then required to derive the amount of methane absorption in the outer planets.

The Strong et al. (1993) laboratory measurements were motivated by the prospect of Near Infrared Mapping Spectrometer (NIMS) data of Jupiter from Galileo in 1995. NIMS spectra would probe the thermal profile of Jupiter from 1 bar down to the first opaque cloud layer between 0.7μm - 5.2μm. The course resolution of NIMS (0.025 μm) and the absence of weak line CH_4 data in the near-IR forced the use of low-resolution transmittance models. These 'band' models involve the fitting of near-IR laboratory measurements

of frequency-averaged transmittance, which are a function of laboratory pressure, temperature, and abundance. Band models have been used for terrestrial applications dating back to Goody (1952) and prior. The Strong et al. (1993) band model is believed to be the most accurate for k-distribution techniques (Irwin et al. 2005) since the data set covers a wide spectral range and were measured over long path lengths. Section 4.2 discusses the band model approach. Section 4.3 details the k-coefficient fitting.

4.2 The Band Model

Band models allow for the analytical calculation of transmission in terms of band parameters. These band parameters are based on a statistical distribution of absorption lines (Lacis and Oinas 1991).

The first laboratory application of the band model to CH_4 was done by Fink et al. (1977) in the visible regime. Fink et al. (1977) implemented the Goody random band model with a Lorentz line-shape[1] and became the first to provide a quantitative picture of the methane spectrum up to 1μm (Strong et al. 1993).

A *band model*, or *random band model*, or *statistical* or *Goody-Meyer band model* are different names for the same type of model. Random comes from the irregular spatial distribution of line positions within spectral bands (e.g. water vapor).

---

[1]Lorenztian line shapes are best applied to pressure-broadened lines emanating from the lower atmosphere. Radiative transitions are disturbed by molecular collisions

From Goody (1964), radiative heating involves several scales of frequency-dependence: (1) variation, as a function of frequency, of the Planck function and its derivative with respect to temperature, (2) band contour shape and expanse over a range of frequency (e.g. for water vapor, bands may have a full width at half maximum of 300 cm^{-1} and the Planck function spanning this range cannot be assumed to be constant.), (3) the frequency dependence of spacing of rotational lines of rotating molecules, and (4) frequency dependence of the Beer-Lambert law of absorption[2]. Due to these dependencies, it has been desirable to establish a technique for averaging over fine structure. The idea of the band model is to smooth out lines by averaging over a small frequency range, producing average absorption functions that can approximate a full band.

For a random band model, the band interval is given a width $\Delta\nu$ and consists of n lines of average separation δ: $\Delta\nu = n\delta$ (Thomas and Stamnes 2002). If line positions are not correlated, the band transmission is written as the products of the individual line transmittance $\langle \mathcal{T}_i \rangle$, where the transmission $\mathcal{T}_b = I[\tau(\nu)]/I_o = \exp[-\tau(\nu)]$. The absorptance (i.e. the ratio of the absorbed intensity $I_o - I[\tau(\nu)]$ to the incident intensity I_o, $\alpha_b(\nu) = 1 - \mathcal{T}_b(\nu)$, is expressed as:

$$
\begin{aligned}
\langle \mathcal{T}_b \rangle &= \langle \mathcal{T}_1 \rangle \langle \mathcal{T}_2 \rangle ... \langle \mathcal{T}_n \rangle = \left[\frac{1}{\Delta\nu} \int_{\Delta\nu} d\nu \int_0^\infty d\mathcal{S} p(\mathcal{S}) e^{-\mathcal{S}u\phi(\nu)} \right]^n \\
&= \left[1 - \frac{\langle \alpha_b \rangle}{n} \right]^n.
\end{aligned}
\tag{4.2}
$$

---

[2]Transmission $T = I_1(\nu)/I_o(\nu) = \exp(-\tau(\nu))$

$\mathcal{S}$ is the line strength and is multiplied by the line profile ϕ. The mass of the column is u. The optical depth may then be defined as $\tau(\nu) = \mathcal{S}u\phi(\nu)$. The $p(\mathcal{S})$ expression defines the analytic line-strength distribution. The most common distributions are the

$$\text{exponential distribution}:$$
$$p(\mathcal{S}) = (1/\bar{\mathcal{S}})\exp(-\mathcal{S}/\bar{\mathcal{S}}) \tag{4.3}$$
$$\text{Godson distribution}:$$
$$p(\mathcal{S}) = \bar{\mathcal{S}}/(\mathcal{S}_{max}\mathcal{S})(\mathcal{S} < \mathcal{S}_{max})$$
$$\text{Malkmus distribution}:$$
$$p(\mathcal{S}) = (1/\mathcal{S})\exp(-\mathcal{S}/\bar{\mathcal{S}})$$
$$p(\mathcal{S}) = 0(\mathcal{S} > \mathcal{S}_{max}). \tag{4.4}$$

The mean line strength is $\bar{\mathcal{S}}$. Line profiles ϕ can be described as Lorentz (pressure) broadened, Doppler broadened, or Voigt (Lorentz + Doppler) broadened.

In the limit $n \to \infty$ and $(1 - x/n)^n \to e^{-x}$, the transmittance in Eq. 4.2 becomes

$$\langle \mathcal{T}_b(u) \rangle = e^{-\langle \alpha_b(u) \rangle}. \tag{4.5}$$

This expression states that the beam transmittance of random, overlapping spectral lines is 'equal to the exponential of the non-overlapping single-line beam absorptance' (Thomas and Stamnes 2002).

4.3 k-Distributions

Since absorption coefficients are repetitive functions of wavenumber, it has been determined that it is more efficient to integrate the transmission function over a subinterval consisting of similar absorption coefficients rather than integrating over wavenumber (Lacis and Oinas 1991). This allows for computational efficiency.

Band models may be fitted with k-distribution parameters, where the k is the absorption coefficient. Within a spectral interval of $|\nu_o - \nu_1|$ wavenumbers, there will be a set of $i = N$ repeating k-coefficients. The statistical distribution of these absorption coefficients k_i is given by Δg_i.

The k-distribution function $f(k)$ is defined as

$$f(k)dk = \frac{1}{\nu_2 - \nu_1} \sum_m \Delta\nu_m, \tag{4.6}$$

where ν_2 and ν_1 define the spectral interval, $\Delta\nu_m$ is the width of the subinterval within which the absorption coefficient is between k and $k + dk$. The value $f(k)dk$ represents the total fraction of the spectral interval for which the absorption coefficient is within the valued-range of k and $k + dk$. The cumulative k-distribution can be defined as

$$g(k) \equiv \int_o^k f(k)dk. \tag{4.7}$$

Historically, the inverse of $g(k)$ is used to describe the k-distribution, $k(\nu) = g(k)^{-1}$. Because $g(k)^{-1}$ is a smoother function than the spectral distribution of $k(\nu)$, the transmission profile along the g-ordinate is well approximated by

summing a small number of Gaussian quadrature terms (Temma et al. 2006).

From the transmission function found by fitting a band model (see above) to laboratory spectra, the k-distribution of the absorption coefficient spectrum is estimated. This process is also referred to as exponential sum fitting. The mean transmission ($\bar{\mathcal{T}}(u)$) as a function of column mass (u) is approximated by the exponential sum:

$$\bar{\mathcal{T}}(u) = \sum_i^N \exp(-k_i u) \Delta g_i, \tag{4.8}$$

Baines et al. (1993) fitted k-coefficients to the band model of Giver et al. (1990). The Giver et al. (1990) data set does not account for hydrogen-broadening[3], were measured over short path-lengths, and covers a small spectral range. The Strong et al. (1993) band model was fitted with k-coefficients by Irwin et al. (1996) and included hydrogen- and self-broadening[4], long path lengths, and a broad spectral range. In 1998, Sihra (1998) presented new measurements of self-broadened methane transmission spectra at lower temperatures than Strong et al. (1993). However, the Sihra (1998) data were self-broadened only and covered shorter path-lengths than the Strong et al. (1993) data. As a result, Irwin et al. (2005) fitted k-coefficients to the new Sihra (1998) data set combined with the Strong et al. (1993) data. The Irwin et al. (2006) data added the weak near-IR CH_4 absorption pointed out by Sromovsky et al. (2006).

---

[3]Collisions with hydrogen molecules. This dominates in the stratospheres of outer planets since they are predominantly H_2 in composition

[4]Collisions with neutral atoms of the same type

Lacis and Oinas (1991) discussed the k-coefficient technique in detail with application to a non-gray[5] atmosphere. The authors argue that use of the Curtis-Godson approximation in a band model may be inappropriate for modeling non-gray atmospheres due to pressure-induced changes in spectral features. The Curtis-Godson approximation has been implemented by Sihra (1998), which served at the band model of the Irwin et al. (2006) k-distribution data. Lacis and Oinas (1991) found an overall 5% overestimation in the stratospheric (> 30 km for Earth) cooling rates they determined using a multi-layered nongray atmosphere when compared to a line-by-line treatment.

---

[5] **gray atmosphere:** optical depth τ is independent of frequency

Chapter 5

TMV Users Manual

This documentation describes the Temporally, Meridionally, Vertically (TMV) radiative seasonal climate model Strong (2008). Users please proceed with caution; this model contains many inter-dependent variables and changing one may severely alter computations. Here I have attempted to address all possible uses and modifications. TMV radiative seasonal climate model is written in Fortran 90 and has been complied with several different compilers, including the Intel Fortran 90 compiler. However, predominately the Portland Group's Fortran 90 Compiler (pgf90) has been used on 3.0 GHz Pentium 4 processors with 1.0 GB of RAM.

There is a two-part process to running the TMV model. First, a grid of optical depths for the mid-infrared (from GEISA03 Jacquinet-Husson et al. (1999)), and near-infrared if desired, for a nominal temperature-pressure profile are generated using the **lbyl_real8_hr.f** line-by-line program. This is detailed in Section 5.3. Once the opacity files have been created and stored in the appropriate directory structure, Section 5.1, the radiative transfer program **seasmod2.f** may be run for a single user defined latitude and set of parameters. Specific input files are required and logical statements should be verified,

113

Section 5.2 and Section 5.1.

Technicalities as to scientific assumptions are typically left out in this document, as they are better detailed in Chapter 2.

Output units are typically SI: units of flux are in W m^2, pressures are in bar, temperature in kelvin.

5.1 Setting up the directory structure

In order to appropriately compile all files, you will need to make a *Makefile* or alias in the .cshrc file for both the radiative transfer code and the line-by-line code. For the radiative transfer code, this would look something like

```
alias satradHR 'pgf90 -Bstatic ../nsubs/nir8_hitran.f ...
```

and for the line-by-line code,

```
alias lbylbeowhr 'pgf90 -Bstatic ../nsubs/TIPS_2003sub.f ...
```

A complete list of all the required subroutines is located in Appendix B.2.

The basic directory structure is as follows. In the users home directory, set up the path

```
/home/SAT/nsubs/
```

where 'SAT' is for Saturn, but feel free to change this name for other planets. All FORTRAN programs should be contained within the `nsubs/` directory.

In this directory, create the path `LAT/`. The directory `LAT/` will contain at least two directories: `t26` and `p40_opacityHR/`. The `t26` directory is the "tilt" directory. Based on the user-defined tilt of the planet, the program will look for a "tilt" directory that is an `int()` value of the tilt with `t` as a prefix. For example, Saturn has a 26.7° axial tilt and the program will look for the directory `LAT/t26`. If the obliquity was set equal to zero, the directory would be `LAT/t00`. The `p40_opacityHR/` directory will contain all the opacity information.

Within the "tilt" directory, latitude directories must be created. The code will take the `int()` value of the user supplied latitude and tack on an `m` or `p` for plus or minus latitudes and place `degrees` as the suffix. Within this last directory, create a four letter/number directory. This will be the `workdir` and a new one should be created for each individual model run (unless you want to overwrite data). For example, for Saturn with an obliquity of 26.7° and for -80° latitude and a model run date of January 1, the directory structure should now look something like below.

`/home/SAT/nsubs/LAT/t26/m80degrees/0101/`

5.2   Input files
5.2.1   Line-by-line input files

In order to run the `lbyl_real8_hr.f` the input files needed should be located in the `/home/SAT/nsubs/` directory.

115

1. `mixsatmoses2000sep.dat`: For Saturn this is the mixing ratio file.

2. `sat_info.dat`: Includes the 3-letter name of the planet, the mixing ratios of helium and hydrogen, the mean molecular weight of the atmosphere, and the D/H ratio.

3. `var_script_shay`: Allows one to change the percentages of the molecular mixing ratios used.

5.2.2 Radiative model input files

Most input for the radiative model should be located in either the opacity directory or the `/home/SAT/nsubs/` directory:

1. `var_script_shay`: Allows one to change the percentages of the molecular mixing ratios used. Same as for `lbyl_real8_hr.f` and located in `/home/SAT/nsubs/` directory.

2. `pt_ch4.out` and `pt_start.out`: These are located in the opacity directory and are the starting temperature-pressure profiles. The file `pt_start.out` is typically a temperature-pressure profile that has been modified and is only opened if the logical command 'tempread' is `.true.`.

3. `mixsatmoses2000sep.dat`: Located in the `/home/SAT/nsubs/` directory, this file is the TMV chemistry from Moses et al. (2007).

4. `lsubs.inp`: The orbital parameters from the JPL ephemeris, located in `/home/SAT/nsubs/`.

116

5. `goodavekin24sls270short2.pun`: A modified Moses temperature-pressure profile located in `/home/SAT/nsubs/`.

6. `2005tsi2.txt`: Solar flux output from SOLAR2000 located in the opacity directory.

7. `1995lo_karko.tab` and `1995hi_karko.tab`: Karkoschka Karkoschka (1994, 1998) visible-wavelength methane absorption coefficients.

8. `cross_*.inp`: The cross sections for the UV region from Moses located in the opacity directory. There should be 4 files: CH_4, C_2H_2, C2H$_6$, C2H$_4$.

9. `kmod.csv`: Irwin et al. (2006) methane absorption information located in the `/home/SAT/nsubs/` directory.

5.3 Line-by-line: generating opacity files

Compile the line-by-line code using your alias or makefile. Upon running the compiled executable, you will be prompted for the wavelength region (mid-infrared, far-infrared, nir-infrared GEISA03/HITRAN04) and molecule (CH_4, C_2H_2, C_2H_6, continuum). Note that for the mid-infrared, all molecules may be (individually) selected. However, the far-infrared is only set up for continuum emission and the near-infrared can only do methane, as written.

Input line-data should be placed in a directory within `SAT/nsubs/model` as written. The variable `gasf(1)` indicates the molecular file of interest.

Output opacity files are unformatted with a record-length that is 4 × `nwn`, where `nwn` is 16000 and is the number of wavelength points in an individual file. As things are set up, the mid-infrared resolution is 2.8×10^6 requiring 172 opacity files each with 16000 wavelengths in them and the near-infrared GEISA03/HITRAN04 resolution is 1.7×10^5 with 18 opacity files and 16000 wavelengths in each. The mid-infrared resolution is a little excessive, and may be tweaked to a smaller value (namely 1.4×10^6).

The output opacity file has dimension $\tau(16000, 70, 12)$ for the mid- and near-infrared, where 16000 is the wavenumber set, 70 is the number of atmospheric pressure layers, and 12 is the number of temperatures ranging from -50 K to +60 K from nominal. For the far-infrared, there are less wavenumbers and $\tau(600, 70, 12)$.

Line-by-line calculations will generate a corresponding temperature-pressure profile. You may use this profile as your "guess" starting temp-pressure profile, in which case, copy the file to your work directory.

5.4 Running the TMV

To run the TMV model, be certain the resolutions and pressure scales used in the line-by-line calculations are identical to those in the seasonal model $(R, scale, p(1))$. These are defined in the *'script_seasmod'* scriptfile. A sample script-file can be found in Appendix B.1 along with short variable descriptions. Similarly, ensure that the number of layers (*nlay*) and the number of planet days per year (*pday*) in the codes are identical. *pday* should correspond to the

number of entries in the provided *lsubs.inp* file. These are the only variables that must be changed within the code, as they are not defined in the script-file. These may be found at the top of the code.

Upon running the model from your generated executable, you will be prompted for the desired 'workdirectory';

```
Workdirectory (4 characters):
```

Again, your workdirectory should be in the `SAT/nsubs/LAT/`*tilt*`/`*m80degrees*`/` path, where *tilt* and *m80degrees*`/` should be changed for your setup. Please provide a 4-character directory at the prompt. This directory should contain your starting temp-pressure profile.

5.5   Flags

You will need to assess several logical statements and provide the best setup for your run. These should be modified in the script-file (Appendix B.1). It is important to note that several logical statements must be used in combination. These certain combinations are detailed in Table B.2. You must choose 2 different sets of combinations to run the program effectively: (1) an *Opacity Params* combo and (2) a *Mole Fraction/Mixing* combo. The former combination defines the opacity set used for NIR calculations and the later defines the type of mole fractions you will be using (e.g seasonal, constant, etc.).

Opacity Params
hit_geisa + nir_hitgeisa
hitran + nir_hitirwin
nir_irwinonly
Mole Fraction/Mixing Params
JULIEHOT + juliepun2 (+ seas_ch4, jpundouble)
JULIEHOT + juliedouble
JULIEHOT + bruno

Table 5.1: Logical flag combinations

There are several crucial variables that may be changed for testing purposes. The integer **KJ** determines the wavenumber steps implemented in each time step. It is equivalent to the number of opacity files required to step through the far-infrared through to the ultraviolet. The variable **WNF(1)** will be the starting wavelength at each time step. If you would like to test just a portion of the spectrum, say the 3 μm band of the near-infrared, **WNF(1) = 2494.7435133** and **KJ = 173,225**. For all normal full TMV runs, you will not need to change these, although be sure the starting **WNF(1) = 0**.

The major output files are coded as '82_*.out'. In these files, the atmospheric pressure [bars], the $dT/dt(p)$, and the temperature T are written out in an unformatted file:

```
open(82,file=workdir//'82_'//stgday//'.out',
&          form='unformatted',access='direct',recl=4*nlay)
write(82,rec=1) (real(p(ll)),ll=1,nlay)
write(82,rec=2) (real(dtdt_lay(ll)),ll=1,nlay)
write(82,rec=3) (real(tnews(ll)),ll=1,nlay)
close(82).
```

5.5.1   TMV Subroutine Options

For the mid-infrared and far-infrared, if you would like to test the individual contributions of different molecules, flags within the mid- and fir-infrared subroutines can be changed. Notably, in `mid8hr.f` the following logical statements may be changed accordingly, based on whether or not you

121

would like to add their effects to the emission component:

```
ct=.true.

ch4=.true.

c2h2=.true.

c2h6=.true.

c3h8=.true.
```

For the far-infrared, `fir8.f`, only the continuum may be switched on or off (of course, if it is switched off, there really is no point in including the far-infrared at all):

```
ct=.true.
```

5.6   Final Word

This concludes the TMV users manual. Planet specific variables should only be contained within the script-file, making the model applicable to any planet given the appropriate user input files and orbital parameters. For problems and assistance, please email `shay@wickedchickenz.com`.

Chapter 6

Conclusion

This body of work has presented the detailed development of an improved radiative seasonal climate model for the stratospheres of giant planets. The Saturnian stratosphere has been detailed extensively (radiative responsivity of the stratosphere, phase lags, thermal trends).

Prior to this work, stratospheric modeling was limited to the Voyager-era models (Cess and Caldwell 1979; Bézard and Gautier 1985; Conrath et al. 1990) which reproduced observed autumnal trends for the Saturnian stratosphere, but were unable to persist in applicable predictions for the current influx of Cassini and ground-based observations (Greathouse et al. 2005a,b; Orton et al. 2005; Flasar et al. 2005; and Howett et al. 2007). With the new model developed for this dissertation, current observational trends can be modeled. However questions remain regarding the possibility of the redistribution of methane photochemical byproducts, ethane and acetylene, via stratospheric dynamics, and, in turn, how this potential redistribution affects the radiative balance in the stratosphere. Exact CH_4 shortwave near-infrared line data would be optimal in order to best constrain the possibility of and need for stratospheric dynamics.

The stratospheric heating and cooling rates provided for Saturn from this modeling endeavor are currently the most complete seasonally dependent rates produced. These rates can be implemented in the complex General Circulation Models (GCMs) in order to examine the effects of circulation. Ultimately, a combined radiative, dynamical, and chemical model is needed to best analyze giant planet atmospheres. The work presented here has established the first component, and ultimately the foundation, for a better model, and better picture, of the Saturnian stratosphere.

Appendices

Appendix A

Appendix #1

A.1 Solar Longitude, L_s

Solar longitude (L_s) (sub-solar longitude) defines the current season, as a function of orbital location, for a planet. Seasons, of course, are created by the axial tilt of the planet (see Chapter 1.2). The elliptical orbit of planetary revolution is assumed to have $360°$. Each season (depending on the planet's axial tilt and ellipticy of the orbit) occurs at $\frac{1}{4}360°$ intervals, such that for the southern hemisphere, autumnal equinox (fall) is $L_s = 0°$ or $360°$, winter solstice is $L_s = 90°$, vernal equinox (spring) is $L_s = 180°$. This is a convenient system for describing the current location of planets with seasons, especially since the ellipticity of the planets' orbits vary and seasons do not always coincide with $\frac{1}{4}$(planet year) (in units of fractional year).
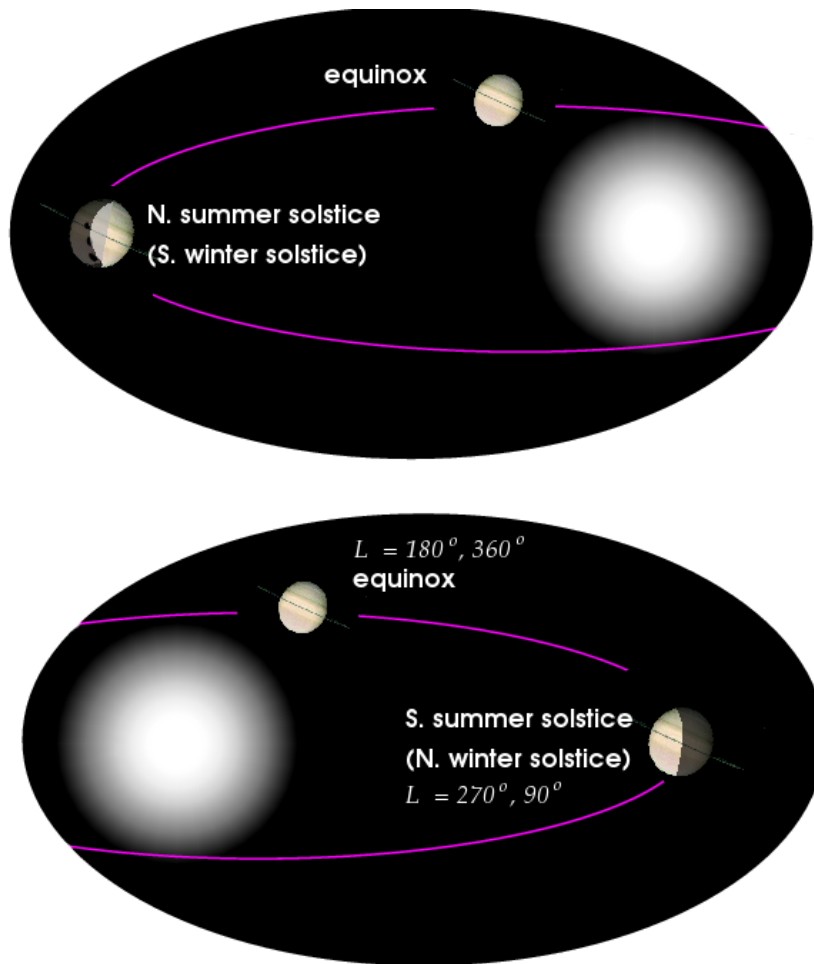
126

Figure A.1: Pictorial view of L$_s$.

Appendix B

Appendix #2

B.1   TMV Script-file

The following table details a sample script-file required to run the TMV model. Variable descriptions are included.

$script\_seasmod$	'variable name': description
.false.	'skipwrite': fast model run; writes out mix ratios as func. of season, no radiative calcs.
.false.	'write_ff': write out mix ratios
.false.	'rates_write': write out heat/cool rates
.false.	'tausum': write file where $\tau = 1$ in atm.
.true.	'ftot_wn': write out $F(\nu)$
.false.	'fluxtot_write': write out $\Sigma F(p)$, collapsed over wavenumber
.true.	'nir_hitgeisa': (3) NIR: GEISA03/HITRAN04
.true.	'hit_geisa': (3) NIR: GEISA03 + HITRAN04
.false.	'hitran': (2) NIR: HITRAN04 only OR HITRAN04 + Irwin (06)
.false.	'nir_hitirwin': (2) HITRAN04 + Irwin (06)
.false.	'nir_irwinonly': (1) Irwin (06) only
.false.	'irwinhalf': approx. Tomasko (07) corrections
.true.	'absfact': use Tomasko (07) multiplicative corr.
.true.	'juliepun2': TMV (usu. true)
.false.	'jpundouble': change mole fractions in seasonal TMV model (double, 1/2, etc.)
.true.	'seas_ch4': use CH_4 seasonal TMV abundances
	Continued on next page

128

script_seasmod	'variable name': description
.false.	'juliedouble': Non-TMV hydrocarb. modifications (usu false)
.true.	'JULIEHOT': Must be true
.true.	'tempread': use prev. derived temp profile (*82_*.out* files).
.false.	'bruno': bruno constant mixing ratio; *juliepun2* = .false.
.false.	'cloud': cloudgrey opacity
2	'secstep': stepsize is in 1 second if equal to 1
.true.	'aerosol':(3)b. aerosol opacity source
.false.	'scattering': when false, uses Tomsvisabsorp.f; true, uses DISORT
.false.	'obltrig': true: tilt=0., l_s=0.
.true.	'bdiurn': use Bruno's diurnal approx. qtr=1
26.7	'obl': obliquity
0.	'lat': latitude to be modelled
4	'nyear': number of planet years to run
0.002226	'xm': M_w molecular weight
0.877	'qh2': abundace of H_2
60268.	'req': Radius at equator
54364.	'rpole': Radius of pole
1.02E-7	'p(1)': pressure [bar] at TOA
0.2273	'scale': pressure scale
'SAT'	'planet':planet
10.66	'hrday': hours in a planet day
2800000.	'res': Mid-IR resolving power
1.52e6	'resnir': NIR resolving power (if using HITRAN, GEISA)

Table B.1 – continued from previous page

B.2   Files Required to Launch the Seasonal Model

Subroutine	Input files
seasmod2.f (main)	scriptfile, var_script_shay, starting temperature profile, mixsatmoses2000sep.dat, lsubs.inp, goodavekin24sls270short2.pun, kin2mbar1e10_shay.pun, 2005tsi2.txt, sunflux_invcm.dat
gravsub.f	
pscale.f	
irwin_rewrite.f	irwinH_iii.par
tominterp.f	
mixr.f	
column.f	
locate.f	numerical recipe
fir8.f	
mid8hr.f	opacity_mir* files
nir8.f	
irwin.f	kmod.csv (Irwin et al. (2006) k-coeffs)
irwin_only.f	kmod.csv (Irwin et al. (2006) k-coeffs)
polin2.f	numerical recipe
nir8_hitran.f	HITRAN/opacity_nirch4_* files
vis18.f	1995lo_karko.tab
vis28.f	1995hi_karko.tab
vis38.f	1995lo_karko.tab
uv8.f	cross_ch4.inp,cross_c2h2.inp,cross_c2h4.inp,cross_c2h6.inp
nir8_ir.f	
tomsfast_new.f	
shadow.f	shadgeneral.out
brunodiurn.f	
callbruno.f	
DISORT.f	calls several subroutines. See DISORT documentation
tomsvisabsorp.f	
diurnaltest.f	
lbyl_real8_hr.f (lbyl)	mixsatmoses2000sep.dat,sat_info.dat,var_script_shay
hitranever.f	
lbylshay.f	
tips_2003.f	
profile6.f	
	Continued on next page

Table B.2 – continued from previous page	
Subroutine	**Input files**
h2hesubver.f	

Bibliography

M. Allen, Y.-T. Lee, E. W. Weisstein, and E. Serabyn. Dynamical Mixing in the Jovian Upper Troposphere. In *Bulletin of the American Astronomical Society*, volume 29 of *Bulletin of the American Astronomical Society*, pages 1017–+, July 1997.

S. K. Atreya. Composition, clouds, and origin of Jupiter's atmosphere - a case for deep multiprobes into giant planets. In A. Wilson, editor, *Planetary Probe Atmospheric Entry and Descent Trajectory Analysis and Science*, volume 544 of *ESA Special Publication*, pages 57–62, February 2004.

K. H. Baines, R. A. West, L. P. Giver, and F. Moreno. Quasi-random narrow-band model FITS to near-infrared low-temperature laboratory methane spectra and derived exponential-sum absorption coefficients. *Journal of Geophysical Research (Planets)*, 98:5517–5529, March 1993.

B. Bézard. *Variations saisonnière de la structure thermique et composition chimique de Jupiter, Saturn, et Uranus*. Univ. Paris 7, Paris, France, 1986.

B. Bézard and D. Gautier. A seasonal climate model of the atmospheres of the giant planets at the Voyager encounter time. I - Saturn's stratosphere. *Icarus*, 61:296–310, February 1985.

B. Bezard, D. Gautier, and B. Conrath. A seasonal model of the Saturnian upper troposphere Comparison with Voyager infrared measurements. *Icarus*, 60:274–288, November 1984.

J. Borysow, L. Frommhold, and G. Birnbaum. Collison-induced rototranslational absorption spectra of H2-He pairs at temperatures from 40 to 3000 K. *Astrophysical Journal*, 326:509–515, March 1988.

A. P. Boss. Formation of gas and ice giant planets. *Earth and Planetary Science Letters*, 202:513–523, September 2002.

S. Brönnimann, F. C. Siegrist, W. Eugster, R. Cattin, C. Sidle, M. M. Hirschberg, D. Schneiter, S. Perego, and H. Wanner. Two case studies on the interaction of large-scale transport, mesoscale photochemistry, and boundary-layer processes on the lower tropospheric ozone dynamics in early spring. *Annales Geophysicae*, 19:469–486, April 2001.

L. R. Brown. Empirical line parameters of methane from 1.1 to 2.1@mm. *Journal of Quantitative Spectroscopy and Radiative Transfer*, 96:251–270, December 2005.

R. D. Cess and J. Caldwell. A Saturnian stratospheric seasonal climate model. *Icarus*, 38:349–357, June 1979.

R. D. Cess and S. C. Chen. The influence of ethane and acetylene upon the thermal structure of the Jovian atmosphere. *Icarus*, 26:444–450, December 1975.

A. Chedin, N. Husson, and N. A. Scott. GEISA - a Data Base for the Study of Phenomena of Radiative Transfer in Planetary Atmospheres. *Bulletin d'Information du Centre de Donnees Stellaires*, 22:121–+, February 1982.

E. Colón and T. E. Dowling. EPIC Simulations of Topographic Effects on the General Circulation of Venus. In *Bulletin of the American Astronomical Society*, volume 32 of *Bulletin of the American Astronomical Society*, pages 1120–+, October 2000.

B. J. Conrath and D. Gautier. Saturn Helium Abundance: A Reanalysis of Voyager Measurements. *Icarus*, 144:124–134, March 2000.

B. J. Conrath, P. J. Gierasch, and S. S. Leroy. Temperature and circulation in the stratosphere of the outer planets. *Icarus*, 83:255–281, February 1990.

B. J. Conrath, P. J. Gierasch, and E. A. Ustinov. Thermal Structure and Para Hydrogen Fraction on the Outer Planets from Voyager IRIS Measurements. *Icarus*, 135:501–517, October 1998.

B. J. Conrath and J. A. Pirraglia. Thermal structure of Saturn from Voyager infrared measurements - Implications for atmospheric dynamics. *Icarus*, 53: 286–292, February 1983.

R. Courtin, D. Gautier, A. Marten, B. Bézard, and R. Hanel. The composition of Saturn's atmosphere at northern temperate latitudes from Voyager IRIS spectra - NH3, PH3, C2H2, C2H6, CH3D, CH4, and the Saturnian D/H isotopic ratio. *Astrophysical Journal*, 287:899–916, December 1984.

T. de Graauw, H. Feuchtgruber, B. Bezard, P. Drossart, T. Encrenaz, D. A. Beintema, M. Griffin, A. Heras, M. Kessler, K. Leech, E. Lellouch, P. Morris, P. R. Roelfsema, M. Roos-Serote, A. Salama, B. Vandenbussche, E. A. Valentijn, G. R. Davis, and D. A. Naylor. First results of ISO-SWS observations of Saturn: detection of CO2, CH3C2H, C4H2 and tropospheric H2O. *Astronomy & Astrophysics*, 321:L13–L16, May 1997.

I. de Pater and J. J. Lissauer. *Planetary Sciences*. Planetary Sciences, by Imke de Pater and Jack J. Lissauer, pp. 544. ISBN 0521482194. Cambridge, UK: Cambridge University Press, December 2001., December 2001.

A. D. del Genio, J. K. Meccage, R. Suozzo, R. Opstbaum, D. Rind, W. B. Rossow, G. Russell, and L. D. Travis. Variable Rotation Rate Experiments with the GISS General Circulation Model. In *Bulletin of the American Astronomical Society*, volume 15 of *Bulletin of the American Astronomical Society*, pages 821–+, June 1983.

T. E. Dowling. An Explicit Planetary Isentropic-Coordinate Atmospheric Model for Jupiter, Saturn, Uranus, and Neptune. In *Bulletin of the American Astronomical Society*, volume 25 of *Bulletin of the American Astronomical Society*, pages 1031–+, June 1993.

T. E. Dowling, A. S. Fischer, P. J. Gierasch, J. Harrington, R. P. Lebeau, and C. M. Santori. The Explicit Planetary Isentropic-Coordinate (EPIC) Atmospheric Model. *Icarus*, 132:221–238, April 1998.

T. E. Dowling and A. Herrnstein. Venus EPIC Model Spinup Results. In *Bulletin of the American Astronomical Society*, volume 38 of *Bulletin of the American Astronomical Society*, pages 515–+, September 2006.

U. A. Dyudina, A. P. Ingersoll, S. P. Ewald, C. C. Porco, G. Fischer, W. Kurth, M. Desch, A. Del Genio, J. Barbara, and J. Ferrier. Lightning storms on Saturn observed by Cassini ISS and RPWS during 2004 2006. *Icarus*, 190: 545–555, October 2007.

T. Encrenaz. The Giant Planets. In I. P. Williams and N. Thomas, editors, *Solar and extra-solar planetary systems*, volume 577 of *Lecture Notes in Physics, Berlin Springer Verlag*, pages 54–+, 2001.

T. Encrenaz, J.-P. Bibring, and M. Blanc. *The solar system.* The solar system, 3rd ed., by T. Encrenaz, J.-P. Bibring, and M. Blanc. Astronomy and astrophysics library. Translated by S. Dunlop. Berlin: Springer, 2004., 2004.

T. Encrenaz, P. Drossart, H. Feuchtgruber, E. Lellouch, B. Bézard, T. Fouchet, and S. K. Atreya. The atmospheric composition and structure of Jupiter and Saturn from ISO observations: a preliminary review. *Planet. Space Sci.*, 47:1225–1242, October 1999.

L. W. Esposito, M. Ocallaghan, and R. A. West. The structure of Saturn's rings - Implications from the Voyager stellar occultation. *Icarus*, 56:439–452, December 1983.

H. Feuchtgruber and T. Encrenaz. The infrared spectrum of Neptune at 3.5-4.1 microns: Search for H_3^+ and evidence for recent meteorological variations. *A&A*, 403:L7–L10, May 2003.

U. Fink, D. C. Benner, and K. A. Dick. Band model analysis of laboratory methane absorption spectra from 4500 to 10,500 A. *Journal of Quantitative Spectroscopy and Radiative Transfer*, 18:447–457, 1977.

J. Fischer, R. R. Gamache, A. Goldman, L. S. Rothman, and A. Perrin. Total internal partition sums for molecular species in the 2000 edition of the HITRAN database. *JQSRT*, 82:401–412, November 2003.

F. M. Flasar, R. K. Achterberg, B. J. Conrath, J. C. Pearl, G. L. Bjoraker, D. E. Jennings, P. N. Romani, A. A. Simon-Miller, V. G. Kunde, C. A. Nixon, B. Bézard, G. S. Orton, L. J. Spilker, J. R. Spencer, P. G. J. Irwin, N. A. Teanby, T. C. Owen, J. Brasunas, M. E. Segura, R. C. Carlson, A. Mamoutkine, P. J. Gierasch, P. J. Schinder, M. R. Showalter, C. Ferrari, A. Barucci, R. Courtin, A. Coustenis, T. Fouchet, D. Gautier, E. Lellouch, A. Marten, R. Prangé, D. F. Strobel, S. B. Calcutt, P. L. Read, F. W. Taylor, N. Bowles, R. E. Samuelson, M. M. Abbas, F. Raulin, P. Ade, S. Edgington, S. Pilorz, B. Wallis, and E. H. Wishnow. Temperatures, Winds, and Composition in the Saturnian System. *Science*, 307:1247–1251, February 2005.

L. N. Fletcher, P. G. J. Irwin, N. A. Teanby, G. S. Orton, P. D. Parrish, R. de Kok, C. Howett, S. B. Calcutt, N. Bowles, and F. W. Taylor. Characterising

Saturn's vertical temperature structure from Cassini/CIRS. *Icarus*, 189: 457–478, August 2007.

A. J. Friedson, G. Orton, and R. West. Global Climate Models of Titan, Uranus, and Neptune. *AGU Fall Meeting Abstracts*, pages B1362+, December 2007.

J. Friedson and A. P. Ingersoll. Seasonal meridional energy balance and thermal structure of the atmosphere of Uranus - A radiative-convective-dynamical model. *Icarus*, 69:135–156, January 1987.

E. Gaidos, N. Moskovitz, and D. M. Williams. Terrestrial Exoplanet Light Curves. In C. Aime and F. Vakili, editors, *IAU Colloq. 200: Direct Imaging of Exoplanets: Science and Techniques*, pages 153–158, 2006.

F. C. Gillett and G. S. Orton. Center-to-limb observations of Saturn in the thermal infrared. *Astrophysical Journal Letters*, 195:L47–L49, January 1975.

J. D. Giorgini, D. K. Yeomans, A. B. Chamberlin, P. W. Chodas, R. A. Jacobson, M. S. Keesey, J. H. Lieske, S. J. Ostro, E. M. Standish, and R. N. Wimberly. JPL's On-Line Solar System Data Service. In *Bulletin of the American Astronomical Society*, volume 28 of *Bulletin of the American Astronomical Society*, pages 1158–+, September 1996.

L. P. Giver, D. C. Benner, M. G. Tomasko, U. Fink, and D. Kerola. Gaussian quadrature exponential sum modeling of near infrared methane laboratory spectra obtained at temperatures from 106 to 297 K. In K. Fox, J. E. Allen,

Jr., L. J. Stief, and D. T. Quillen, editors, *Laboratory Research for Planetary Atmospheres*, pages 147–156, May 1990.

G. R. Gladstone, M. Allen, and Y. L. Yung. Hydrocarbon Photochemistry in the Upper Atmosphere of Jupiter. *Icarus*, 119:1–52, January 1996.

R. Goody. *Atmospheric Radiation I: Theoretical Basis.* Oxford University Press, Inc., 1964.

R. Goody, R. West, L. Chen, and D. Crisp. The correlated-k method for radiation calculations in nonhomogeneous atmospheres. *Journal of Quantitative Spectroscopy and Radiative Transfer*, 43:191–199, 1989.

R. M. Goody. A statistical model for water-vapour absorption. *Quarterly Journal of the Royal Meteorological Society*, 78:165–169, April 1952.

C. Goukenleuque, B. Bézard, B. Joguet, E. Lellouch, and R. Freedman. A Radiative Equilibrium Model of 51 Peg b. *Icarus*, 143:308–323, February 2000.

T. K. Greathouse, J. H. Lacy, B. Bézard, J. I. Moses, C. A. Griffith, and M. J. Richter. Meridional variations of temperature, C_2H_2 and C_2H_6 abundances in Saturn's stratosphere at southern summer solstice. *Icarus*, 177:18–31, September 2005a.

T. K. Greathouse, H. G. Roe, and M. J. Richter. Changes in the Temperature of Saturn's Stratosphere from 2002 to 2004 and Direct Evidence of

a Mesopause. In S. Mackwell and E. Stansbery, editors, *36th Annual Lunar and Planetary Science Conference*, volume 36 of *Lunar and Planetary Institute Conference Abstracts*, pages 1365–+, March 2005b.

T. K. Greathouse, H. G. Roe, and M. J. Richter. Evidence for a mesosphere on Saturn and the seasonal variation of temperature between 2002 and 2004 in Saturn's southern hemisphere. In *Bulletin of the American Astronomical Society*, volume 37 of *Bulletin of the American Astronomical Society*, pages 657–+, August 2005c.

J. D. Haigh and M. Blackburn. Solar Influences on Dynamical Coupling Between the Stratosphere and Troposphere. *Space Science Reviews*, 125:331–344, August 2006.

H. B. Hammel, K. A. Rages, and A. J. Friedson. Evidence for Seasonal Change at Uranus' South Pole. In *Bulletin of the American Astronomical Society*, volume 35 of *Bulletin of the American Astronomical Society*, pages 1014–+, May 2003.

H. B. Hammel, M. L. Sitko, D. K. Lynch, G. S. Orton, R. W. Russell, T. R. Geballe, and I. de Pater. Distribution of Ethane and Methane Emission on Neptune. *Astrophysical Journal*, 134:637–641, August 2007.

H. B. Hammel, L. A. Young, J. Hackwell, D. K. Lynch, R. Russell, and G. S. Orton. Variability of Neptune's 12.2-micron ethane emission feature. *Icarus*, 99:347–352, October 1992.

J. B. Holberg, W. T. Forrester, and J. J. Lissauer. Identification of resonance features within the rings of Saturn. *Nature*, 297:115–120, May 1982.

C. J. A. Howett, P. G. J. Irwin, N. A. Teanby, A. Simon-Miller, S. B. Calcutt, L. N. Fletcher, and R. de Kok. Meridional variations in stratospheric acetylene and ethane in the southern hemisphere of the saturnian atmosphere as determined from Cassini/CIRS measurements. *Icarus*, 190:556–572, October 2007.

W. M. Irvine and R. F. Knacke. *The chemistry of interstellar gas and grains*, pages 3–34. Origin and Evolution of Planetary and Satellite Atmospheres, 1989.

P. G. J. Irwin, S. B. Calcutt, and F. W. Taylor. Radiative transfer models for Galileo NIMS studies of the atmosphere of Jupiter. *Advances in Space Research*, 19:1149–1158, May 1997.

P. G. J. Irwin, S. B. Calcutt, F. W. Taylor, and A. L. Weir. Calculated k distribution coefficients for hydrogen- and self-broadened methane in the range 2000-9500 cm^{-1} from exponential sum fitting to band-modelled spectra. *Journal of Geophysical Research (Planets)*, 101:26137–26154, 1996.

P. G. J. Irwin, K. Sihra, N. Bowles, F. W. Taylor, and S. B. Calcutt. Methane absorption in the atmosphere of Jupiter from 1800 to 9500 cm^1 and implications for vertical cloud structure. *Icarus*, 176:255–271, August 2005.

141

P. G. J. Irwin, L. A. Sromovsky, E. K. Strong, K. Sihra, N. A. Teanby, N. Bowles, S. B. Calcutt, and J. J. Remedios. Improved near-infrared methane band models and k-distribution parameters from 2000 to 9500 cm^1 and implications for interpretation of outer planet spectra. *Icarus*, 181: 309–319, March 2006.

N. Jacquinet-Husson, E. Arié, J. Ballard, A. Barbe, G. Bjoraker, B. Bonnet, L. R. Brown, C. Camy-Peyret, J. P. Champion, A. Chédin, A. Chursin, Clerbaux. C., G. Duxbury, J. M. Flaud, N. Fourrié, A. Fayt, G. Graner, R. Gamache, A. Goldman, Vl. Golovko, G. Guelachvili, J. M. Hartmann, J. C. Hilico, J. Hillman, G. Lefévre, E. Lellouch, S. N. Mikhaĭlenko, O. V. Naumenko, V. Nemtchinov, D. A. Newnham, A. Nikitin, J. Orphal, A. Perrin, D. C. Reuter, C. P. Rinsland, L. Rosenmann, L. S. Rothman, N. A. Scott, J. Selby, L. N. Sinitsa, J. M. Sirota, A. M. Smith, K. M. Smith, V. G. Tyuterev, R. H. Tipping, S. Urban, P. Varanasi, and M. Weber. The 1997 spectroscopic GEISA databank. *J. Quant. Spectrosc. Rad. Transfer*, 62:205–254, 1999.

E. Karkoschka. Spectrophotometry of the jovian planets and Titan at 300- to 1000-nm wavelength: The methane spectrum. *Icarus*, 111:174–192, September 1994.

E. Karkoschka. Methane, Ammonia, and Temperature Measurements of the Jovian Planets and Titan from CCD Spectrophotometry. *Icarus*, 133:134–146, May 1998.

E. Karkoschka and M. Tomasko. Saturn's vertical and latitudinal cloud structure 1991 2004 from HST imaging in 30 filters. *Icarus*, 179:195–221, December 2005.

E. Karkoschka and M. G. Tomasko. Saturn's upper troposphere 1986-1989. *Icarus*, 97:161–181, June 1992.

E. Karkoschka and M. G. Tomasko. Saturn's upper atmospheric hazes observed by the Hubble Space Telescope. *Icarus*, 106:428–+, December 1993.

Y. Kaspi and G. Flierl. A General Circulation Model for Deep Circulation on Gas Giants: Internal Convection, Solar Heating and Zonal Flows. *AGU Fall Meeting Abstracts*, pages C1290+, December 2006.

A. A. Lacis and V. Oinas. A description of the correlated-k distribution method for modelling nongray gaseous absorption, thermal emission, and multiple scattering in vertically inhomogeneous atmospheres. *Journal of Geophysical Research (Planets)*, 96:9027–9064, May 1991.

J. H. Lacy, M. J. Richter, T. K. Greathouse, D. T. Jaffe, and Q. Zhu. TEXES: A Sensitive High-Resolution Grating Spectrograph for the Mid-Infrared. *PASP*, 114:153–168, February 2002.

R. P. Lebeau and T. E. Dowling. EPIC Simulations of Time-Dependent, Three-Dimensional Vortices with Application to Neptune's Great Dark SPOT. *Icarus*, 132:239–265, April 1998.

E. Lellouch, R. Moreno, and G. Paubert. A dual origin for Neptune's carbon monoxide? *A&A*, 430:L37–L40, January 2005.

G. F. Lindal, D. N. Sweetnam, and V. R. Eshleman. The atmosphere of Saturn - an analysis of the Voyager radio occultation measurements. *Astrophysical Journal*, 90:1136–1146, June 1985.

K. Liou. *Radiation and Cloud Processes in the Atmosphere*. Oxford University Press, Inc., 1992.

S. Manabe and K. Bryan. Climate Calculations with a Combined Ocean-Atmosphere Model. *Journal of Atmospheric Sciences*, 26:786–789, July 1969.

S. Manabe and R. F. Strickler. Thermal Equilibrium of the Atmosphere with a Convective Adjustment. *Journal of Atmospheric Sciences*, 21:361–385, July 1964.

M. S. Marley and C. P. McKay. Thermal Structure of Uranus' Atmosphere. *Icarus*, 138:268–286, April 1999.

C. E. Max, B. A. Macintosh, S. G. Gibbard, D. T. Gavel, H. G. Roe, I. de Pater, A. M. Ghez, D. S. Acton, O. Lai, P. Stomski, and P. L. Wizinowich. Cloud Structures on Neptune Observed with Keck Telescope Adaptive Optics. *AJ*, 125:364–375, January 2003.

R. Morales-Juberías, A. Sánchez-Lavega, and T. E. Dowling. EPIC simulations of the merger of Jupiter's White Ovals BE and FA: altitude-dependent behavior. *Icarus*, 166:63–74, November 2003.

J. I. Moses, B. Bézard, E. Lellouch, G. R. Gladstone, H. Feuchtgruber, and M. Allen. Photochemistry of Saturn's Atmosphere. I. Hydrocarbon Chemistry and Comparisons with ISO Observations. *Icarus*, 143:244–298, February 2000.

J. I. Moses, T. Fouchet, B. Bézard, G. R. Gladstone, E. Lellouch, and H. Feuchtgruber. Photochemistry and diffusion in Jupiter's stratosphere: Constraints from ISO observations and comparisons with other giant planets. *Journal of Geophysical Research (Planets)*, 110:8001–+, August 2005.

J. I. Moses and T. K. Greathouse. Latitudinal and seasonal models of stratospheric photochemistry on Saturn: Comparison with infrared data from IRTF/TEXES. *Journal of Geophysical Research (Planets)*, 110(E9):9007–+, September 2005.

J. I. Moses, M.-C. Liang, Y. L. Yung, and R.-L. Shia. Two-Dimensional Photochemical Modeling of Hydrocarbon Abundances on Saturn. In *Lunar and Planetary Institute Conference Abstracts*, volume 38 of *Lunar and Planetary Institute Conference Abstracts*, pages 2196–+, March 2007.

O. Muñoz, F. Moreno, A. Molina, D. Grodent, J. C. Gérard, and V. Dols. Study of the vertical structure of Saturn's atmosphere using HST/WFPC2 images. *Icarus*, 169:413–428, June 2004.

P. D. Nicholson, R. G. French, E. Tollestrup, J. N. Cuzzi, J. Harrington, K. Matthews, O. Perkovic, and R. J. Stover. Saturn's rings I. Optical depth profiles from the 28 Sgr occultation. *Icarus*, 145:474–501, June 2000.

J. L. Ortiz, F. Moreno, and A. Molina. Saturn 1991-1993: Clouds and Hazes. *Icarus*, 119:53–66, January 1996.

G. S. Orton, T. Encrenaz, C. Leyrat, R. Puetter, and A. J. Friedson. Evidence for methane escape and strong seasonal and dynamical perturbations of Neptune's atmospheric temperatures. *A&A*, 473:L5–L8, October 2007.

G. S. Orton and P. A. Yanamandra-Fisher. Saturn's Temperature Field from High-Resolution Middle-Infrared Imaging. *Science*, 307:696–698, February 2005.

M. Palmer, L. Gray, and M. Allen. Solar Forcing of Climate: the Importance of Stratospheric Dynamics. In *34th COSPAR Scientific Assembly*, volume 34 of *COSPAR, Plenary Meeting*, 2002.

R. Prangé, T. Fouchet, R. Courtin, J. E. P. Connerney, and J. C. McConnell. Latitudinal variation of Saturn photochemistry deduced from spatially-resolved ultraviolet spectra. *Icarus*, 180:379–392, February 2006.

G. H. Rieke. The thermal radiation of Saturn and its rings. *Icarus*, 26:37–44, September 1975.

L. S. Rothman, D. Jacquemart, A. Barbe, D. C. Benner, M. Birk, L. R. Brown, M. R. Carleer, C. Chackerian, K. Chance, L. H. Coudert, V. Dana,

V. M. Devi, J. M. Flaud, R. R. Gamache, A. Goldman, J. M. Hartmann, K. W. Jucks, A. G. Maki, J. Y. Mandin, S. T. Massie, J. Orphal, A. Perrin, C. P. Rinsland, M. A. H. Smith, J. Tennyson, R. N. Tolchenov, R. A. Toth, J. Vander Auwera, P. Varanasi, and G. Wagner. The HITRAN 2004 molecular spectroscopic database. *Journal of Quantitative Spectroscopy and Radiative Transfer*, 96:139–204, December 2005.

A. Sánchez-Lavega, R. Hueso, S. Pérez-Hoyos, J. F. Rojas, and R. G. French. Saturn's cloud morphology and zonal winds before the Cassini encounter. *Icarus*, 170:519–523, August 2004.

A. Sanchez-Lavega, J. F. Rojas, and P. V. Sada. Saturn's Zonal Winds at Cloud Level. *Icarus*, 147:405–420, October 2000.

B. R. Sandel, D. E. Shemansky, A. L. Broadfoot, J. B. Holberg, G. R. Smith, J. C. McConnell, D. F. Strobel, S. K. Atreya, T. M. Donahue, H. W. Moos, D. M. Hunten, R. B. Pomphrey, and S. Linick. Extreme ultraviolet observations from the Voyager 2 encounter with Saturn. *Science*, 215:548–553, January 1982.

A. P. Showman, C. S. Cooper, J. J. Fortney, and M. S. Marley. Atmospheric Circulation of Hot Jupiters: Three-dimensional circulation models of HD 209458b and HD 189733b with Simplified Forcing. *ArXiv e-prints*, 802, February 2008.

A. P. Showman and I. de Pater. Dynamical implications of Jupiter's tropospheric ammonia abundance. *Icarus*, 174:192–204, March 2005.

147

A. P. Showman, J. J. Fortney, Y. Lian, and M. S. Marley. Coupled Radiative-Dynamical GCM Simulations of Hot Jupiters. In *AAS/Division for Planetary Sciences Meeting Abstracts*, volume 39 of *AAS/Division for Planetary Sciences Meeting Abstracts*, pages 29.06–+, October 2007.

K. Sihra. *Laboratory measurements of near-infrared methane bands for remote sesing of the jovian atmosphere*. University of Oxford, 1998.

B. A. Smith, L. A. Soderblom, D. Banfield, C. Barnet, R. F. Beebe, A. T. Bazilevskii, K. Bollinger, J. M. Boyce, G. A. Briggs, and A. Brahic. Voyager 2 at Neptune - Imaging science results. *Science*, 246:1422–1449, December 1989.

L. A. Sromovsky and P. M. Fry. Modeling Neptune's Seasonal Variation in Cloud Structure. In *Bulletin of the American Astronomical Society*, volume 35 of *Bulletin of the American Astronomical Society*, pages 1013–+, May 2003.

L. A. Sromovsky, P. M. Fry, and K. H. Baines. The Unusual Dynamics of Northern Dark Spots on Neptune. *Icarus*, 156:16–36, March 2002.

L. A. Sromovsky, P. G. J. Irwin, and P. M. Fry. Near-IR methane absorption in outer planet atmospheres: Improved models of temperature dependence and implications for Uranus cloud structure. *Icarus*, 182:577–593, June 2006.

K. Stamnes, S.-C. Tsay, K. Jayaweera, and W. Wiscombe. Numerically stable

algorithm for discrete-ordinate-method radiative transfer in multiple scattering and emitting layered media. *Applied Optics*, 27:2502–2509, 1988.

P. W. Stratman, A. P. Showman, T. E. Dowling, and L. A. Sromovsky. EPIC Simulations of Bright Companions to Neptune's Great Dark Spots. *Icarus*, 151:275–285, June 2001.

K. Strong, F. W. Taylor, S. B. Calcutt, J. J. Remedios, and J. Ballard. Spectral parameters of self- and hydrogen-broadened methane from 2000 to 9500 cmˆ-1 for remote sounding of the atmosphere of Jupiter. *Journal of Quantitative Spectroscopy and Radiative Transfer*, 50:363–429, October 1993.

S. B. Strong. Seasonal Model Temperatures of Saturn's Stratosphere: The Effects of Meridional, Vertical, and Temporal Hydrocarbon Abundance Variations. Submitted to Icarus, 2008.

S. B. Strong, T. Greathouse, and J. Moses. Seasonal Model Temperatures of Saturn's Stratosphere: The Effects of Meridional, Vertical, and Temporal Hydrocarbon Abundance Variations. In *AAS/Division for Planetary Sciences Meeting Abstracts*, volume 39 of *AAS/Division for Planetary Sciences Meeting Abstracts*, pages 37.07–+, October 2007.

K. Sugiyama, M. Odaka, K. Nakajima, and Y.-Y. Hayashi. Numerical Modeling of Moist Convection in Jupiter's Atmosphere. In *Planetary Atmospheres*, pages 122–123, 2007.

M. Sussman, T. E. Dowling, and N. J. Chanover. EPIC Modeling of Seasonal Thermal Forcing on Uranus. In *AAS/Division for Planetary Sciences Meeting Abstracts*, volume 39 of *AAS/Division for Planetary Sciences Meeting Abstracts*, pages 55.05–+, October 2007.

F. W. Taylor and S. B. Calcutt. Near-infrared spectroscopy of the atmosphere of Jupiter. *Journal of Quantitative Spectroscopy and Radiative Transfer*, 32: 463–477, December 1984.

T. Temma, K. H. Baines, R. A. H. Butler, L. R. Brown, L. Sagui, and I. Kleiner. Exponential sum absorption coefficients of phosphine from 2750 to 3550 cm^{-1} for application to radiative transfer analyses on Jupiter and Saturn. *Journal of Geophysical Research (Planets)*, 111:12003–+, December 2006.

G. E. Thomas and K. Stamnes. *Radiative Transfer in the Atmosphere and Ocean.* Radiative Transfer in the Atmosphere and Ocean, by Gary E. Thomas and Knut Stamnes. Cambridge Atmospheric and Space Science Series, Cambridge University Press, 2002, 546 pp., 2002.

W. K. Tobiska,, T. Woods, F. Eparvier, R. Viereck, L. Floyd, D. Bouwer, G. Rottman, and O. R. White. The SOLAR2000 empirical solar irradiance model and forecast tool. *J. Atmos. Solar Terr. Phys.*, 62:1233–1250, 2000.

A. T. Tokunaga, J. Caldwell, F. C. Gillett, and I. G. Nolt. Spatially resolved infrared observations of Saturn. II - The temperature enhancement at the South Pole of Saturn. *Icarus*, 36:216–222, November 1978.

M. G. Tomasko, B. Bezard, L. R. Doose, S. Engel, and E. Karkoschka. Measurements of Methane Absorption by the Descent Imager/Spectral Radiometer (DISR) During its Descent through Titan's Atmosphere. *Icarus*, 2007. Submitted.

M. G. Tomasko and L. R. Doose. Polarimetry and photometry of Saturn from Pioneer 11 Observations and constraints on the distribution and properties of cloud and aerosol particles. *Icarus*, 58:1–34, April 1984.

U. S. Government Printing Office (Usgpo). *The Astronomical Almanac for the year 2005.* The Astronomical Almanac for the year 2005, Washington: U.S. Government Printing Office (USGPO), 2005, U.S. Naval Observatory (USNO), Royal Greenwich Observatory (RGO)., 2005.

U. S. Government Printing Office (Usgpo). *The Astronomical Almanac for the year 2007.* The Astronomical Almanac for the year 2007, Washington: U.S. Government Printing Office (USGPO), 2007, U.S. Naval Observatory (USNO), Royal Greenwich Observatory (RGO)., 2007.

L. Wallace. The structure of the Uranus atmosphere. *Icarus*, 43:231–259, September 1980.

R. V. Yelle, C. A. Griffith, and L. A. Young. Structure of the Jovian Stratosphere at the Galileo Probe Entry Site. *Icarus*, 152:331–346, August 2001.

Y. L. Yung and W. B. Demore. *Photochemistry of planetary atmospheres.* Oxford University Press, 1999.

Index

Vita

Shadrian B. Strong was born in Tucson, Arizona on 29 February 1980, the daughter of Mrs. Janette Holmes and Mr. Stanley Holmes. She graduated cum laude with a Bachelor of Science degree in Physics from the College of Charleston, SC in 2001. She interned at Lowell Observatory in Flagstaff, AZ, Maria Mitchell Observatory in Nantucket, MA, and Cerro Tololo Inter-American Observatory in Chile leading up to her attendance of graduate school in the Department of Astronomy at The University of Texas at Austin in 2002. As a graduate student, Shadrian was employed by the Lunar and Planetary Institute in Houston and frequently traveled between Houston and Austin for research purposes. In 2006, she interned at the Jet Propulsion Lab in Pasadena, CA and worked on the development of a proposal for a Saturn-probe New Frontiers mission. In graduate school, she worked on a variety of projects including mid-infrared instrumentation, hydrodynamic simulations of massive stars (resulting in an M.A.), and as an observer on the Texas Echelon Cross Echelle Spectrograph (TEXES) team lead by John Lacy.

Permanent address: 8911 North Plaza Court
                   Austin, Texas 78753

This dissertation was typeset with LaTeX[†] by the author.

[†]LaTeX is a document preparation system developed by Leslie Lamport as a special version of Donald Knuth's TeX Program.